HIGH THROUGHPUT PROFILE MILLLING FOR THE FLEXIBLE AND ACCELERATED PROCESSING OF ELECTRIC STEELS

A Thesis
Presented to
The Academic Faculty

by

Howard J. Liles

In Partial Fulfillment
of the Requirements for the Degree
Masters of Science in the
G. W. Woodruff School of Mechanical Engineering

Georgia Institute of Technology
May 2013

HIGH THROUGHPUT PROFILE MILLLING FOR THE FLEXIBLE AND ACCELERATED PROCESSING OF ELECTRIC STEELS

Approved by:

Dr. J. Rhett Mayor, Advisor
G. W. Woodruff School of Mechanical Engineering
Georgia Institute of Technology

Dr. Shreyes Melkote
G. W. Woodruff School of Mechanical Engineering
Georgia Institute of Technology

Dr. Steven Liang
G. W. Woodruff School of Mechanical Engineering
Georgia Institute of Technology

Date Approved: 4/3/2013

ACKNOWLEDGEMENTS

I would like to thank my committee members, Dr. Steven Liang and Dr. Shreyes Melkote for their time and energy. Their evaluation and recommendation has greatly influenced this work for the better.

I would like to thank my lab mates for their countless hours of advice, encouragement, and support in my research endeavor. Their help has been invaluable in this effort and has greatly contributed to my development as a researcher and as an engineer.

I would like to also thank my advisor Dr. J. Rhett Mayor. His guidance and mentorship has significantly aided in both my personal and professional development.

I would like to thank the countless family members and friends who have provided encouragement and support during my time in graduate school.

I would like to thank my wife, Iyanna, for her steadfast and loving support. I am truly grateful for her companionship and encouragement during this challenging endeavor.

Finally I would like to thank my *Heavenly Father.* It has been his counsel, love, support, and wisdom that have even made this accomplishment possible.

TABLE OF CONTENTS

ACKNOWLEDGEMENTS iii

LIST OF TABLES viii

LIST OF FIGURES ix

SUMMARY xvi

CHAPTER 1 INTRODUCTION 1

1.1 Introduction 1

1.2 Review of Required Properties of Electrical Steels 7

1.2.1 Electrical Steel Mechanical Properties 7

1.2.2 Electrical Steel Magnetic Properties 8

1.3 Research Objectives 9

1.4 Summary and Outline of Thesis 9

CHAPTER 2 REVIEW OF RELEVANT LITERATURE 11

2.1 Introduction 11

2.2 Traditional Laminate Processing Techniques for Electric Machines 11

2.2.1 Electric Discharge Machining 11

2.2.2 Laser Beam Machining 14

2.2.3 Abrasive Waterjet Machining 17

2.2.4 Mechanical Stamping 19

2.2.5 Comparison Studies of Traditional Processing Techniques.....20

2.3 HTPM.....22

2.4 Summary and Identification of Research Gaps.....24

CHAPTER 3 DEVELOPMENT OF A MECHANISTIC MODEL FOR THE CUTTING RESPONSE OF M-19 ELECTRICAL STEEL.....28

3.1 Introduction.....28

3.2 Analytical Model.....29

3.3 Apparatus and Experimental Setup.....34

3.3.1 Laminate Stack Preparation Methodology.....37

3.4 Experimental Approach and Methodology.....38

3.5 Preliminary Empirical Investigation of Material Properties.....48

3.5.1 Results and Analysis (Coarse Study).....50

3.6 Detailed Empirical Investigation of Material Properties.....53

3.7 Results.....55

3.8 Analysis.....57

3.9 Discussion.....63

3.10 Summary.....67

CHAPTER 4 OPTIMIZATION OF CUTTING PARAMETERS FOR MAXIMUM PRODUCTIVITY AND MINIMUM BURR FORMATION.....69

4.1 Introduction.....69

4.1.1 Material Properties of M-19 Electrical Steel....69
4.1.2 Burr formation metric....73
4.1.3 Delamination metric....74
4.2 Approach....74
4.3 Apparatus and Experimental Setup....75
4.4 Results....78
4.4.1 Coarse study (Initial Investigation)....78
4.4.2 Analysis (Coarse Study)....81
4.4.3 Results (Fine Study)....82
4.5 Analysis....83
4.6 Discussion....85
4.6.1 Burr Formation....85
4.6.2 Delamination....87
4.7 Supplementary Study on Tool Wear....89
4.8 Summary....91
CHAPTER 5 CONSIDERING THE IMPACT OF PROCESS HISTORY ON MAGNETIC PROPERTIES OF M-19 ELECTRIC STEEL....93
5.1 Introduction....93
5.1.1 Magnetic Properties of M-19 Electrical Steel....94
5.2 Experimental Approach....94

5.3 Apparatus and Experimental Setup 96
5.3.1 Specimen Preparation 99
5.3.2 Metrology 101
5.4 Analysis 102
5.4.1 Specific Core Loss 103
5.4.2 Permeability 104
5.5 Results 104
5.5.1 Experimental Uncertainty 108
5.6 Discussion 112
5.6.1 Burr Formation and Oxidation 112
5.6.2 Magnetic Properties 115
5.6.3 Productivity 115
5.7 Summary 116
CHAPTER 6 SUMMARY AND CONCLUSIONS 118
6.1 Summary 118
6.2 Conclusions 120
6.3 Publications 121
6.4 Recommendations for Future Work 121
REFERENCES 124

LIST OF TABLES

Table 3.1: Particle Swarm optimization parameters 45

Table 3.2: Experimental Testing Matrix (Coarse Study) 49

Table 3.3 Cutting Characteristics Table 53

Table 3.4 Experimental Test Matrix (Fine Study) 54

Table 3.5 Comparison of force averaged and empirically tuned specific cutting energy and force ratio 64

Table 3.6 Resultant force ratio for single layer stack vs. double layered stacks 66

Table 4.1 Chemical composition of M-19 electrical steel used in this study[72] 69

Table 4.2: M-19 Material Properties. 71

Table 5.1: M-19 Material Properties. 94

Table 5.2 Experimental Test Matrix 95

Table 5.3 Measured data from magnetic testing 105

Table 5.4 Measurement Equipment and Reported Accuracy 108

Table 5.5: Decision Table for Hypothesis Test 110

Table 5.6: Specific Core Loss Comparison Results of Hypothesis Test. 111

Table 5.7: Permeability Comparsion Results of Hypothesis Test 111

Table 5.8 Comparison Metric for Abrasive Waterjet Machining and HTPM 116

LIST OF FIGURES

Figure 1.1 Electrical vehicles currently in production by various manufacturers. (A) Plug-in hybrid electric vehicle produced by GM[1]. (B) All electric vehicle produced by Nissan[2]. 2

Figure 1.2 Prototype of ultra-high speed electric machine. 3

Figure 1.3 Finite element model of ultra high speed spindle developed by Kunz et. al[7]. Warmer colored regions indicate increased magnetic flux density. Red regions indicate magnetic saturation. The solid blue regions between the stator teeth indicate no magnetic flux and represents air as opposed to electrical steel..... 5

Figure 1.4 Single laminate of a stator and laminated stack of a rotor. Characteristic dimensions: Rotor tooth width: 1.1mm; Stator tooth width: 1.8mm; Air gap between stator and rotor: 350microns 6

Figure 2.1 (A) Laminated stack of electrical steel cut via wire EDM. (B) Top view of Image A. Significant rusting is visible along the edges and surface of the stack. (C) Microscope image of wire EDM cut of a single laminate. Oxidations and corrosion is clearly visible along the edge of the cut 14

Figure 2.2 (Left) Heat affected zone of electrical steel after being laser beam machined. The sample has been polished and etched. The top portion of the image shows a clear difference in grain structure as compared to the bottom portion [23]. 16

Figure 2.3 Laser machined laminated stack of an aluminum composite. Damage to the interlaminar layer is clearly visible [25]. 17

Figure 2.4 Diagram illustrating embedment of abrasive particles as into a laminated workpiece. This embedment results in stresses that act separate the layers leading to delamination of the composite [29]. 18

Figure 2.5 (A) Delaminate of a graphite/epoxy composite that was processed via abrasive waterjet machining (B) A magnified view depicting an actual abrasive particle embedded in the composite[29]. 19

Figure 3.1 Orthogonal cutting model. Top figure illustrates slot milling process. Bottom figure depicts cutting forces of a tooth cutting through a laminated stack. 30

Figure 3.2 Tlusty and McNeil's cutting force model. The top plot shows the planar cutting force components as a function of cutter rotation angle. The bottom figure shows the resultant cutting force as a function of cutter rotation angle.... 33

Figure 3.3 Bao and Tansel's cutting force model. The top plot shows the planar cutting force components as a function of cutter rotation angle. The bottom figure shows the net cutting force as a function of cutter rotation angle. 33

Figure 3.4 (A) View of endmill tip and cutting diameter (B) Microscope image of endmill tip to approximate cutting edge radius..... 35

Figure 3.5 Machining set-up used during this study..... 35

Figure 3.6 Velocity profile of machine tool motion during a cutting trial. 37

Figure 3.7 Fast Fourier Transform of the force data obtained during a cutting trial. 40

Figure 3.8 Characteristic force data obtained from a cut. 40

Figure 3.9 Averaged single point estimate of cutting forces in the crossfeed direction compared to the measured data for the corresponding direction. 42

Figure 3.10 Averaged single point estimate of cutting forces in the crossfeed direction compared to the measured data for the corresponding direction. 42

Figure 3.11: Flow chart depicting optimization algorithm utilized to determine specific cutting energy and force ratio. 44

Figure 3.12 Characteristic plot of analytical model of cutting forces in the feed direction compared to the measured data for the corresponding direction. 46

Figure 3.13 Analytical model of cutting forces in the crossfeed direction compared to the measured data for the corresponding direction. 47

Figure 3.14 Analytical model of planar resultant cutting forces compared to the resultant force data obtained during experimental cutting trials. 47

Figure 3.15 (A) Two layer laminated stack after being bonded in the compression jig (before testing). (B) Photograph of sample laminated stack of machining experiments (after testing). The white residue is simply excess epoxy that is still adhered to the stack. 50

Figure 3.16 Microscope photograph of slot machined into a laminated stack of M-19. (A) Slot cut using low feed rate and low spindle speed. (B) Slot cut using higher feed rates and low spindle speeds. 51

Figure 3.17 Resultant forces in the plane of the laminate (excluding axial component).. 52

Figure 3.18 Single laminate average resultant cutting forces as a function of feed per tooth. 56

Figure 3.19 Double laminate average resultant cutting forces as a function of feed per tooth. 56

Figure 3.20 Average force values at varying feeds per tooth for single laminate machining experiments with fitted in a piecewise manner. A 2^{nd} order polynomial fit is applied to the first two data points while the last five are fitted with a linear fit. The dotted line indicates a possible linear trend that may occur as the process transitions from a plowing dominant to a cutting dominant regime. However this region is not well characterized. 58

Figure 3.21 Micro-milling cutting forces vs. tool engagement (analogous to feed per tooth). Plots show the minimum chip thickness effect resulting in a peak in the cutting forces[45]. 58

Figure 3.22 Average specific cutting energy values at varying feeds per tooth for single laminate machining experiments with a power law fitted trend line to illustrate material response. Note that error bars indicate experimental uncertainty..... 60

Figure 3.23 Average force ratio (Kr) values at varying feeds per tooth for single laminate machining experiments. A power fit is applied to the first two data points while the last five are fitted with a separate power fit. The dotted line indicates a possible linear trend that may occur as the process transitions from a plowing dominant to a cutting dominant regime. However, this region is not well characterized. Note that error bars indicate experimental uncertainty..... 62

Figure 3.24 Specific cutting energy vs. feed per tooth at multiple cutting speeds. (Left) single laminate. (Right) Two laminate stack. 65

Figure 4.1 Approximated stress strain curves for various types of steels..... 71

Figure 4.2 Comparison of toughness of various types of steel..... 72

Figure 4.3 Image obtained via digital microscope illustrating a high throughput profile milled machined slot and the surface profile of this slight taken along the red vertical line. 76

Figure 4.4 Peak burr height for the eight conditions under investigation. Displayed values are the average of 3 replicates with the standard deviation above and below these values. 79

Figure 4.5 Burring percentage for the eight conditions under investigation. Displayed values are the average of 3 replicates with a standard deviation above and below these values. 79

Figure 4.6 (LEFT) Comparison of cut quality. (a) Edge of cut made using Case 4 (80,000rpm, 7 micron feed per tooth, two laminate stack) with very little burring. (b) Edge of cut made using Case 5 (20,000rpm, 2 micron feed per tooth, single laminate stack) with significant burring..... 80

Figure 4.7 Sidewalls of cut laminated stack. (a) Slight delamination is observable (cut from Case 1 at 20,000rpm, 2 micron feed per tooth, and two laminate stack). (b) No delamination is observable (cut from Case 3 at 20,000rpm, 7 micron feed per tooth, two laminate stack). Note: black region is surface of microscope table. It has been digitally modified to enable easier viewing of the image..... 81

Figure 4.8 Maximum peak burr height as a function of feed per tooth. Error bars indicate standard deviation. 82

Figure 4.9 Mean burr height as a function of feed per tooth. Error bars indicate standard deviation. 83

Figure 4.10 Characteristic Surface roughness profile taken from a trace along the edge of a machined slot. 85

Figure 4.11 Illustrations of modes of delamination in a laminated stack 87

Figure 4.12 Machined slot within a laminated stacks exhibiting no delamination. (A) Left side of slot. (B) Right side of slot 88

Figure 4.13 Machined slot within a laminated stack exhibiting slight delamination near the outer edge (A) but not delamination near the base of the same slot(B). 88

Figure 4.14: Mean burr height as a function of cutting length. Cutting condition: feed per tooth 32 microns per tooth; spindle speed 80,000rpm. The fitted line is a fourth order polynomial fit. The dotted line demarcates a cutting length of 360mm which is equivalent to the maximum cutting length of a given study. 90

Figure 4.15: Mean burr height as a function of cutting length. Cutting condition: feed per tooth 7 microns per tooth; spindle speed 80,000rpm. The fitted line is a fourth order polynomial fit. The dotted line demarcates a cutting length of 360mm which is equivalent to the maximum cutting length of a given study.. 91

Figure 5.1 Magnetic testing fixture and schematic of fixture design 97

Figure 5.2 Circuit diagram of magnetic testing fixture..... 99

Figure 5.3 Machining fixture for producing HTPM laminate test samples. 101

Figure 5.4 Average permeability for different processing methods. Permeability was measured at 60Hz and 1.5T. The dotted line indicates the typical minimum permeability for this material. 107

Figure 5.5 Average specific core loss for different processing methods. Specific core loss was measured at 60Hz and 1.5T. The dotted line indicates the required maximum allowable core loss by the ASTM standard. 107

Figure 5.6 Oxidation occurring on electric steel after abrasive waterjetting, despite prompt removal of water via compressed air. 112

Figure 5.7 Peak burr height and average burr height for abrasive waterjet samples at two conditions compared to HTPM. The error bars indicate the standard deviation amongst the measured samples. 113

Figure 5.8 Rusting and burr formation at different locations along the edge of abrasive waterjet machined pieces of M-19 electrical steel illustrating consistent burring along the edge. The far right image is a magnification of the far left image revealing the burred edge. 114

Figure 6.1: (A) Specimen used for this study. (B) Future specimen design with increased process affected area. Note that the dark border around the edge of image A and around the internal cuts of image B indicates process affected area. 123

SUMMARY

The proliferation of electric machines has drastically increased in recent years and is likely to increase into the future. This interest in the production of advanced, high power density electrical machines that are small in size has heightened the need for flexible manufacturing processes to produce their laminated components during short batch and prototyping production runs. A means of cost effective, accelerated prototyping of these machines will have a substantial impact on their design and optimization, reducing time requirements to produce and test a given design. A review of the current manufacturing methods for prototyping electric machines was conducted. In particular, laser cutting, electric discharge machining, and abrasive waterjet (AWJ) machining were researched as competitive processes. Each of these methods exhibits marked advantages and disadvantages that present the opportunity for a new process to compete. This work investigates the applicability of high throughput profile milling (HTPM) for the prototyping of advanced electric machines, specifically, the process parameter space for milling of electrical steels. The material response will be determined by characterizing its specific cutting energy and utilizing this to develop a model to predict cutting forces during the milling process. Optimal process parameters will be investigated to obtain maximum productivity and minimal burr formation. Finally, the impact of HTPM processing on the magnetic properties of electrical steels will be compared to that of a leading prototyping technology, AWJ machining.

CHAPTER 1

1.1 Introduction

Electric machines serve as the primary means of converting electrical energy into mechanical work; thus, their development and optimization can potentially have far reaching impacts on areas such as the automotive, aeronautical, and mobile power industries. Consequently the widespread proliferation and utilization of these machines has drastically increased in recent years and is likely to increase even more into the future. Recent developments in major manufacturing industries such as the automotive industry's increased interest in electrical and hybrid electric vehicles are clear indicators of this trend. The electrification of the automotive industry is accelerating. All of the primary automotive manufacturers already have hybrid electric vehicles in production and some of the OEM's have recently launched all-electric vehicles. GM has launched the Chevy Volt, shown in Figure 1.1(A), as a serial hybrid vehicle with a range extending engine and Nissan has released the Leaf, shown in Figure 1.1(B) as an all-electric vehicle. These vehicles both employ primary traction motors, electrical machines that are providing the tractive torque to the power train. As the automotive industry moves towards increased product offerings with electrical traction power trains the demands on the electrical machine research and development timeframes will be significantly increased.

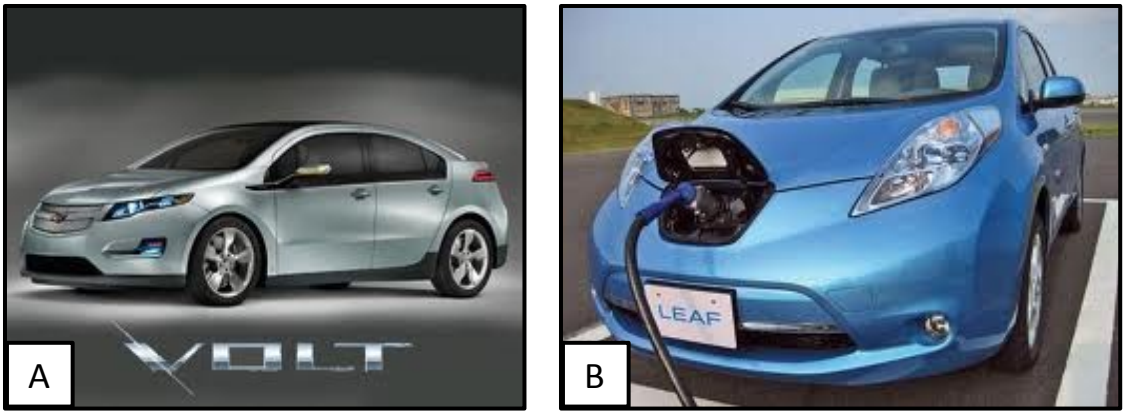

Figure 1.1 Electrical vehicles currently in production by various manufacturers. (A) Plug-in hybrid electric vehicle produced by GM[1]. (B) All electric vehicle produced by Nissan[2].

The demands for advanced, highly optimized electric machines are increasing in multiple industries, not only in the automotive sector. The machine tool industry is increasingly moving towards high-speed machining centers that require optimized spindle motors that have high speeds and torque density requirements. OKUMA, Nakanishi, and HAAS are a few leading machine tool manufacturers that are continuing to develop machine tool with high torque capabilities and high spindle speeds to meet the demand for increased productivity[3-5].

More recently, the emerging micro-machining industry has created the demand for ultra-high-speed spindles with rotational speeds approaching 500,000rpm. Multiple research groups are actively engaged in meeting this challenge. Kolar et. al has developed a permanent magnetic electric drive capable of exceeding these rotational speeds[6]. Furthermore, research conducted out of this group has performed design and analysis to develop an ultra high speed spindle capable of rotating at 750,000 revolutions per minute[7] . Figure 1.2 illustrates an initial stator-housing prototype based on the ultra high speed spindle design and is indicative of the small size of some of these machines.

Figure 1.2 Prototype of ultra-high speed electric machine.

Furthermore, the electrification of the aircraft industry is adding to the demand for advance electric machines. Boeing's 787 has been developed such that virtually everything that has traditionally been powered by bleed-air from the engines has been transitioned to an electric architecture[8]. This industry is particularly demanding in that aircraft have specific weight and size requirements for the electric machines.

Finally the increasing demand for advanced electric machines has become an area of national significance. The U.S. Department of Energy's Advanced Research Projects Agency-Energy (ARPA-E) has recently awarded $9.6 million from the American Recovery and Reinvestment Act for transformational energy research projects including projects aimed at improving the energy efficiency and power density of electric machines[9]. Furthermore, the Obama administration has released several statements motivating the development of these machines[10, 11]. This is strategically directed at stimulating economic growth in addition to continuing the technological advancement of the country.

The increased interest in the production of advanced, high power density electrical machines that are small in size have heightened the need for flexible manufacturing

processes to produce their laminated components during short batch and prototyping production runs. Producing prototypes is a critical step in the design and development of new technologies as it enables testing and analysis that cannot be accomplished via any other means. Thus a means of cost effective, accelerated prototyping of these machines will have a substantial impact on the design and optimization efforts as it will reduce time requirements to produce and test a given machine design. This allows developers to spend their times and efforts more efficiently by expediting the design cycle.

Furthermore, "specialty" machines that are produced in small numbers with highly specific requirements and high design variability require a production method that is flexible enough to accommodate the changing design constraints while maintaining acceptable production rates. "Specialty" machines refer to devices such as advanced electric machines that may be used aboard aircraft with precise performance constraints which cannot be met with the typical off the shelf approach. These precise constraints also require the materials and components to function at a very high level.

Figure 1.2 presents a finite element model which is used in the electromagnetic design of another specialty machine, the ultra high speed spindle mentioned earlier. This model investigates the magnetic flux lines of the rotor and stator of the machine, revealing that there are regions that are heavily loaded (the warm colored regions) and approaching saturation (the electromagnetic performance limit of the material). If these regions are degraded by the process history of the material, higher core losses, lower machine efficiency and lower saturation limits will be realized. Furthermore, stators and rotors at this small scale may be more susceptible to process related material degradation

since most of the electrical steel, by volume, is being utilized (indicated by the fact that most of the stator surrounding the active tooth is warm colored).

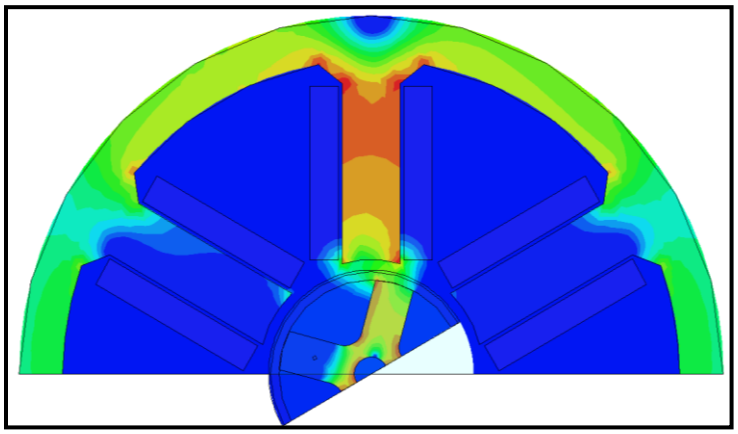

Figure 1.3 Finite element model of ultra high speed spindle developed by Kunz et. al[7]. Warmer colored regions indicate increased magnetic flux density. Red regions indicate magnetic saturation. The solid blue regions between the stator teeth indicate no magnetic flux and represents air as opposed to electrical steel.

As advanced electric machines continue to proliferate, the need for these specialty machines will increase. This presents a challenge to the conventional production process. Electric machines are frequently produced in large production runs via a stamping process. Stamping is a very effective mass production process for fixed designs; however, the high costs associated with the die sets for each individual laminate design limits the flexibility of the process and consequently reduces the suitability of the method to short production runs and prototyping of advanced designs.

Many of these advanced electric machines are also often miniature in size as efforts to increase energy density evolve. Their small geometries (as illustrated in Figure 1.4) introduce an additional challenge to the manufacturing process as shaping and handling numerous small components that comprise these machines can be quite difficult. As the dimensions of these machine components decrease and performance demands rise, the

tolerance for error in the production of these machines reduces and thus the components must be well designed (with good agreement between the design and the actual physical device) and produced with high quality (limited defects or burrs).

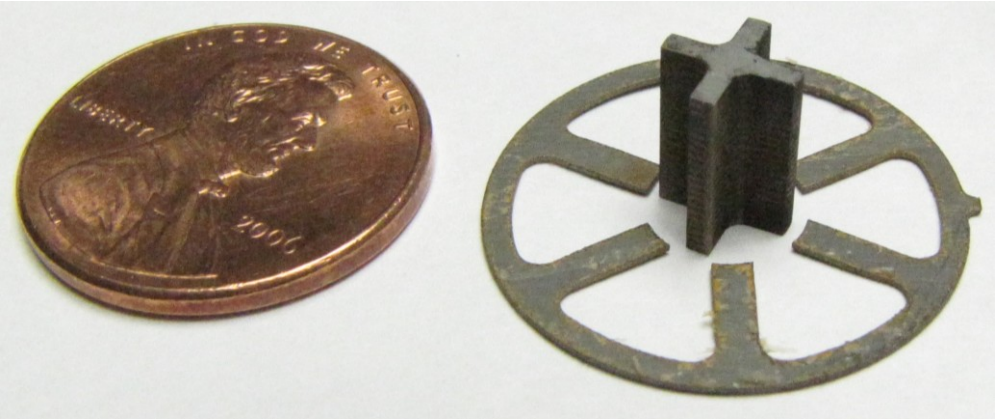

Figure 1.4 Single laminate of a stator and laminated stack of a rotor. Characteristic dimensions: Rotor tooth width: 1.1mm; Stator tooth width: 1.8mm; Air gap between stator and rotor: 350microns

The high degree of specificity required in the design of specialty and highly optimized electric machines in addition to the flexibility required for rapidly changing designs motivates the need for a suitable process of quickly prototyping and producing these machines. In fact, development and manufacturing of the ultra high speed spindle mentioned previously is a direct motivating application for an accelerated prototyping process. An investigation into the performance of other widely utilized manufacturing methods for prototyping electric machines was conducted. Of the possible manufacturing methods, particularly laser cutting, electric discharge machining (EDM), and abrasive waterjet (AWJ) machining were researched as competitive processes. Each of these methods exhibit marked advantages and disadvantages that consequently present the opportunity for a new process to compete.

This research aims to address the agile manufacturing of advanced electric machine prototypes through the development of high-throughput profile milling (HTPM) process technology as an alternative solution to the production of the electrical steel laminates required in the active (magnetically) components of the new generation of high-torque density and high speed electrical machines.

1.2 Review of Required Properties of Electrical Steels

As previously mentioned, electrical machines typically include a stator and rotating rotor used to produce mechanical work. Sarma provides a more detailed description of the operating principles of electric machines[12]. These machine components are composed of electrical steel, low-carbon steel that has been alloyed with up to 3% silicon. This alloying process results in significant changes to both the magnetic and mechanical properties of the material. M-19 electrical steel is the specific alloy of metal that will be investigated in this work. It was selected due to its common use in the electric machines industry as a low core loss material.

1.2.1 Electrical Steel Mechanical Properties

The addition of silicon and other elements (added to enhance the magnetic properties of the metal) significantly changes the machinability of the material. Smith discusses how other than improving magnetic properties, the alloying of steel with silicon is performed to greatly increase strength and toughness in order to produce ultra high strength steel used in components such as aircraft landing gear[13]. This increase in strength and toughness results in a corresponding decrease in machinability.

1.2.2 Electrical Steel Magnetic Properties

The magnetic properties of M-19 steel, however, are quite favorable for constructing electric machines. The silicon increases the electrical resistivity, enables desirable grain growth, and also enables the development of preferred orientation grain structure[14]. Its saturation induction of just over two tesla is approaching the limit of the induction capability of existing materials. Furthermore, the low core loss allows the material to be very efficient with minimal eddy current formation.

Conversely, the manufacturing processes that shape the electrical steels into the geometries necessary to form a machine introduce challenges stemming from the sensitivity of the magnetic performance of these materials to the changes in the microstructure. Thermal or mechanical deformation of the grains of electrical steels affects the performance of the material, particularly the core loss and the permeability. Furthermore, this phenomenon is further complicated by the fact that there exists and optimum grain size for minimum core loss. Thus increasing above or below this value can result in degraded magnetic properties. Consequently, the performance of the final electric machine is sensitive to the processing history of the electrical steel. Deformations of the grains as small as tens of microns can result in decreased permeability and increased core loss. Thus care must be taken to shape the electrical steel laminates into the desired shapes while simultaneously minimizing the total mechanical and thermal stresses left in the finished components.

1.3 Research Objectives

This work aims to investigate the applicability of HTPM as a manufacturing process for the prototyping of advanced electric machine. Specifically, this work will investigate the process parameter space for milling of electrical steels. The material response will be determined by characterizing its specific cutting energy at multiple feed rates and utilizing these to develop a cutting force model to predict cutting forces during the milling process. Optimal process parameters will be investigated to obtain maximum productivity (maximum linear feed rate) and minimal burr formation. Furthermore, the relative impact of high through-put profile milling processing on the magnetic properties of electrical steels will be compared to that of current leading electrical steel prototyping technologies (specifically abrasive waterjet machining). The core loss and magnetic permeability of the two processes will be compared and analyzed statistically. Furthermore, additional performance comparisons such as relative productivity, burr formation, etc. will be investigated.

1.4 Summary and Outline of Thesis

Overall, there exists sufficient motivation to justify further study of an accelerated process for producing advanced electric machine prototypes. Electrical steel presents a significant challenge as the material from which the unique geometries of these machines must be produced. The performance of the machine is directly dependent on the processing technique due to the sensitivity of the material to mechanically and thermally induced deformations. Furthermore, this material exhibits significant toughness and processing laminated stacks of thin materials has challenges of its own. Results from preliminary work and these other observations serve to indicate that this particular

problem is challenging, interesting and worthy of additional research. Thus an investigation into HTPM of electrical steels for the accelerated prototyping of electrical machines is conducted. The subsequent chapters will discuss in detail this effort. First, Chapter 2 presents a review of the literature concerning current manufacturing techniques for processing electrical steel in addition to literature relevant to processing this material via HTPM. Chapter 3 presents the development of a mechanistic model for the cutting response of M-19 electrical steel. Chapter 4 continues to discuss optimization of cutting parameters for maximum productivity and minimum burr formation. The experimental studies performed in Chapter 3 and Chapter 4 were conducted concurrently using the same experimental plan; however, for clarity of presenting and discussing the results and analysis developed, the work is divided categorically into mechanistic modeling and process optimization respectively. Chapter 5 presents a comparison of the effects of process history on magnetic performance between abrasive waterjet machining and HTPM. Finally, Chapter 6 summarizes the conclusion of this investigation and discusses future work that still remains to be conducted.

CHAPTER 2

REVIEW OF RELEVANT LITERATURE

2.1 Introduction

The literature is reviewed to investigate the effects of different processing methods on the performance of electrical steels. The current traditional electrical steel processing methods investigated include: abrasive waterjet machining, electric discharge machining, laser beam machining, and stamping. The literature was also reviewed to determine if the proposed HTPM has previously been explored. Specifically application of this process to the production of electric steel laminates and previous attempts to machine laminated stacks of electric steel were investigated. Furthermore, literature regarding the modeling of the milling process mechanics and investigating the material properties particularly relevant to the machining of these steels was also reviewed.

2.2 Traditional Laminate Processing Techniques for Electric Machines

2.2.1 Electric Discharge Machining

The electric discharge machining (EDM) process occurs through a material erosion mechanism primarily making use of electrical energy and turning it into thermal energy through a series of discrete electrical discharges occurring between the electrode and workpiece immersed in a dielectric fluid. Ho et. al describes this process stating that the thermal energy generates a channel of plasma between the cathode and anode at a temperature in the range of 8000 to 12,000 °C or as high as 20,000 °C initializing a substantial amount of heating and melting of material at the surface of each pole[15].

When the pulsating direct current supply occurring at the rate of approximately 20,000–30,000 Hz is turned off, the plasma channel breaks down. This causes a sudden reduction in the temperature allowing the circulating dielectric fluid to implore the plasma channel and flush the molten material from the pole surfaces in the form of microscopic debris. This process of melting and evaporating material from the workpiece surface is in complete contrast to the conventional machining processes, as chips are not mechanically produced. The volume of material removed per discharge is typically in the range of 10^6–10^4 mm^3 and the material removal rate (MRR) is usually between 2 and 400 mm^3/min. Wire EDM is a variation of the typical EDM process utilizing a thin wire as the electrode. This variant enables significant flexibility by combining multiple linear and rotary stages and the wire to cut through metal materials and creating 3D structures. The typical WEDM cutting rates (CRs) are 300 mm2/min for a 50 mm thick D2 tool steel and 750 mm2/min for a 150 mm thick aluminum, and SF quality is as fine as 0.04–0.25 μm Ra.[16]

Kumar et. al discusses the surface and subsurface damage incurred by EDM of different materials[17]. An easily removed spattered EDM surface layer is created when expelled molten metal and small amounts of electrode material form spheres and spatter the surface of the workpiece. The action of EDM has actually altered the metallurgical structure and characteristics in the recast layer. This layer is formed by the un-expelled molten metal solidifying in the crater. The molten metal is rapidly quenched by the dielectric. Micro-cracks can form in this very hard, brittle layer. If this layer is too thick or is not reduced or removed by polishing, the effects of this layer can cause premature failure of the part in some applications. The last layer is the heat-affected zone (HAZ) or

annealed layer, which has only been heated, not melted. The depth of the recast layer and the heat-affected zone is determined by the heat sinking ability of the material and the power used for the cut. This altered metal zone influences the quality of the surface integrity. Furthermore, Ghanem et. al investigates effects that EDM has on the surface integrity of several steels. He discusses how the EDM process induces residual stresses and cracking into the materials [18]

In addition to reviewing the literature, an AgieCharmilles Cut 20 P wire EDM was used to cut single and stacked laminates of electrical steel. This also resulted in significant rusting of the material, as can be seen in Figure 2.1 This rusting inhibits the EDM cutting process leading to increased wire breakage; a non-trivial problem. In addition to this, cutting the laminated stack was quite tedious due to repeated wire breakage. Furthermore, additional corrosion of the surface was visible along the edges of some of the cuts (see Figure 2.1) when machined at higher feed rates. This additional damage is likely due to excessive heating of the material along the edges of the cut and could indicate additional damage to the magnetic properties of the surrounding material. While it is possible to cut via this method, the rapid corrosion and precise demands of the EDM process reduce the productivity and quality of the final part.

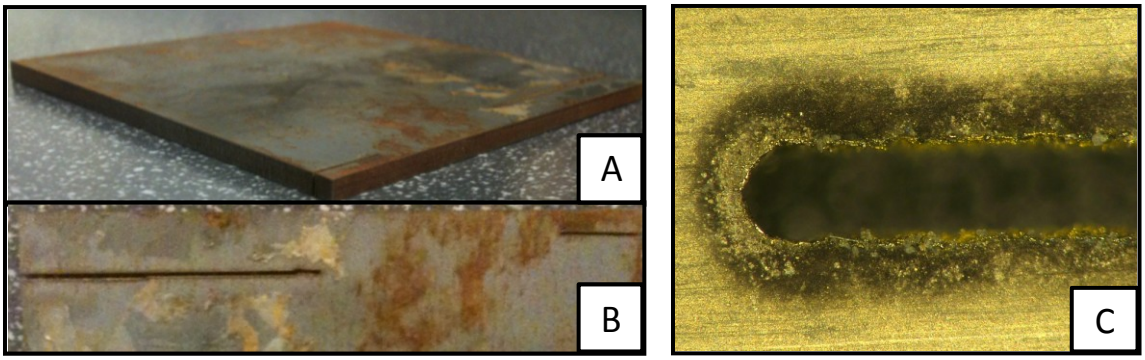

Figure 2.1 (A) Laminated stack of electrical steel cut via wire EDM. (B) Top view of Image A. Significant rusting is visible along the edges and surface of the stack. (C) Microscope image of wire EDM cut of a single laminate. Oxidations and corrosion is clearly visible along the edge of the cut

2.2.2 Laser Beam Machining

The mechanism of material removal during laser beam machining includes different stages such as (i) melting, (ii) vaporization, and (iii) chemical degradation (chemical bonds are broken which causes the materials to degrade) as described by Dubey et. al[19]. When a high energy density laser bream is focused on work surface the thermal energy is absorbed which heats and transforms the work volume into a molten, vaporized or chemically changed state that can easily be removed by flow of high pressure assist gas jet (which accelerates the transformed material and ejects it from machining zone). The effectiveness of this process depends on thermal properties and, to a certain extent, the optical properties rather than the mechanical properties of the material to be machined. Therefore, materials that exhibit a high degree of brittleness, or hardness, and have favorable thermal properties, such as low thermal diffusivity and conductivity, are particularly well suited for laser machining. LBM is a flexible process and when combined with a multi-axis workpiece positioning system or robot, the laser beam can be used for drilling, cutting, grooving, welding and heat treating processes on a single machine.

Dubey et. al observed that laser beam machining produces a heat affected zone in the material surrounding the cut[19]. This heat affected zone is the manifestation of changes in the metallurgical characteristics of the material and thus should be minimized. He also noted various manufacturing performance metrics for the process. The max cutting speed noted in an experimental investigation was 5m/min (83mm/sec) in 0.8-2mm thick metal plates. However, the process is very energy inefficient and incorporates numerous process parameters that significantly impact the laser performance.

A significant amount of research effort has been invested into determining the effects that laser beam machining has on the magnetic properties of electrical steels. Baudouin et. al compares continuous laser, pulsed laser, and mechanical cutting of non-oriented electrical steels [20]. The magnetic properties were evaluated and also the internal stresses were measured via X-ray diffraction. He concluded that it was difficult to correlate the internal stresses with magnetic properties. Mechanical cutting (punching) exhibited better magnetic properties than continuous laser cutting (Hc Br mu) for the standard sized samples. Pulsed laser occurred at 12mm/sec while continuous laser occurred at 100mm/sec with a (150 micron spot size).

Baudouin et. al and Belhadj et. al also explored the effects of rapid heating and heat affected zones on electrical steels in efforts to develop analytical models to predict the heat affected zone based on the cutting parameters [21] [22, 23]. Figure 2.3 illustrates the heat affected zone along the edge of a laser beam machined cut. They noted the competing effects of grain growth and induced thermal stress. Thus the modeling of the process proved very difficult and no correlation between heat affected zone and cutting parameters was ultimately determined although significant increases in core loss as a

result of the thermal processing was noted. Other negative effects such as decreases in permeability and coercive field increases were also noted.

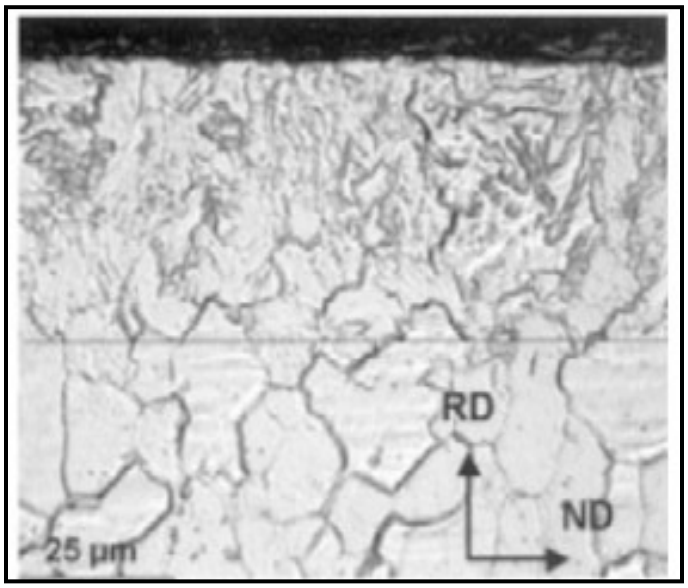

Figure 2.2 (Left) Heat affected zone of electrical steel after being laser beam machined. The sample has been polished and etched. The top portion of the image shows a clear difference in grain structure as compared to the bottom portion [23].

Gaworska-Koniarek et. al explored the effects of the type of assist gas (air vs. nitrogen) used in laser cutting of electrical steels[24]. Air exhibited more degradation of the magnetic properties and the formation of iron oxides which negatively affect the steel's performance.

De Graaf et. al investigated the cutting of aluminum synthetic laminates via laser beam machining[25]. These laminates are a type of newly developed composited material engineered for the aeronautical/astronautical industries. De Graaf developed a model to describe the cutting process; however, interlaminar damage was noted during the cutting process. Figure 2.3 illustrates some of the interlaminar damage incurred via the laser machining process indicating the limited applicability of laser beam machining to the cutting of laminated materials.

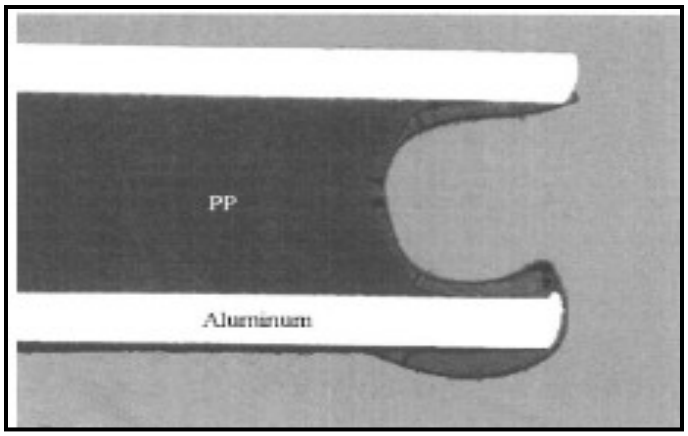

Figure 2.3 Laser machined laminated stack of an aluminum composite. Damage to the interlaminar layer is clearly visible [25].

2.2.3 Abrasive Waterjet Machining

Zeng et. al describe the operating principles of abrasive waterjet (AWJ) machining as the entraining of abrasive particles into a high velocity water stream to cut through materials[26]. The essence of AWJ machining is rapid erosion combined with rapid cooling. In most cases, water does not participate in material removal, but serves as an energy carrier and a flushing medium. Bulk material removal is the result of accumulated micro-cutting effects of individual abrasive particles as in conventional grinding. This is a relatively robust machining process capable of cutting most materials. Previous studies by Schoppa et al and Boehm et. al [27, 28] have shown that AWJ machining has a minimal effect on the magnetic properties of electric steel. However, the work conducted by Boehm was in-fact a parallel study, conducted at the same time as the research presented in this work. Schoppa et. al investigated non-oriented electrical steels and noted that AWJ machining had the smallest impact on magnetic properties as compared with laser beam machining, punching, and mechanical cutting, even though comparatively low cutting speeds of 800mm/min for material thickness of 0.5mm were achieved [28].

Shanmugan et. al investigated using AWJ machining to process laminated stacks of graphite/epoxy composites[29]. He noted significant delamination in this process and attempted to develop a semi-analytical model to predict the delamination. He concluded that the shockwave impact of the waterjet creates crack tips in the composite which is followed by water wedging and abrasive embedment. A descriptive depiction of this process is shown in Figure 2.4. Figure 2.5 Actual photographs of the particle embedment and composite delamination are shown in Figure 2.5. He also studied the machining of alumina ceramics via AWJ machining and was able to develop a predictive model of the kerf taper angle in the process, with a 6.2% deviation between the model and experimental values [30].

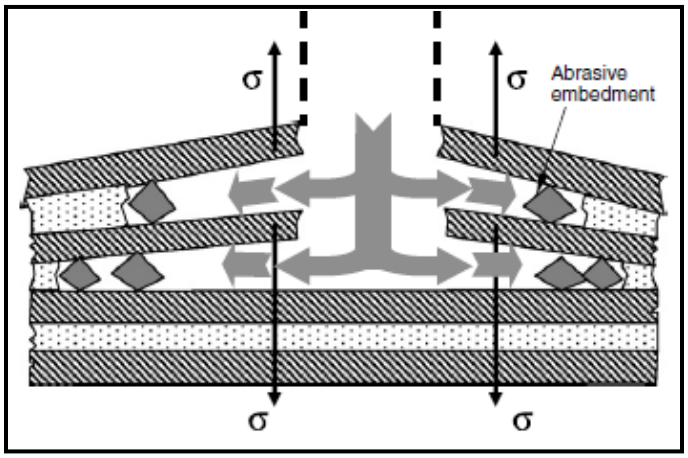

Figure 2.4 Diagram illustrating embedment of abrasive particles as into a laminated workpiece. This embedment results in stresses that act separate the layers leading to delamination of the composite [29].

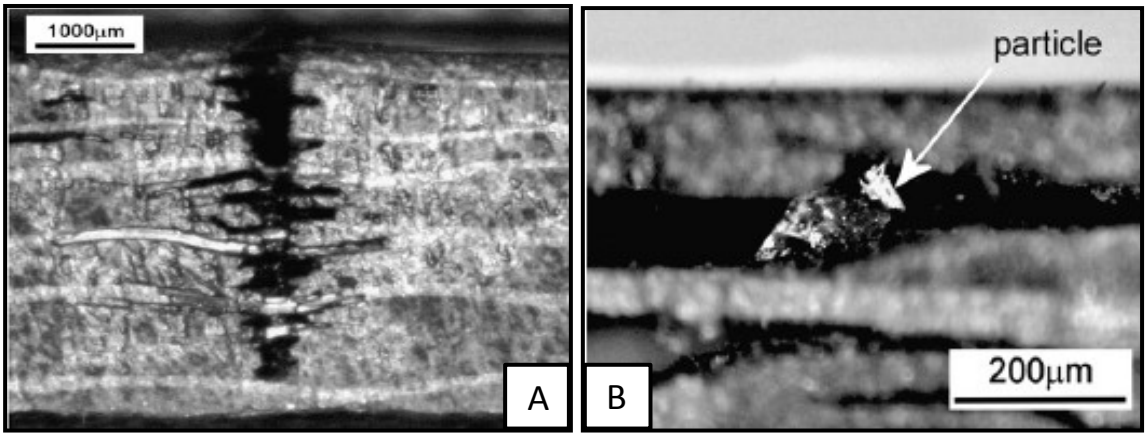

Figure 2.5 (A) Delaminate of a graphite/epoxy composite that was processed via abrasive waterjet machining (B) A magnified view depicting an actual abrasive particle embedded in the composite[29].

Azmir et al and Paul et. al also investigated the machining of composites using abrasive waterjet machining [31, 32]. Paul et. al observed delamination, kerf and burr formation and related the delamination to water pressure during initial penetration of the stack.

In addition to reviewing the literature, some exploratory AWJ machining of electrical steel samples was conducted in house using an Omax 2626 JetMachining Center. Significant burr formation was observed along the edge of the cut with consistent burr heights as high as 190 microns. These burrs can cause problems during assembly of laminated stacks or could potentially cause wiring damage and eventual short circuiting; and thus, must be removed via a secondary processing operation. Furthermore, this process is not suitable for manufacturing of precision micro-meso parts as the parts are easily lost in the waterjet tank during the cutting process.

2.2.4 Mechanical Stamping

Schoppa et. al discusses how cutting or punching and the processes steps associated with producing a laminate stack for the core of an electric machine induces mechanical

stresses which adversely affect the magnetic performance of materials[33, 34]. Samples were tested by increasing the number of slices made in a sample to see the effect of increased cutting on the magnetic performance. It is postulated that the effect of cutting is larger for materials with larger grains and that annealing can help relieve some of these changes. Moses et. al performed similar work investigating the changes in core loss and B-H curve characteristics after the material is cut via a shearing process[35]. He came to similar conclusions that the shearing of the electrical steels results in a decrease in the magnetic performance in and near the sheared region. Several efforts have also been made to predict the magnetic properties via the mechanical deformation that occurs near the cut edge [36-38].

2.2.5 Comparison Studies of Traditional Processing Techniques

Emura et. al compares the effects that different processing methods (namely laser, guillotine, photocorrosion, and punching) have on the magnetic properties of electrical steel[39]. Two percent silicon non-oriented steels were used and measured at 1.5 T. The process effects were studied in as cut and annealed conditions after the cut. Photocorrosion and punching showed the best performance in core loss and permeability just after being cut. Annealing improved the properties of all conditions except photocorrosion.

Kurosaki et al investigated minimizing the deterioration of magnetic properties shearing, laser cutting and wire electric discharge machining when producing motor cores. Cutting method and clamping technique significantly influenced properties[40]. Wire EDM had the lowest core loss and had the best wire magnetizing force with

shearing having the worst magnetizing force. Induction was the same for all. Surface roughness was best achieved via shearing.

Murthy et. al discusses the effects of processing methods on the cogging torque of an electric machine[41]. Laser cut, stamping, and EDM processes have been explored with laser machining having the most significant degradation of performance regarding cogging torque. Stamping is slightly better and wired EDM produced the best performance being synonymous with annealed and stamped processing.

Loisos discuss the debate over whether laser vs. mechanical processing of electrical steel results in the best performance[42]. He notes conflicting studies from other authors concerning whether laser machining or mechanical cutting results in the greatest decrease in magnetic performance. He performs a set of experiments to investigate this debate; however, the laser cutting in this study is performed at an extremely low material removal rate (approximately 4-6mm^3/min) as only a depth of about 2microns of material is removed per pass of the laser. Thus the laser cutting was a very slow process. He successfully achieved minimal degradation of magnetic properties via this technique. He discusses how rapid heating and cooling is the cause of thermal stresses, which are considered harmful on the magnetic properties of the material. On the other hand the high temperatures involved in the laser cutting process may cause a grain growth near the cut edge which is beneficial on the magnetic properties. However which mechanism dominates the laser cutting process remains yet to be understood. The study measured local flux density at various points throughout the material to determine the effects of the cutting process near the cut edge. This study suggests that very small and incremental removal of the material may be instrumental in minimizing magnetic degradation.

2.3 HTPM

HTPM could enable rapid prototyping of electric machines giving designers an increased ability to further advance the development of these devices. As discussed previously these advanced electric machines often are miniature in size and even the larger stators and rotor components often have intricate microscale features such as stator/rotor poles shoes, internal fillets, or very thin teeth. Furthermore, in order to minimize material waste, the smallest tool possible should be used during typical a profile milling process which also suggests the use of microscale tools and machining processes. Consequently several cutting models that have been previously published in the literature regarding micromachining were investigated in order to effectively understand and predict the process analytics (particularly the cutting forces) for machining laminated stacks of electrical steel. Malekian et. al recently discussed a model developed for micro-milling cutting forces which takes into account the effects of plowing, elastic recovery, tool run-out, and the overall dynamics of the machine tool[43]. The paper states that there are two regimes of cutting: 1) relying on shearing forces and 2) relying on plowing forces. The transition from one regime to another occurs at a critical chip thickness (when the chips become so small that the tool nose radius becomes relatively large in comparison). This is an extension of the work conducted by Basuray et. al who also investigates the transition from cutting to plowing [44]. Moreover the mechanics of cutting forces in the micro-regime has been extensively studied by several authors, of which Mayor et. al, Volger et. al, Kim et. al, and Joshi et. al are a few [45-50].

Li et. al, Zaman et. al, and Bao et. al discusses and develop end milling models developed to determine cutting forces [51-53]. These models all are based on an initial foundation developed by Tlusty and McNeil for determining cutting forces[54].

Much of the research investigating milling of laminated stacks focuses on machining carbon fiber or glass fiber reinforced composites[55-59]. After a review of over 31 publications, ranging from 1992 to the present, specifically investigating the processing methods of electrical steel laminates, no existing research concerning the milling of laminated stack of electrical steel could be found in the literature. The only remotely similar work was conducted concurrently with this work and has recently been published in conference proceedings. In a parallel study, Boehm et. al investigated turning of electrical steel and the effects on magnetic properties[27]. Their results agree with findings of other researchers (concerning the performance of AWJ machining) suggesting that AWJ machining and mechanical machining produce components exhibiting similar magnetic performance with minimal degradation.

Boehm et. al also investigated a new means of producing electric machines using only machining processes[60]. In this study turning and drilling were utilized to produce motor core components although little information is given concerning the process parameters of these machining processes. Furthermore, this work seems to be more exploratory in nature aiming to develop a novel electric machine design as opposed thoroughly characterizing the performance of a machining process. Thus it does not seem that the machining process was analyzed with scientific rigor from a manufacturing science perspective. This presents a research opportunity to more thoroughly investigate

the mechanical machining process (particularly high throughput profile milling), its mechanics, effects on material performance, and the optimization of the process.

The conventional machining resources (Kalpakjian, Tlusty, and Machinist handbook texts[61-63]) in addition to data sheets provided by the manufacturer were consulted to obtain proper cutting conditions for processing this material. These did not provide the proper cutting conditions for processing electrical steel via HTPM nor were specific cutting energies provided for this material. Furthermore, as production of electrical steel laminates is a previously unexplored application of this process, little relevant material property information such as specific cutting energy or ideal cutting speeds and feeds is available in the literature. Thus, using HTPM to shape electrical steel laminates is a previously unexplored process and little pertinent knowledge is available to aid in the optimization of the machining parameters. Critical material properties and process parameters namely specific cutting energies, typical cutting speeds or feed rates, in addition to the material's mechanical and magnetic response while undergoing intermittent mechanical deformation (e.g. milling) are undefined for this specific type of material.

2.4 Summary and Identification of Research Gaps

The literature has been reviewed to investigate the traditional processing methods for producing electrical machine laminates. In order to achieve accelerated prototyping of electric machines, these processes must yield minimal degradation of magnetic properties, accurately produce the desired components, and accomplish these two goals at a high rate of productivity. Furthermore, the process must be flexible in that it can

quickly and cheaply adapt and produce different components per the designer/optimizer's request.

Stamping is an effective means of producing electric machine components in that it can achieve tight geometrical tolerances at very high production rates. Although it does have some effect on degrading the magnetic performance, the process produces some of the best magnetically performing components compared to the other processes investigated. Even though it is a very fast processing method, it is highly inflexible to design changes due to high die and equipment costs. Thus, this process is not particularly well suited to accelerated prototyping of electric machine laminates.

Wire EDM/EDM typically has a very slow material removal rate and also induces a recast layer at the cutting surface in addition to corrosion from the water dielectric. The wire EDM processes submerges the workpiece in de-ionized water which can also lead to rapid corrosion and rusting of the electric steel. Wire EDM, on the other hand, is very flexible in that it can easily cope with part to part variation (sudden changes in geometry or design); however, it is a thermal process. Therefore, it can be expected that high thermal gradients induced into the electrical steels during these processes will have an impact on their grain structure and consequently their magnetic properties and overall performance. This is manifested by the heat affected zones and significantly degraded magnetic performance observed by previous studies considering heating effects on electrical steels. However, these effects are quite complex and currently not completely understood. The slow material removal rate and potential heat effects limit effectiveness of the EDM process to achieve accelerated prototyping despite its flexibility.

Abrasive waterjet machining has significant difficulty machining laminated stacks. Especially in generating the initial holes which is necessary for internal features. The forces from the high pressure jet results in significant delamination. Furthermore burr formation and kerf are major problems yielding unacceptable parts or requiring timely secondary processing. Finally, the water in which the electric steel is submerged and cut with, leads to considerable rusting along the edge and surface of the steels. Nevertheless, this process yields minimal degradation of the magnetic performance of these steels and is also highly flexible. However, its material removal and productivity are relatively low.

Laser cutting induces a heat affected zone around the edge of the cut that negatively affects the magnetic properties of the material and consequently the performance and efficiency of the resulting electric machine. The confusion concerning the performance of laser cutting vs. mechanical cutting and mixed conclusions from different suggests that the multiple parameters that go into cutting electrical steel and their effect on the magnetic properties are not well understood. This process however can attain high cutting speeds and is very flexible. Furthermore given the proper parameters and lowering the material removal rate minimal magnetic degradation can be achieved. However, this process also has difficulty processing laminated stacks of material.

Several of the comparative studies investigating electrical steel processed via EDM have shown that this process can result in more favorable magnetic properties than the other processes being considered. This could be due to the small and incremental removal of material despite the fact that it is a thermal process. A study considering laser beam machining has also reinforces this concept. Removing very small amount of material (very small depths of cut) resulted in less material degradation. Finally, AWJ machining

also exhibited minimal degradation of material properties. These indications suggest that HTPM should also have minimal degradation of the magnetic performance of these electrical steels, due to the small area undergoing mechanical strain in the milling process. This process is capable of very high feed rates and, since its material removal rate is a function of the spindle speed, extremely high spindle speeds should enable higher material removal rates while maintaining a material removal strategy of incrementally removing small pieces of material. Furthermore, HTPM can potentially process stacks of electrical steel which can increase productivity greatly. Milling is a complex process and multiple efforts to model it and the associate cutting forces have been realized. However, as with any process, the proper processing parameters are necessary to properly machine these electrical steels, especially considering their high toughness and sensitivity to grain deformation. No relevant processing information is readily available and thus a set of experiments can be conducted to determine these parameters. These experiments have the potential to realize a novel process capable of effectively meeting all the requirements of an accelerated prototyping process for producing electric machines.

CHAPTER 3

DEVELOPMENT OF A MECHANISTIC MODEL FOR THE CUTTING RESPONSE OF M-19 ELECTRICAL STEEL

3.1 Introduction

The application of high-throughput profile milling to the agile production of stator and rotor laminates of advanced electrical machines requires a thorough understanding of the cutting response of the electrical steels. This chapter presents an empirical investigation of the plastic response of the high silicon content electrical steel M-19 and establishes the specific cutting energy and force ratio of the steel at different chip loads. A sequence of experimental studies were conducted to provide an understanding of the material response, produce a model for the specific cutting energy of the material, and produce a mechanistic force predicting model. These models are empirically based but are subsequently validated via additional testing. The experimentation is conducted using a coarse-fine approach, first investigating a broad range of factors and then narrowing the scope while increasing the resolution of the testing conditions. First, a three factor, two level, preliminary experimental study is completed to investigate the effect of the machining parameters of feed per tooth, axial depth of cut, and spindle speed on the cutting response of the electrical steel. Insights obtained from this study motivated a secondary detailed investigation which utilized a two factor, five level experimental test matrix to further analyze feed per tooth and depth of cut. Finally, these two studies provided a sufficient data set to construct the specific cutting energy models and mechanistic force predicting models.

3.2 Analytical Model

An analytical force model of the endmilling process adopted from Tlusty and McNeil [61] was utilized in this study to evaluate and predict the cutting forces. This model utilizes the following three assumptions to compute the cutting force:

$$F_T = K_s b h \tag{3.1}$$

$$F_N = K_r F_T \tag{3.2}$$

$$h = f_t \sin(\theta) \tag{3.3}$$

Equation (3.1) states that the tangential cutting force F_T is proportional to the chip cutting area (where *b* is the axial depth of cut and *h* is the uncut chip thickness) by the constant known as the specific cutting energy K_s. Equation (3.2) describes how the normal cutting force F_N is proportional to the tangential cutting force by the force ratio (K_r). This ratio (K_r) is typically assumed as 0.3; however; due to the exotic nature of this material, this value must be determined in addition to the specific cutting energy. Finally, Equation (3.3) assumes that the motion of the tool path can be approximated as a circular arc, which advances by the feed per tooth f_t with each successive pass. The $\sin(\theta)$ component of the Equations accounts for the location along the circular path that the tool tip is located at a given point in time, in which θ is the cutter rotation angle. This angle is measured from the point at which the first tooth enters the cut as can be seen in Figure 3.1. The value of this angle is often approximated to be 90 degrees to obtain a conservative estimate of the amount of material to be removed. Thus *h,* which is referred to as the undeformed chip thickness, corresponds with the commanded feed per tooth. Consequently, these two terms are referred to synonymously throughout this study.

Figure 3.1 illustrates the cutting process and the orthogonal cutting model utilized in this analysis.

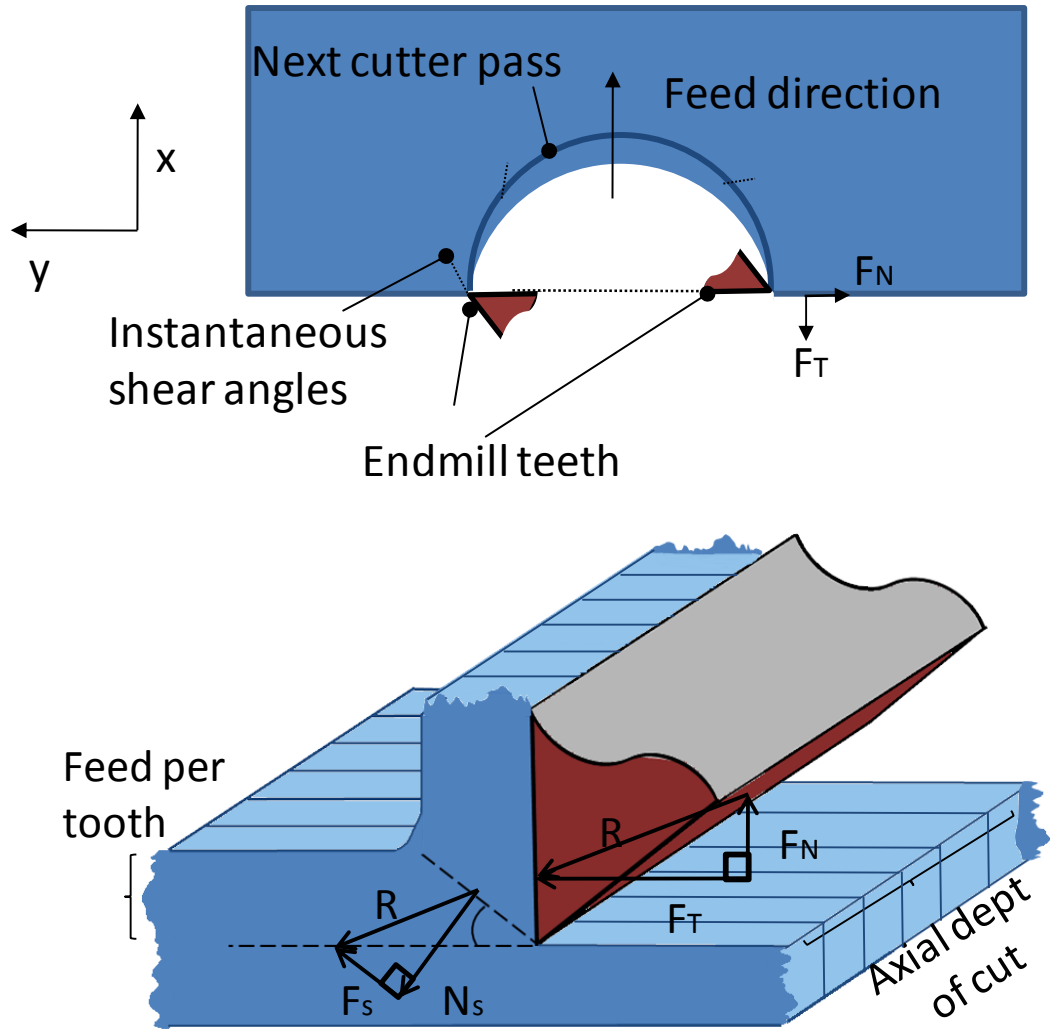

Figure 3.1 Orthogonal cutting model. Top figure illustrates slot milling process. Bottom figure depicts cutting forces of a tooth cutting through a laminated stack.

These equations can be combined to predict the cutting force applied by the tool during the machining process. Equation (3.4) and Equation (3.5) are the functions used to predict the cutting forces in the x and y directions which correspond to the crossfeed and feed directions respectively. These forces can be converted into normal and

tangential forces (Equation (3.6) and Equation (3.7) respectively) via simple algebraic manipulation.

$$F_x = K_s bh(K_r \sin(\theta)\cos(\theta) - \sin^2(\theta)) \tag{3.4}$$

$$F_y = K_s bh(K_r \sin^2(\theta) + \sin(\theta)\cos(\theta)) \tag{3.5}$$

$$F_T = -F_x \sin(\theta) + F_y \cos(\theta)) \tag{3.6}$$

$$F_N = F_x \cos(\theta) + F_y \sin(\theta)) \tag{3.7}$$

These forces can also be combined via vector addition to obtain a planar resultant force as shown in Equation (3.8). The axial force was neglected in this simplified two dimensional cutting model due to its small magnitude relative to the other two forces, which is a result of the small helix angle of the endmills used in this study.

$$F_{\mathrm{Re}sul\tan t} = \sqrt{F_x^2 + F_y^2} \tag{3.8}$$

More advanced analytical force models have been developed to more accurately predict cutting forces in micro-scale machining[51, 53]; however, these models are significantly more complex. Bao and Tansel's cutting force model is one such model considered as an alternative more precise predictor of cutting forces due to the fact that it incorporates the actual trochoidal trajectory of the cutting edges. [52] This model utilizes the same three assumptions mentioned above in the Tlusty and McNeil model, however, it incorporates additional terms into Equation 3 to correct for the actual trajectory of the cutting tooth. Equation (3.9) shows this modification.

$$h = f_t \sin(\theta) - \frac{m}{2\pi r} f_t^2 \sin(\theta)\cos(\theta) + \frac{1}{2r} ft^2 \cos^2(\theta) \tag{3.9}$$

It is important to note however, that Bao and Tansel's model converges with Tlusty and McNeil's in conventional macro-scale milling. However, as the ratio of the feed per

tooth to the tool radius f_t / r increases beyond a critical value, the two models diverge as the circular arc assumption becomes no longer valid. In typical micromachining high feed rates are incorporated to maximize material removal rates and maintain productivity. Bao and Tansel's model was considered to aid in the analysis of this study, but due to the dimensions of the tool radius and feed per tooth selected for this study the Bao and Tansel's model actually yields identical force predictions. More specifically, the maximum f_t / r ratio studied in this investigation was 0.04 occurring at the highest feed rate capable on the machine while operating at maximum spindle speed (32 microns per tooth at 80,000rpm). Bao et. al states that the cutting force models show significant deviation (15%) at ratios of greater than 0.1. [52] Thus under the cutting conditions investigated in this study, no significant deviation is expected between Bao and Tansel's model and Tlusty and McNeil's model.

Figure 3.2 shows the cutting force waveform for Tlusty and McNeil's cutting force model in an altered coordinate system. The coordinate system has been adjusted to correspond with the force readings recorded by a force dynamometer during experimentation. The net resultant force is also shown in Figure 3.2. Figure 3.3 shows the cutting force model for Bao and Tansel's cutting force model.

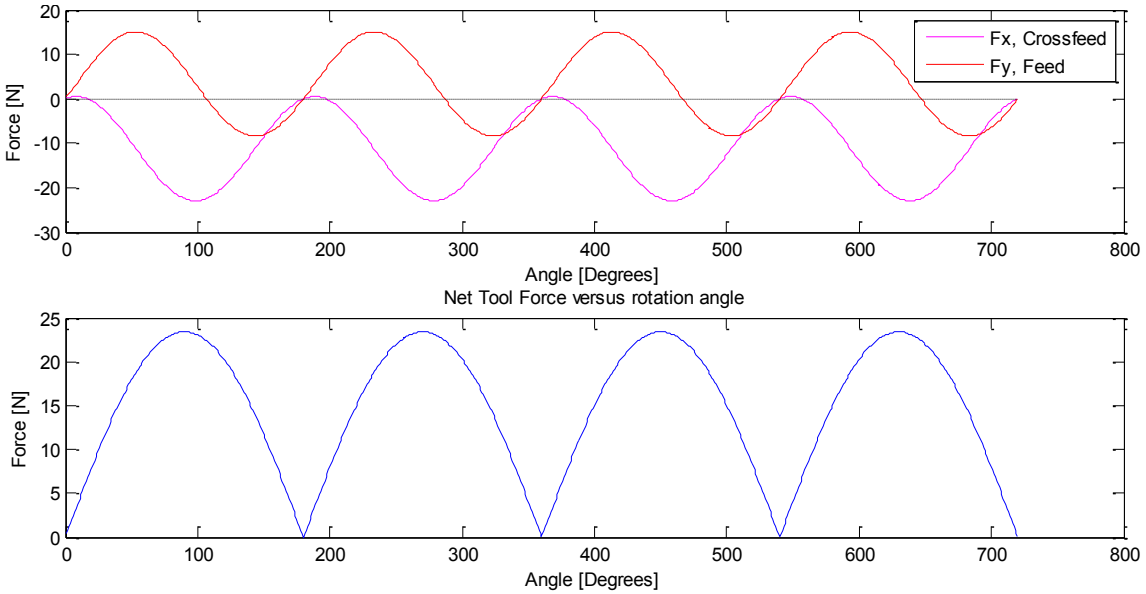

Figure 3.2 Tlusty and McNeil's cutting force model. The top plot shows the planar cutting force components as a function of cutter rotation angle. The bottom figure shows the resultant cutting force as a function of cutter rotation angle.

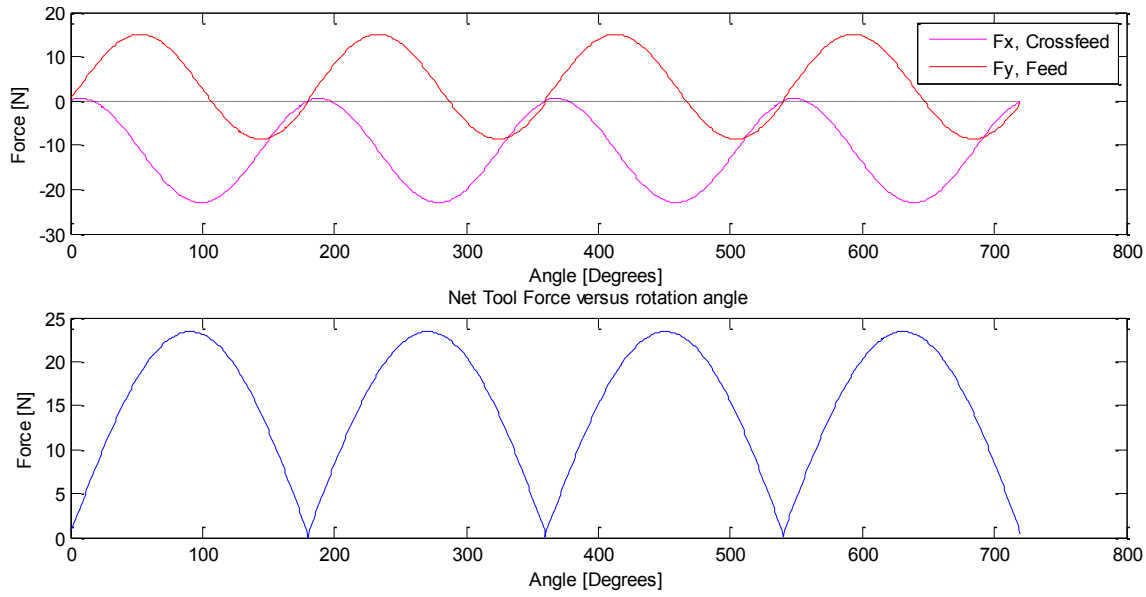

Figure 3.3 Bao and Tansel's cutting force model. The top plot shows the planar cutting force components as a function of cutter rotation angle. The bottom figure shows the net cutting force as a function of cutter rotation angle.

These figures were conducted under the same conditions using the specific cutting energy of a typical stainless steel and show identical force readings, illustrating the

convergence of the tool models and the relative effectiveness of Tlusty and McNeil's model at predicting cutting forces as compared to another more advanced model. Thus Tlusty and McNeil's model was selected to continue the analysis in this study.

It is important to note that the utilization of the cutting force model in this study is specifically aimed at determining the specific cutting energy and force ratio required to process the material via milling. Thus forces were experimentally measured and combined in conjunction with the analytical force model to compute the specific cutting energy and the cutting force ratio.

3.3 Apparatus and Experimental Setup

The same experimental setup, tooling type, and apparatus is utilized for both the coarse and the fine study. The machining tests were conducted on a customized desktop CNC milling center. The machine setup utilized an NSK America E800z 80,000rpm spindle and exhibited a feed capability of 50mm/second. Tooling consisted of two flute, helical endmills with diameters of 1.5875mm (1/16") specified by the manufacturer. The endmills were composed of uncoated, ultra-duty sub-micrograin carbide, with a 30 degree helix angle. The cutting depth was also 4.7625mm (3/16") with an overall length of 38mm (1.5") and the cutter tapers up to a 3.175mm (1/8") shank. The diameters of the endmills were measured under a digital microscope and averaged to yield and actual diameter of 1.519mm. Furthermore the edge radius of the tool flutes (which was not supplied by the manufacturer) was approximated to be 3.685 microns by viewing the end of the tool under a microscope and fitting a circle to the tip of a flute (see Figure 3.4). Due to the fact that the flutes of the endmills are helical, it is quite difficult to measure

the actual edge radius of the cutting edge, thus the approximated radius is used loosely to give an estimate of the tools geometry. No cutting fluid was used during these tests.

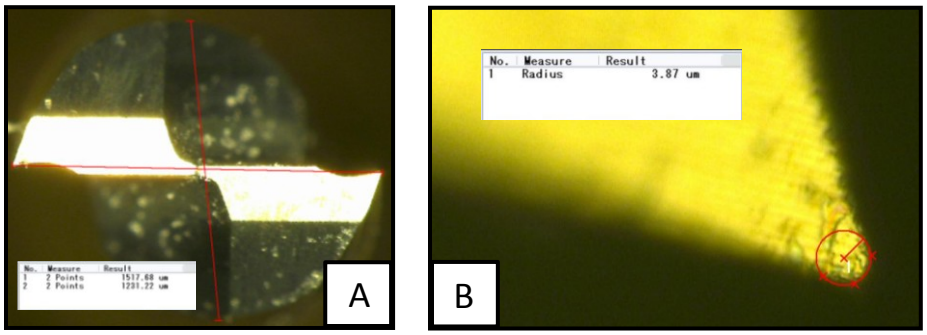

Figure 3.4 (A) View of endmill tip and cutting diameter (B) Microscope image of endmill tip to approximate cutting edge radius.

The laminate stack was mounted atop a set of machined aluminum risers to enable through-cut slotting of the steel without damaging the dynamometer. The risers and the laminate stack were rigidly held in place by a steel beam that crosses perpendicular to the risers and secured directly to the dynamometer by a pair of bolts. Figure 3.5 displays the setup used during testing.

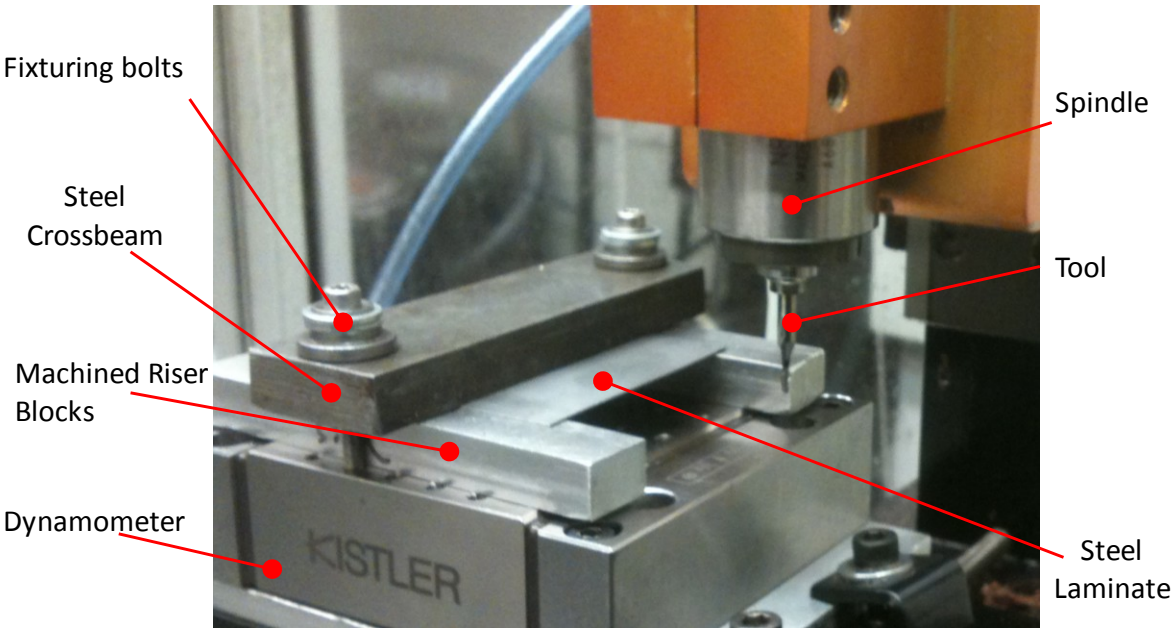

Figure 3.5 Machining set-up used during this study

A Kistler MiniDyn Type 9256C2 is used to record the forces measured during the cutting process. A Kistler Type 5814B1 3 Channel Charge Amplifier which converts the charge produced by the dynamometer to a voltage signal is read by a LabVIEW DAQ NI PCI 6132 card and recorded onto a desktop computer via LabVIEW Signal Express. The force data was recorded at a sampling rate of 120KHz. The force signals were then digitally processed using a low-pass filter set at 3000Hz to remove noise. This filter was selected above any of the expected excitation frequencies of the cutting process (specifically the tooth passing frequency) to avoid altering the data to be analyzed. A Fast Fourier Transform (FFT) analysis was conducted on the raw signal and the filtered signal and the frequencies and amplitudes of the dominant peaks were exactly the same, thus validating that the energy content of the signal is the same and that the filter does not significantly affect the desired data. Furthermore, no significant energy content was observed in the raw signal about the filter cutoff frequency which validates the selection of this frequency as an appropriate cutoff frequency.

In addition to recording cutting forces, the motion profile of the test was also recorded. The motion controller of the CNC machine tool in conjunction with high resolution rotary encoders outfitted on each stage was utilized to also record the instantaneous position of the stage during the experimental cuts. A sample of the velocity profile of one of the tests is shown in Figure 3.6. Slight dynamic effects occur at the beginning of the motion as the system attempts to quickly reach the desired command velocity. Precautions are made to minimize the effects of this dynamic response. First, the tool is moved sufficiently far enough away from the workpiece such that the initial 0.2 seconds of dynamic ringing will occur before it engages the workpiece. This can be

accurately accomplished by predicting the distance that the stage will move after 0.2 seconds using the commanded velocity. Furthermore, to mitigate any potential dynamic effects occurring due to the entrance and exit of the tool into the workpiece, the force data during the middle of the cut is selected for use in the study. Due to the high spindle speed and high sampling rate of the dynamometer only a small section of the recorded force data is required. Thus, selecting this central section of the data set will provide sufficient and the most accurate data as it will approximate a steady-state cutting condition.

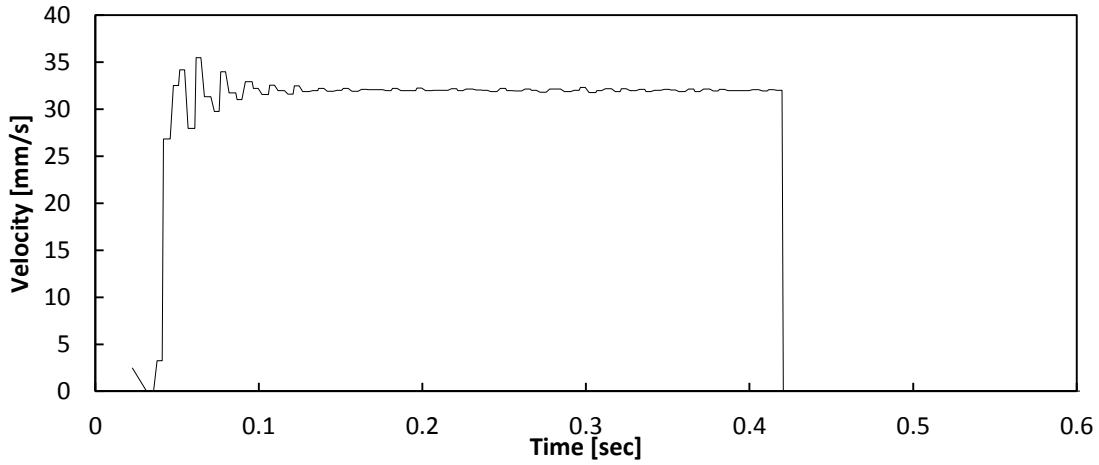

Figure 3.6 Velocity profile of machine tool motion during a cutting trial.

3.3.1 Laminate Stack Preparation Methodology

The laminate stacks used in this research were prepared using fully processed electrical steel and an epoxy resin. The electric steel was first cut into 50mm x 50mm squares using a mechanical shear. These individual laminates were then stacked with a layer of epoxy resin sandwiched between each individual layer. The entire stack was then placed inside a specially designed compression jig which squeezes the entire stack under uniform pressure of approximately 18 MPa. Initial results and analysis indicated that this

was a satisfactory pressure to obtain acceptable stacking factors while also not yielding the electrical steel. This compression serves to remove the excess epoxy from between the individual layers. The high pressure causes the excess epoxy to flow out the sides of the stack. The stack is then allowed to cure while still under compression for the specified curing time as indicated by the resin manufacturer. After this process has been completed the stack is removed from the jig and the excess epoxy is removed from the edges of the stack. The design of this jig is further discussed in the following section. Furthermore, the compression is able to achieve a very thin layer of epoxy between the individual laminates. Stacking factors (percentage of the stack that is actual electrical steel) of 93% with stack heights as high as 34.7mm were realized. This process enables the production of laminated stacks of varying thicknesses in a consistent and repeatable manner.

3.4 Experimental Approach and Methodology

From a set of initial exploratory cuts it can be concluded that it is indeed possible to machine laminated stacks of electrical steel; however, the process parameters must be carefully selected to optimize the machining process. Typical cutting process parameters for (1000 series) plain carbon steels with similar hardness to M-19 were utilized in the initial exploratory cutting experiments of the laminated stacks; however, repeated tool breakage motivated the use of more conservative feed rates. Furthermore, subsequent analysis indicated that the electrical steel behaved more similarly to stainless steel. Specific machining strategy modifications were incorporated such as cutting near the shank of the tool and through-cut milling in an “overhanging” fixturing arrangement. These modifications were driven by the results of the exploratory cuts and additional analysis in an effort to minimize tool breakage. Performing the milling process via

through-cut slotting enables the tool to be engaged higher up along the shank than normally possible (while still maintaining the same depth of cut, e.g. the thickness of the stack). Ultimately, this analysis and machining strategy was utilized to aid in the design of experiments.

A FFT was also performed on the force data to investigate the energy content of the signal in the frequency spectrum. A characteristic FFT plot is shown in Figure 3.7. The two peaks correspond with the dominant frequencies of the data recorded. They correspond with the tooth passing frequency and the rotational speed which is half the tooth passing frequency (due to the fact that the tool has two flutes). This specific FFT was taken from a test condition with a spindle speed of 20,000rpm corresponding to 333.3Hz (666.67Hz tooth passing frequency for a two flute tool). Furthermore, no other significant peaks are observable in the FFT indicating that most of the energy in the system is going into the cutting process and that there are likely no other unaccounted sources of forcing. Furthermore, the very large peak occurring at the spindle rotation speed also indicates that significant runout was occurring during the cut. Typically most of the energy should be going into the higher frequency peak as each tooth performs its cut into the material.

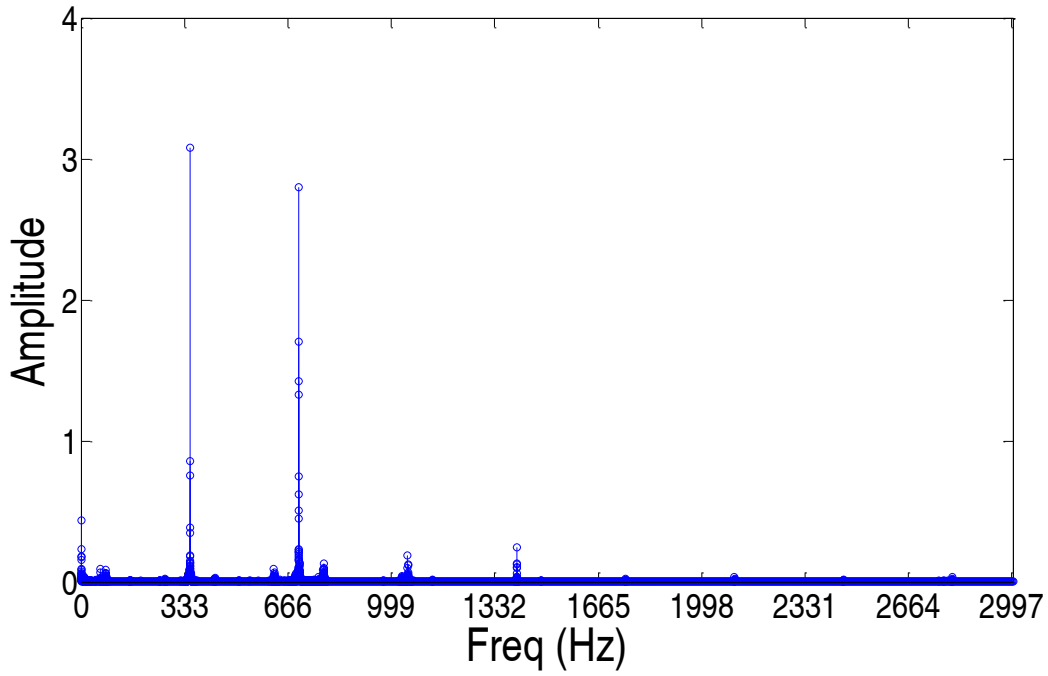

Figure 3.7 Fast Fourier Transform of the force data obtained during a cutting trial.

Figure 3.8 displays a set of characteristic data obtained from one of the cutting trials. This figure shows a time period of four tool rotations with each rotation exhibiting two peaks due to the engagement of the two flutes of the endmill.

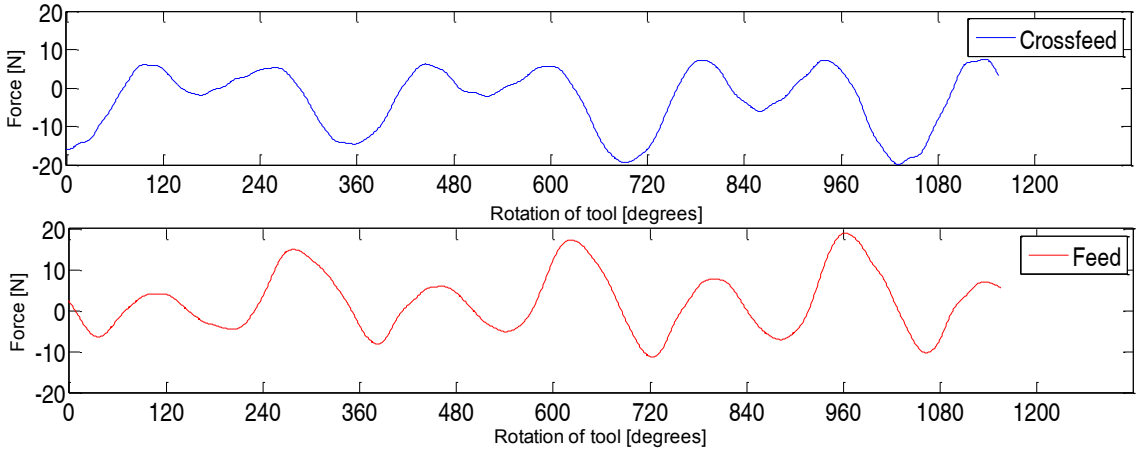

Figure 3.8 Characteristic force data obtained from a cut.

The cutting forces waveform shown in Figure 3.8 should ideally be sinusoidal; however, tool runout and deflection of the tool contribute to cause variation in the curve peaks. The very regular and periodic nature of this variation seems to further suggest that it is caused by runout or some similar forced process. The runout in the waveform also agrees with the FFT data shown above. It is important to note that significant work has already been conducted to investigate the effects of runout in milling processes and to effectively model this phenomenon [64-68]. However, this was not incorporated into the analytical model in detail. In order to account for the runout effects in the data and obtain accurate specific cutting energies and force ratios, two approaches were utilized: (1) The cutting force waveforms are averaged to yield a single point force estimate which is then used to obtain the desired coefficients; (2) A simple scalar adjustment to the uncut chip thickness combined with empirical tuning via a particle swarm optimization algorithm is incorporated to obtain the desired coefficients.

Force Averaging Approach

The first approach, referred to as the force averaging approach, takes into consideration the fact that the runout simply redistributes the chip load during the cutting process[69]. Consequently, the force curves in the feed and crossfeed directions can be averaged to a single point estimate, and then the specific cutting energy can be determined based off this average value and the maximum uncut chip thickness. The cutter rotation angle can be assumed to be 90 degrees from the entrance of the cut resulting in the feed and crossfeed forces correlating to the normal and tangent forces respectively. Figure 3.9 and Figure 3.10 display the measured force data along with the averaged single point estimate value for both the feed and cross feed directions.

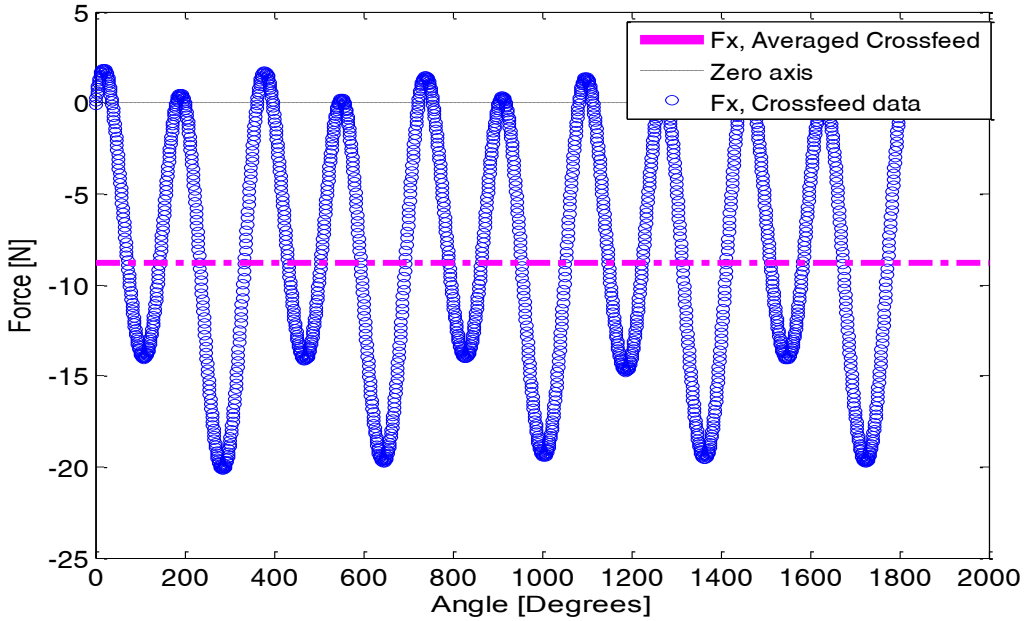

Figure 3.9 Averaged single point estimate of cutting forces in the crossfeed direction compared to the measured data for the corresponding direction.

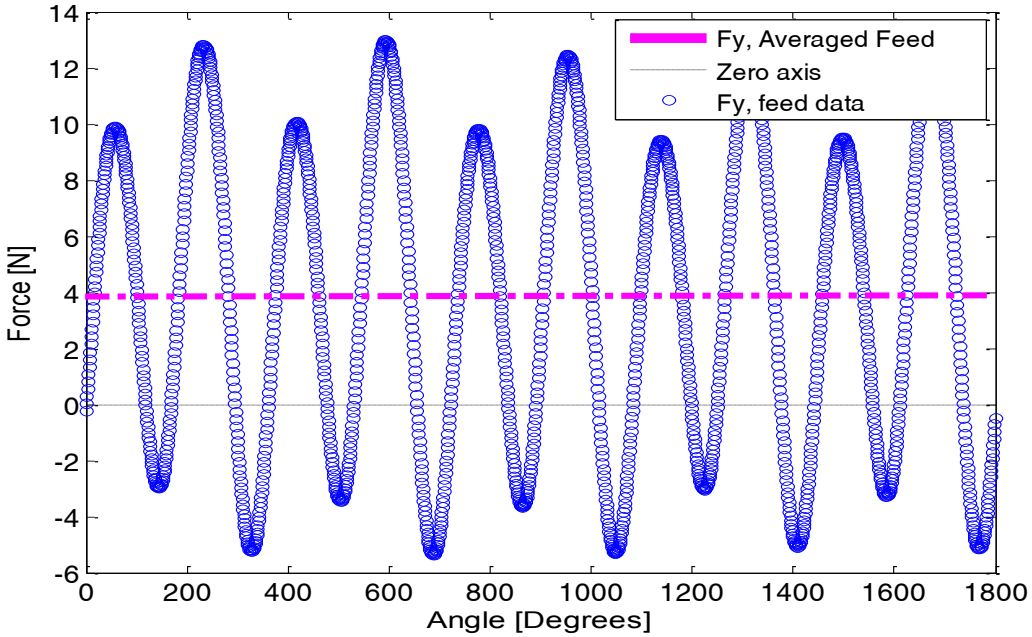

Figure 3.10 Averaged single point estimate of cutting forces in the crossfeed direction compared to the measured data for the corresponding direction.

Empirical Tuning Approach

As previously mentioned, the second approach incorporated a simple scalar adjustment of the uncut chip thickness in the analytical model. Equation (3.10) and

Equation (3.11) show the function used to modulate the uncut chip thickness where E is the tool runout term.

For tooth 1 ($0° < \theta < 180°$): $$h = f_t \sin(\theta) + E \tag{3.10}$$

For tooth 2 ($180° < \theta < 360°$): $$h = f_t \sin(\theta) - E \tag{3.11}$$

This modification should enable the model to make some considerations of the runout when determining the specific cutting energy and force ratio coefficients. Based on Equation (3.3) and as can be observed in Figure 3.2, the maximum force will occur when the endmill tooth has rotated by 90 degrees into the cut. Thus, the experimental resultant force peaks are averaged yielding a characteristic resultant force for the condition, F_{Char}. However, after combining the experimentally measured forces to compute the resultant force, a distorted waveform is obtained in some cases. This distortion is due to noise in the force signal caused by cutting dynamics, tool runout, and workpiece vibrations. The peaks of this distorted waveform do not correctly correspond with the predicted cutter angle of 90 degrees. Thus correlating the cutter rotation angle of the experimental and analytical model is not trivial.

Consequently, a particle swarm optimization algorithm is used to match the measured cutting forces to the predicted values via minimizing the least squared error between the model and the data. Figure 3.11 displays a flow chart that summarizes the algorithm. Furthermore, Table 3.1 displays the parameters used in the optimization. Specifically, force ratio *Kr*, *Ks,* tool runout, and the phase misalignment between the analytical model curve and the experimental data curve were selected as the variables to be optimized. This enabled a relatively robust algorithm in that simultaneously accounts for multiple variables when fitting the data. The high sampling rate of the dyno provides sufficient

data points to enable the algorithm to accurately compute the specific cutting energy and force ratio.

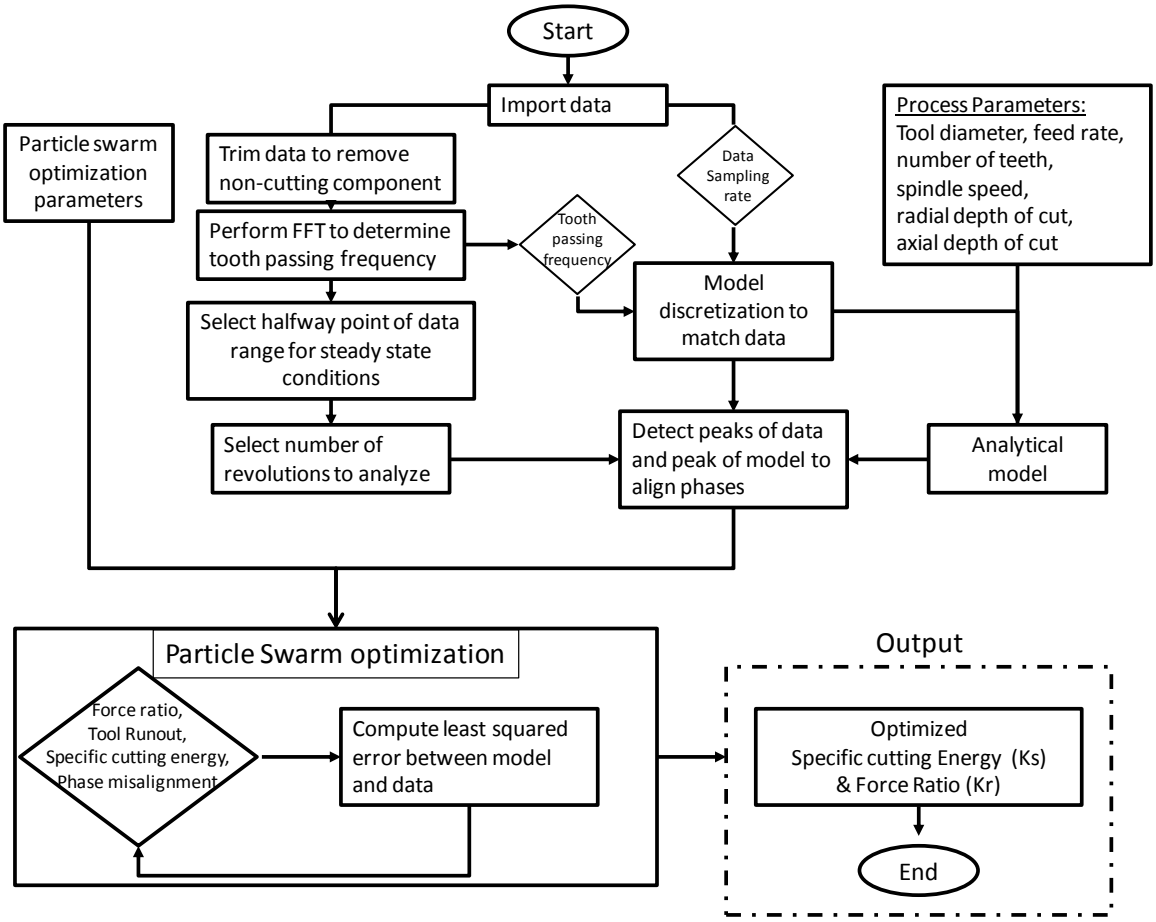

Figure 3.11: Flow chart depicting optimization algorithm utilized to determine specific cutting energy and force ratio.

The runout in this optimization is incorporated into the model by increasing or decreasing the uncut chip thickness via the function shown in Equation (3.10) and Equation (3.11). The phase misalignment between the model curve and the data curve are calculated by locating and determining the distance between the peaks of the curves relative to each other. The curves are then iteratively shifted until their peaks occur at the same time instance. The optimization routine calculates the squared error between the experimental values, denoted with an "exp" subscript, and the values predicted by the

model, denoted with a "model" subscript, as shown in Equation (3.12). The "res" subscript denotes resultant force which is calculated using Equation (3.8). Subsequently, the corresponding coefficient of determination is generated as can be seen in and Equation (3.13), with the bar superscript denoting the average force value. The performance of the optimization routine was evaluated by considering the coefficient of determination value (R^2) and manually inspecting how well the curves for the analytical force model and experimental force data correlate when plotted together.

$$E^2 = \sum\left[(F_{X,\exp} - F_{X,model})^2\right] + \sum\left[(F_{Y,\exp} - F_{Y,model})^2\right] + \sum\left[(F_{res,,\exp} - F_{res,model})^2\right] \tag{3.12}$$

$$R^2 = 1 - \frac{E^2}{\sum\left[\left(F_{X,\exp} - \overline{F_{X,\exp}}\right)^2 + \left(F_{Y,\exp} - \overline{F_{Y,\exp}}\right)^2 + \left(F_{res,\exp} - \overline{F_{res,\exp}}\right)^2\right]} \tag{3.13}$$

Table 3.1: Particle Swarm optimization parameters

Parameters	Values	Units
Range of acceptable values for Ks	0 to 14000	MPa
Range of acceptable values for Kr	0.1 to 3	--
Range of acceptable values for Runout	-1 to 1	mm
Range of acceptable values for Phase Misalignment	-90 to 90	Degrees
Maximum number of iterations	600	--
Population size	100	--
Acceleration constant 1	1.7	--
Acceleration constant 2	2	--
Initial inertial weight	0.2	--
Final inertial weight	0.4	--
Minimal global error gradient	1e-3	--

A characteristic plot of the feed component, crossfeed component, and resultant force waveforms for two tool revolution are shown below in Figure 3.12-Figure 3.14. As expected the empirically determined model does a very good job of fitting instantaneous samples of the data. These figures indicate that the specific cutting energy obtained is a

good description of the energy required to cut the material under the specified cutting conditions. There are some slight fluctuations and deviations but these are likely caused by the dynamic and intermittent nature of the endmilling process. Furthermore, the cutting of the thin laminate induces vibrations which can cause slight variations in the instantaneous uncut chip thickness. These dynamics effects are likely the cause of the slight ascending trend of the peak magnitudes in Figure 3.12 and Figure 3.13. This slight trend is only temporary during the cutting processes and is simply a manifestation of vibration of machining a thin laminate.

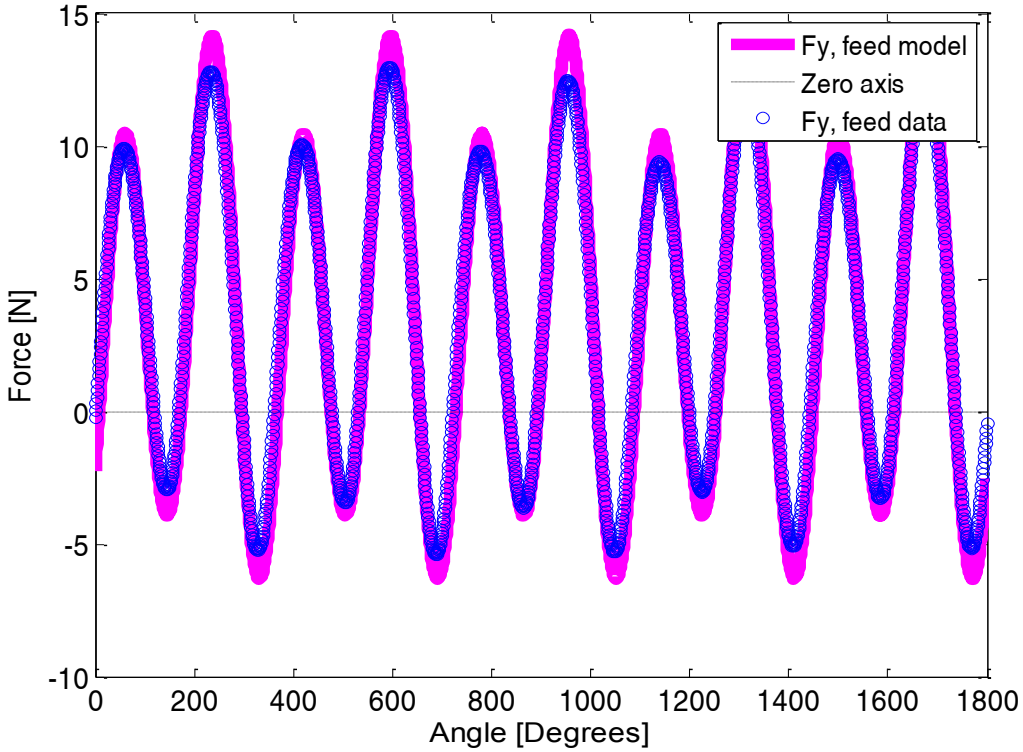

Figure 3.12 Characteristic plot of analytical model of cutting forces in the feed direction compared to the measured data for the corresponding direction.

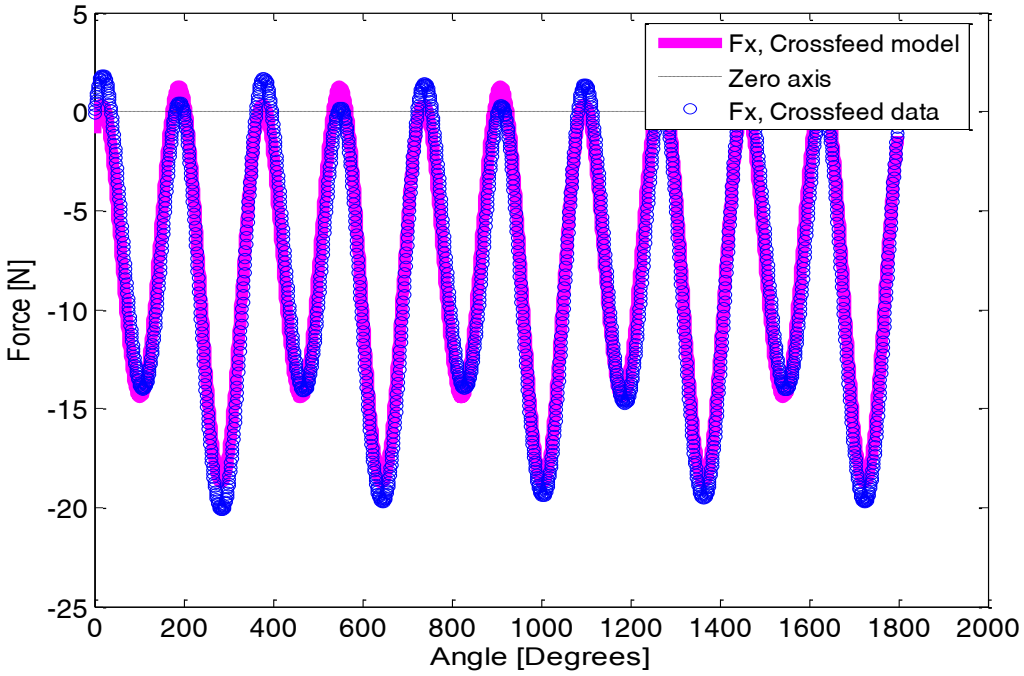

Figure 3.13 Analytical model of cutting forces in the crossfeed direction compared to the measured data for the corresponding direction.

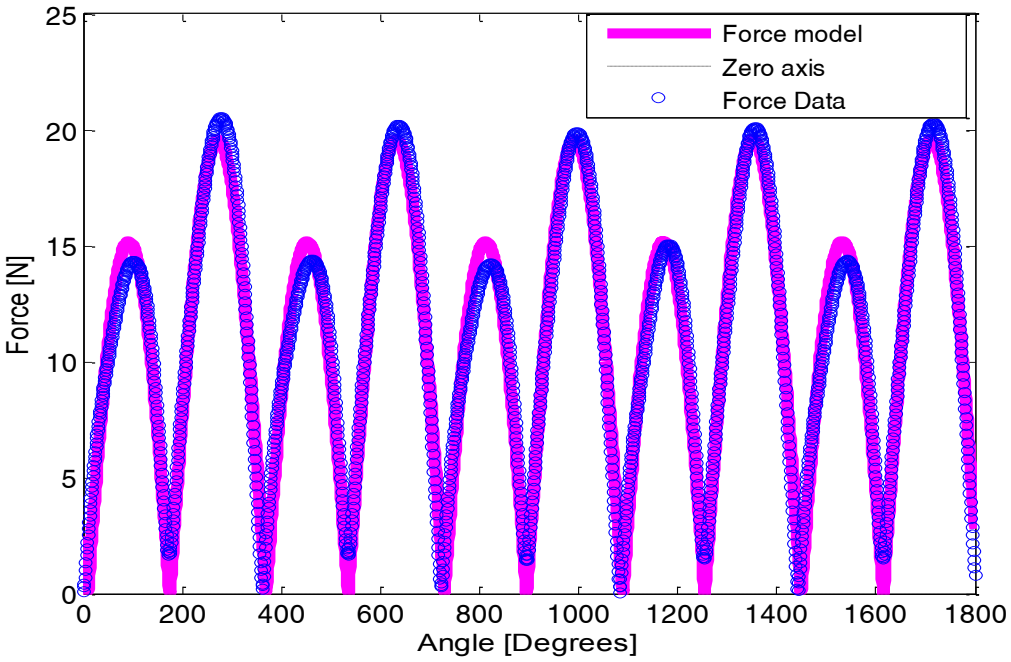

Figure 3.14 Analytical model of planar resultant cutting forces compared to the resultant force data obtained during experimental cutting trials.

3.5 Preliminary Empirical Investigation of Material Properties

The design of experiments is divided into two steps. An initial coarse investigation is conducted followed by a refined investigation after some preliminary understanding of the material has been obtained. M-19 was selected as the electrical steel of choice for this study due to its wide utilization in industry, being one of the more common and cost effective electrical steels.

For the preliminary study a three factor, two level, experimental test matrix was developed and completed to investigate the machining parameters of feed per tooth, axial depth of cut, spindle speed. Three replicates were conducted at each condition. The entire set of 24 tests was also randomized to maintain statistical independence of each individual test. Table 1 shows the test matrix utilized in this study. The tool size of 1/16" was selected to conduct these experiments. This selection was motivated by the design of the previously mentioned ultra high speed spindle. The minimum feature size on the stator and rotor components of this spindle was a radius of 793 microns (~1/32"). This minimum feature size is also the defining factor on the scale of the machining process. This definition of scale defined by Mayor et. al [70] situates the machining process in the micro/meso machining regime.

The depth of cut was fixed by the number of laminates cut at a time. The feed per tooth was chosen based on the insights gained from the initial exploratory tests and from measuring the tool edge radius to be 3-4 microns. A feed per tooth of 2 microns per tooth was below this edge radius and a feed per tooth of 7 microns was above the edge radius of the tool and still achievable with our current machining set-up. These feeds were selected to investigate the potential effects that cutting just above and just below the tool

nose radius would have on the cut. The spindle speeds were selected as a means of bounding the potential spindle speeds to be used during this machining process. Preliminary testing conducted at lower speeds suggested that higher speeds provided better quality cuts. Furthermore, speeds in excess of 80,000rpm are difficult to achieve using conventional electric spindles. Finally, the depths of cut were selected at 50% and 25% of the tool diameter. Due to the laminated nature of the steel this resulted in stacks consisting of a single layer and stacks consisting of two layers. This enabled the study of the material properties of M-19 in addition to its behavior as a laminated stack. These thicknesses introduce forces small enough such that the spindle of the machining center did not overload and the sensing range of the dynamometer was not exceeded. Further, the selection of process parameters was guided to gain preliminary information on the machining of laminated stacks. The initial assumption is that the layer of epoxy resin constrains the stack to behave as one monolithic piece of material during the machining operation.

Table 3.2: Experimental Testing Matrix (Coarse Study)

Case no.	Feed per tooth (microns)	Spindle Speed (rpm)	Axial Depth of cut (microns)
1	2	20000	711
2	2	80000	711
3	7	20000	711
4	7	80000	711
5	2	20000	355
6	2	80000	355
7	7	20000	355
8	7	80000	355

3.5.1 Results and Analysis (Coarse Study)

The preliminary coarse study served as an initial wide field study of the machining of these electrical steels. The data collected consisted of force data measured by the dynamometer. Loud squeals were heard during most of the cutting trials. These sounds could be due to excessive vibrations of the flexible, thin, laminated stack. Even louder, intermittent vibrations, which might be the result of chatter was also heard while machining at the lower feed rates. Figure 3.15 illustrates a full cured laminated stack before and after the machining trials.

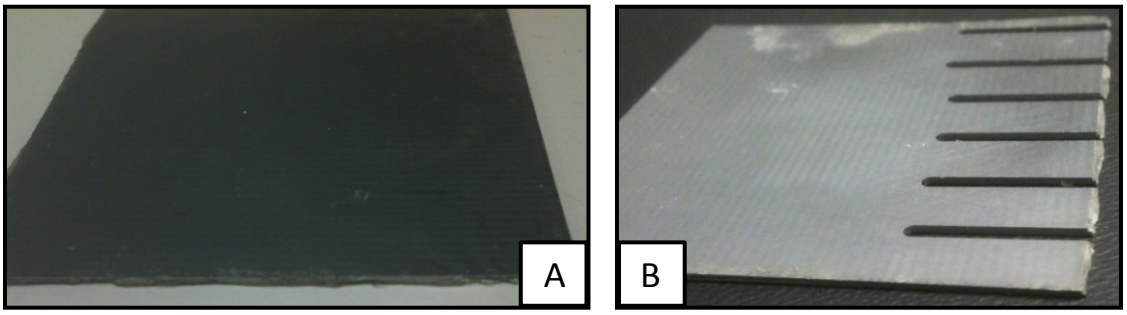

Figure 3.15 (A) Two layer laminated stack after being bonded in the compression jig (before testing). (B) Photograph of sample laminated stack of machining experiments (after testing). The white residue is simply excess epoxy that is still adhered to the stack.

The scalloping that can be observed on the sidewalls of the cut in Figure 3.16 below seems to also validate this theory. This could potential be due to the thin geometry of the single laminate and laminate stack. The effects of chatter were not investigated during this initial study. Moreover, very clean sidewalls were observed along the edge of most of the cuts at high feed rates in the study (see Figure 3.16 B).

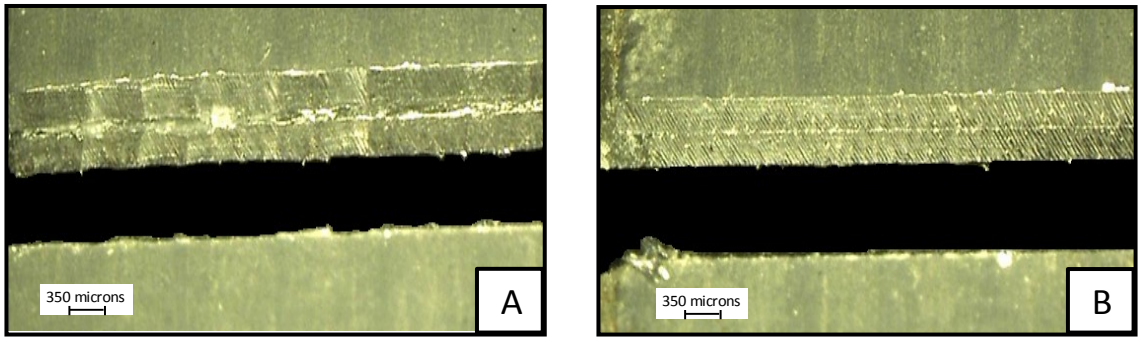

Figure 3.16 Microscope photograph of slot machined into a laminated stack of M-19. (A) Slot cut using low feed rate and low spindle speed. (B) Slot cut using higher feed rates and low spindle speeds.

Resultant planar cutting forces displayed in Figure 3.17 used to characterize and compare different cutting conditions provide insight into the underlying mechanics of the cutting process. Referring back to Table 3.2 the first four cases incorporate a two laminate stack axial depth of cut while the last four incorporate an axial depth of cut equal to the thickness of a single laminate. The even cases correspond to the high spindle speed of 80,000 rpm while the odd numbered cases correspond to 20,000 rpm. Finally, the square data points indicates low feeds per tooth of 2 microns/tooth and the circle data points indicate high feeds per tooth of 7 microns/tooth. It is important to note that at higher axial depths of cut produces higher resultant forces. Furthermore, higher feeds per tooth also result in higher cutting forces. Also, the resultant cutting forces tend to decrease with increasing spindle speed. This happens in at all the conditions except Case 7 and Case 8. One explanation for this is difference is that cutting the single laminate at higher feed rates will likely result in increased vibration and dynamic effects which could influence the measured cutting forces.

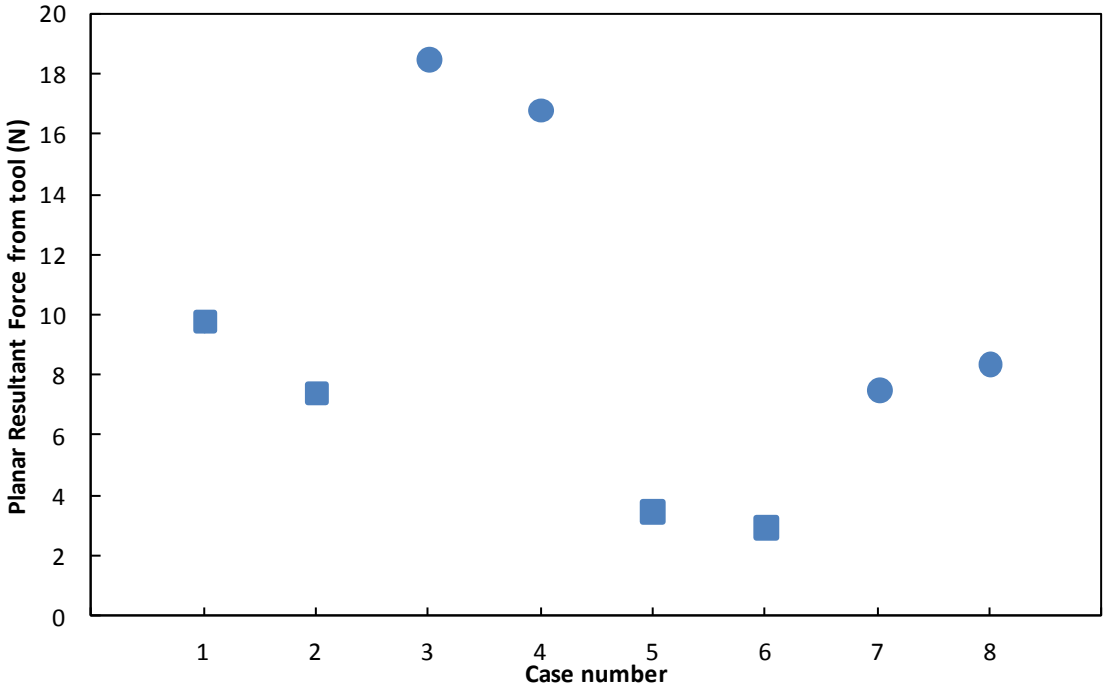

Figure 3.17 Resultant forces in the plane of the laminate (excluding axial component).

The resultant forces observed in this coarse study are indicative of the competing phenomena occurring during cutting at these feed rates and spindle speeds. The force values are influenced by the number of laminates cut at one time (axial depth of cut) and the rate at which the tool advances through the material (feed rate). As predicted by the analytical model, Equations 4 and 5 cutting forces increase as the axial depth of cut and feed per tooth increase; however, an increase in spindle speed yields a decrease in cutting forces. This is clearly shown in Figure 3.17 between cases 1 and 2, 3 and 4. This suggests that the material is sensitive to strain rate which is also a function of cutting speed.

Table 3.3 shows a comparison of some of the cutting characteristic metrics for each of the individual conditions investigated in this study. The specific cutting energy and force ratios were obtained using the empirical tuning approach. It is interesting to note that the two minimum specific cutting energies also occur at the two maximum material

removal rates. Furthermore the maximum specific cutting energy occurs at the minimum material removal rate. These trends indicate that via greater spindle speeds, not only can more efficient cutting be accomplished (as evidenced by the lower specific cutting energies), but also added productivity can be achieved as evidenced by an increased material removal rate. Thus the specific cutting energy which is derived from these observed force values provides a better insight into the cutting process.

Table 3.3 Cutting Characteristics Table

Case No.	Feed per tooth [microns]	Spindle Speed [rpm]	Axial Depth of cut [microns]	Material Removal Rate [mm^3/min]	Specific Cutting Energy [N/mm^2]	Force Ratio (Normal Force/ Tangential Force)	Tool Runout [microns]
1	2	20000	711	90	5934	0.52	0.4
2	2	80000	711	361	4220	0.79	0.0
3	7	20000	711	316	3198	0.48	1.1
4	7	80000	711	1264	2481	0.68	0.2
5	2	20000	355	45	3887	0.84	0.1
6	2	80000	355	180	2880	0.97	0.1
7	7	20000	355	158	2783	0.45	0.6
8	7	80000	355	632	2282	0.84	0.2

3.6 Detailed Empirical Investigation of Material Properties

For the fine study a two factor, five level experimental test matrix is developed to further analyze feed per tooth and depth of cut. The spindle speed was held constant at the highest setting achievable with our current machining setup. Thus the extended tests are all conducted at the highest spindle speed that attainable given our current laboratory equipment. Changes in stack height are still investigated by considering single and two-layer laminated stacks, in addition to exploring the effects of increasing feed per tooth. Three replicates were conducted at each condition. Similar as with the coarse study, the entire set of 30 tests was also randomized to maintain statistical independence of each

individual test. However, in order to minimize set-up time, the single laminate cuts were performed as a single randomized set and the two-layer stack trials were all performed as another randomized set. Table 3.2 shows the test matrix utilized in this extended study. The feed per tooth was chosen based on the limits of our lab machining center (which has a maximum feed rate of 85mm/sec corresponding to a feed per tooth of approximately 32 microns per tooth at a spindle speed of 80,000rpm, and a chip load equal to 2% of the tool diameter). The selected feeds per tooth were thus incremented to cover the entire range of the machine tool utilizing the same spacing as the initial spacing between test conditions of 5microns per tooth.

Table 3.4 Experimental Test Matrix (Fine Study)

Case no.	Feed per tooth (microns)	Spindle Speed (rpm)	Axial Depth of cut (microns)
1	12	80000	355
2	17	80000	355
3	22	80000	355
4	27	80000	355
5	32	80000	355
6	12	80000	711
7	17	80000	711
8	22	80000	711
9	27	80000	711
10	32	80000	711

Experiments were conducted at three different conditions on single laminates so as to only focus on the behavior of the electrical steel itself. They were conducted at the maximum spindle speed of 80,000rpm and feed rates evenly space around the center of the range of experiments with values of 9.5 microns/tooth, 14.5 microns/tooth and 19.5 microns per tooth. Three replicates were performed at each condition and similar to the other tests the order of the testing was randomized to maintain statistical independence.

3.7 Results

Due to the fact that minimum specific cutting energies found in the coarse study are obtained at the maximum cutting speeds, the subsequent (fine study) conducted all of its tests at the maximum available spindle speed and more thoroughly investigated the effects of feed rate and depth of cut. These tests produced similar observable responses as the coarse study, in that audible squeals occurred during the cuts. Slight out of plane deflection of the laminates was also observed at some of the high feed rate, single laminate tests. This is likely due to increased cutting forces and the thin membrane like geometry of the laminate resulting in low flexural stiffness. This occurred even though the laminates were rigidly constrained on three sides. This suggests that appropriate fixturing strategies will be necessary if this process is used at higher feed rates. One potential strategy is to apply in plane tension to the laminate by firmly clamping and pulling on its edges. This tension would increase the stiffness of the laminate and reduce the amplitude of the out of plane vibration. Thoroughly analyzing this approach would require evaluating complex geometric nonlinearities. However, different fixturing techniques were not considered during this study. The observed defection was quite small and only occurred briefly at the beginning of the cut on a few of the trials. As the tool progressed into the material, the laminate quickly returned to its original planar position.

The resultant cutting forces were calculated in the same fashion as discussed in the coarse study. Figure 3.18 shows the resultant cutting forces over the entire range of feed rates investigated. This figure specifically illustrates the forces measure when cutting a single laminate. Thus, they are purely based on the material properties of the M-19 and not that of a laminated structure or the resin used to bind that structure. Figure 3.19

however shows the resultant cutting force for the two layer laminated structure. As expected, all the forces for corresponding feed rates are higher in the two laminate stacks than their single laminate counterparts.

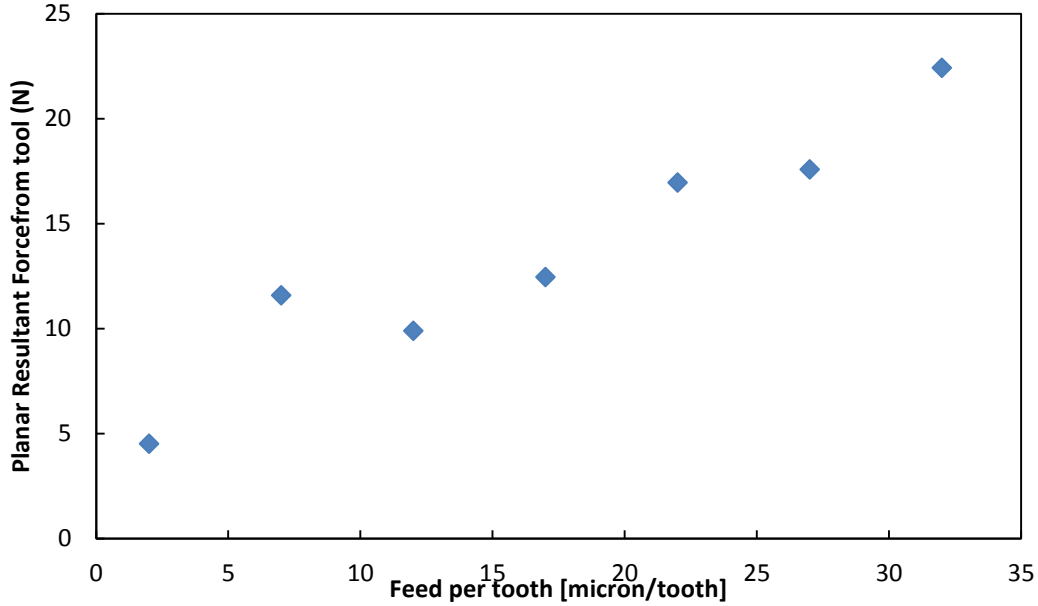

Figure 3.18 Single laminate average resultant cutting forces as a function of feed per tooth.

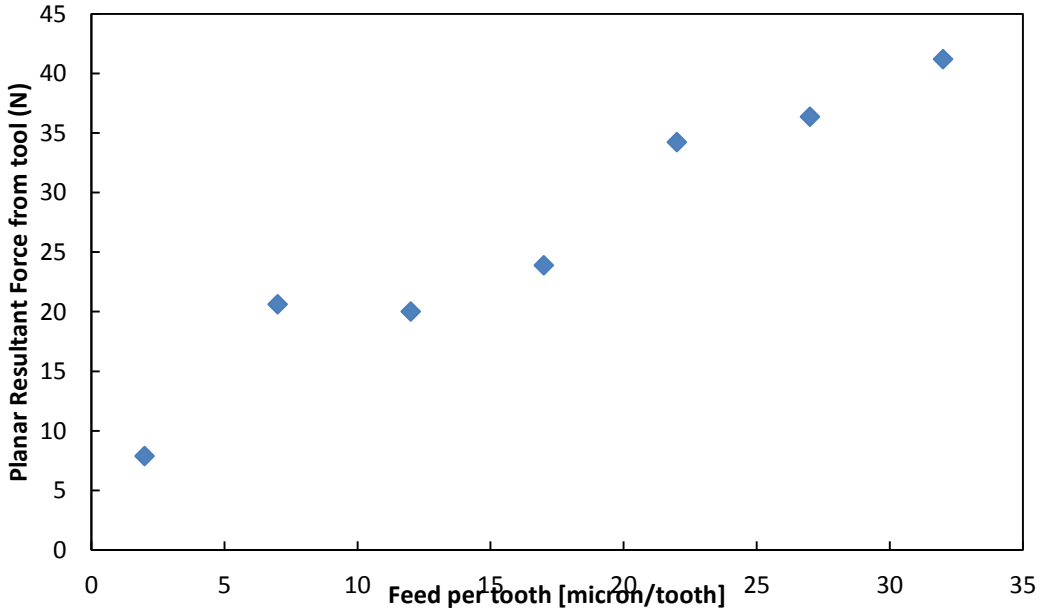

Figure 3.19 Double laminate average resultant cutting forces as a function of feed per tooth.

3.8 Analysis

The force data obtained from the refined study behaves as expected in that resultant cutting forces increase with increasing feed per tooth. The trend seems to be mostly linear however there is a significant deviation from this at the feed rate of 7 microns per tooth. This is likely a manifestation of the minimum chip thickness effect noted by Malekian et. al [43]. According to Equation (1) the cutting force should decrease linearly as the feed per tooth decreases. In micro-scale machining, at a certain feed per tooth, the tool tip can no longer be approximated by a perfectly sharp tip. Instead, it exhibits some radius known as the tool nose radius. When the uncut chip thickness reaches a value comparable to the nose radius of the tool, a plowing effect becomes more dominant in the cutting process. This effect is normally quite small in conventional macro-scale machining; however at very small feeds per tooth, the material is pushed and extruded as opposed to shearing. This plowing results in significant increases in cutting forces. The increase in force due to this plowing effect counteracts the decrease in force resulting from a decreased uncut chip thickness (removing less material). The minimum chip thickness is essentially the point at which these two effects are equal resulting in a local maximum of cutting forces. The data point at 7 microns per tooth agrees with this explanation. Figure 3.20 illustrates an analyzed form of the data with a curve fit to show the peak due to the minimum chip thickness effect. This curve corresponds very nicely with that observed by Mayor et. al [45] shown in Figure 3.21, although that study investigated thrust and cutting force individually as opposed to resultant force.

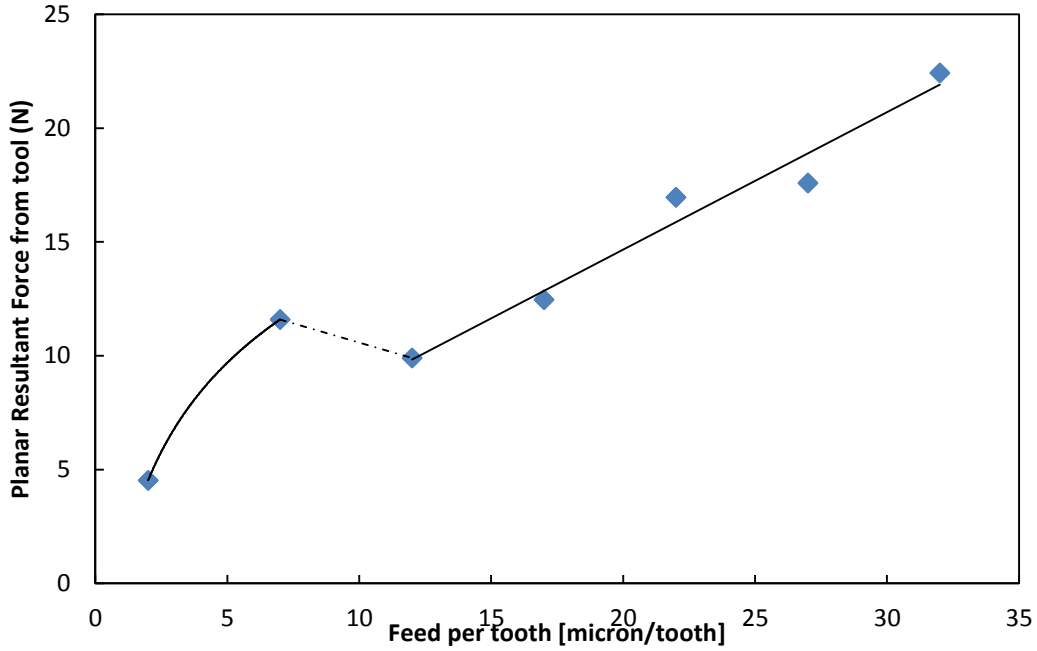

Figure 3.20 Average force values at varying feeds per tooth for single laminate machining experiments with fitted in a piecewise manner. A 2nd order polynomial fit is applied to the first two data points while the last five are fitted with a linear fit. The dotted line indicates a possible linear trend that may occur as the process transitions from a plowing dominant to a cutting dominant regime. However this region is not well characterized.

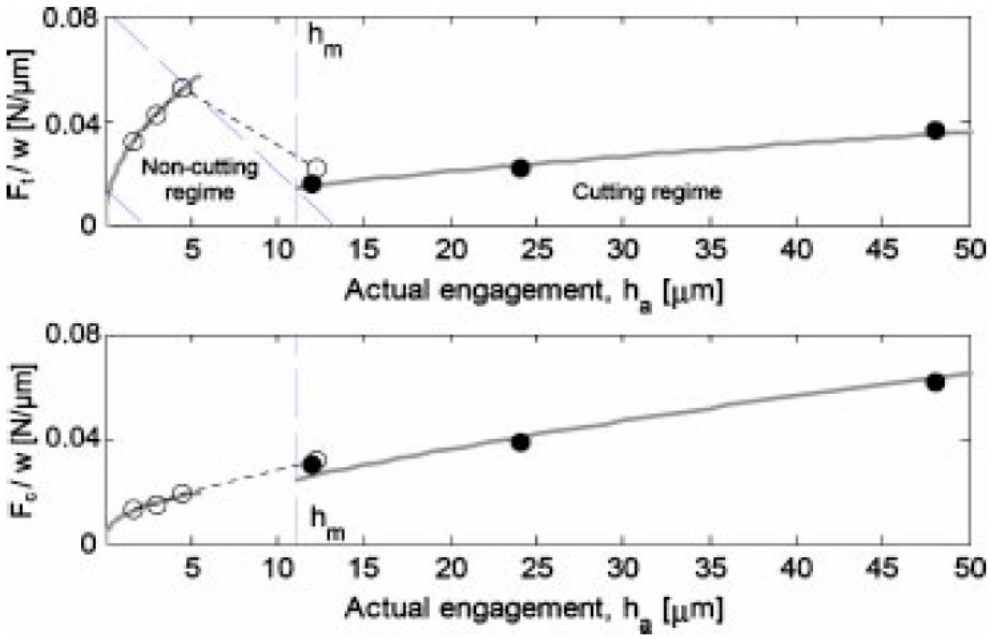

Figure 3.21 Micro-milling cutting forces vs. tool engagement (analogous to feed per tooth). Plots show the minimum chip thickness effect resulting in a peak in the cutting forces[45].

The specific cutting energy seems to follow the typical power curve of materials as can be seen in Figure 3.22. It can be described as a function of feed per tooth using Equation (3.14).

$$K_s = 3342.2 f_t^{-0.198} \tag{3.14}$$

In typical conventional macro-scale machining the specific cutting energy is assumed to be constant for a specific machining process. However, as evidenced by Figure 3.22, the value does indeed change quite significantly especially at very low feed per tooth. The value of the specific cutting energy varies with feed rate up to a certain point at which it is essentially constant. This constant region is the regime which most conventional macro-scale machining occurs. The evidence of this changing specific cutting energy also further confirms the occurrence of the minimum chip thickness effect. As the feed per tooth decreases, more energy is required to remove the material as the dominant cutting method transitions from shearing to plowing. This occurs due to the highly negative effective rake angle caused by the tool nose, exhibiting behavior very similar to a grinding process which also requires significant amounts of energy to remove small amount of material. A Kline-Mcclintock error analysis was conducted using Equation (3.15) based off the experimental uncertainty associated with the specific cutting energy values. In this Equation (m) is the number of teeth on the tool and (N) is the spindle speed. The uncertainty was calculated at the maximum undeformed chip thickness which should correlate with (F_{char}). It is important to note that only the uncertainty associated with the experimental process variables (force, feed rate, spindle speed, and axial depth of cut) was calculated.

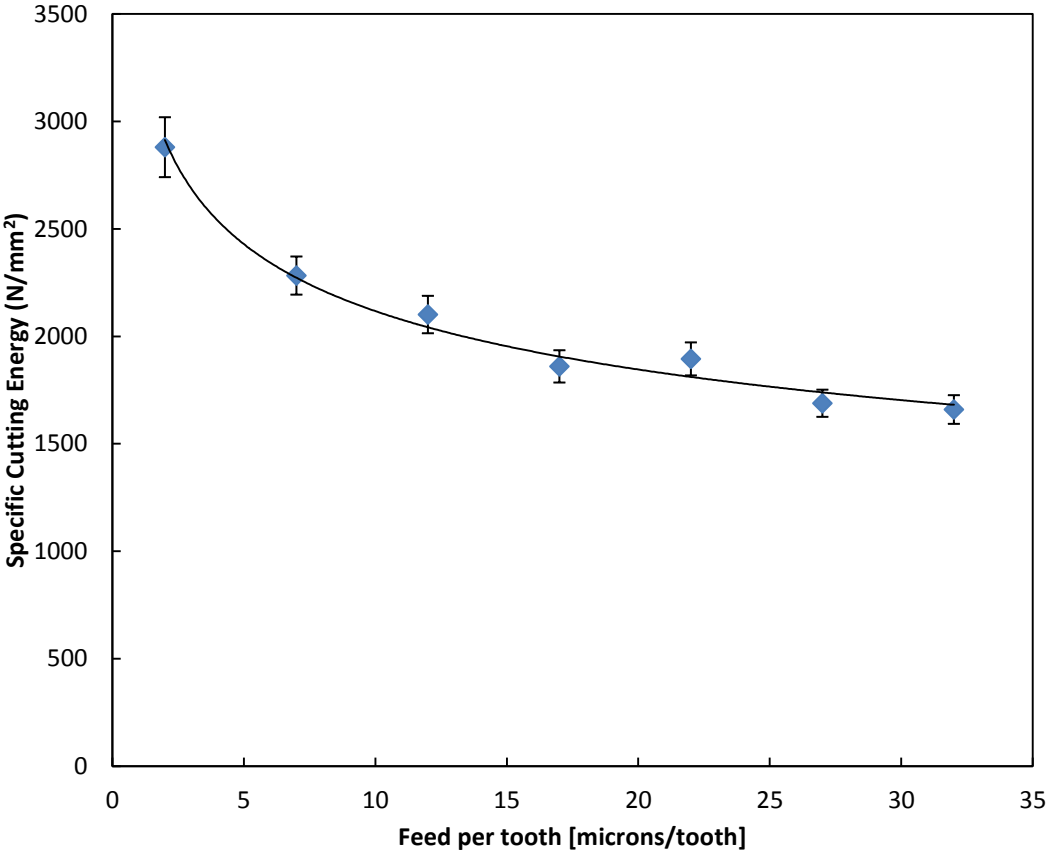

Figure 3.22 Average specific cutting energy values at varying feeds per tooth for single laminate machining experiments with a power law fitted trend line to illustrate material response. Note that error bars indicate experimental uncertainty.

$$K_s = \frac{F_{char}}{b\frac{f}{mN}\sin\left(\frac{\pi}{2}\right)\sqrt{1+K_r^2}} \tag{3.15}$$

The force ratios (Kr) for the tested conditions were also computed and are shown in Figure 3.23. It can be described as a function of feed per tooth using a piecewise function as shown in Equation (3.16) and Equation (3.17) with K_{r1} describing the first curve and K_{r2} describing the second curve.

$$K_{r1} = 1.0649 f_t^{-0.198} \tag{3.16}$$

$$K_{r2} = 0.1305 f_t^{0.4298} \tag{3.17}$$

The force ratio is the ratio of the normal force to the tangential force. As can be seen in the figure, the ratio is quite high at low feeds per tooth corresponding to a large amount of normal force. There is a sudden decrease in normal force around the minimum chip thickness. There is sizable experimental uncertainty which causes difficulty in determining the exact trends in the data. However, a piecewise power law fit is used to describe the trends of the data as power fits are commonly used to describe these trends [71]. The dotted line between the data points at 7 microns/tooth and 12 microns/tooth indicates a possible linear trend between these two points; however, the trend is only a postulation. The initially high force ratio can be explained as there is a significant amount of plowing at low feed rates which results in a high normal force. The normal force initially decreases with feed per tooth as the amount of plowing to shearing decreases as the feed per tooth approaches the minimum chip thickness. Furthermore, the sudden decrease in force ratio occurring around the minimum chip thickness is indicative of the cutting process transitioning from a plowing dominant to a shearing dominant regime, requiring less normal force. Finally, the force ratio begins to increase again as the feed per tooth increases at feed rates much higher than the minimum chip thickness. This is agrees with other observations by Kalpakjian at the rake angles considered in this study[63].

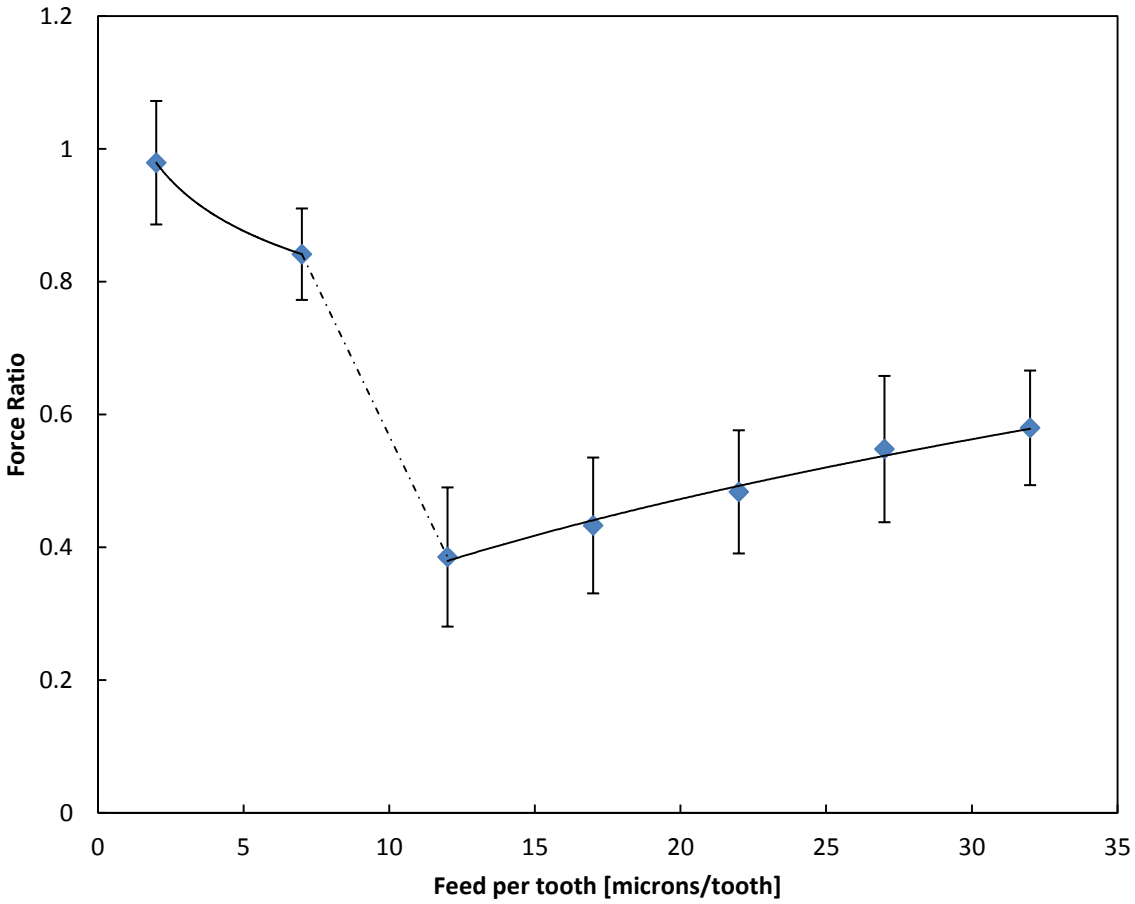

Figure 3.23 Average force ratio (Kr) values at varying feeds per tooth for single laminate machining experiments. A power fit is applied to the first two data points while the last five are fitted with a separate power fit. The dotted line indicates a possible linear trend that may occur as the process transitions from a plowing dominant to a cutting dominant regime. However, this region is not well characterized. Note that error bars indicate experimental uncertainty.

A Kline-Mcclintock error analysis was also conducted using Equation (3.18) based off the experimental uncertainty associated with the force ratio values. Again, the uncertainty was only determined for the experimental process variables.

$$K_r = \sqrt{\frac{F_{char}^{\ 2}}{b^2\left(\frac{f}{mN}\sin\left(\frac{\pi}{2}\right)\right)^2 K_s^{\ 2}} - 1} \tag{3.18}$$

Efforts to improve the experimental uncertainty were investigated; however, the variable parameters were either fixed by the manufacturer or prohibitively costly to implement. The thickness of a single laminate or laminated stack may vary by approximately 10 microns and is set by the manufacturer. The uncertainty of the spindle rotational speed is governed by the electric spindle controller and is conservatively estimated at 1000 rpm. The uncertainty of the drive system of the machine tool was estimated at 1% of the commanded feed rate. The force uncertainty is extremely low as the Kistler dyno possesses excellent force measurement capabilities; however, the uncertainty of this device was estimated at 0.1 N under the amplifier conditions used during testing. This uncertainty value was obtained by using precision weights to determine the accuracy of the dyno force measurement values at the testing conditions.

3.9 Discussion

Table 3.5 below shows the specific cutting energies and force ratios obtained using both the force averaging and empirical tuning approaches for a laminated stack over the entire range of feed rates investigated in both the coarse and the fine study. The force ratios are virtually identical as would be expected. Furthermore, the specific cutting energies differ by a constant of ~0.7 for all the feed conditions. This is due to the fact that the averaged force approach used the average force of the entire curve and the maximum uncut chip thickness to determine the specific cutting energy. If the average uncut chip thickness were used to determine the coefficient then the values should correspond

similarly to the way the force ratios do. It is important to note that other than this constant offset, the values and trends do agree well suggesting that the empirically tuned approach is capable of effectively handling cutter runout. Thus the empirical tuning approach is utilized to determine the machining coefficients during this study.

Table 3.5 Comparison of force averaged and empirically tuned specific cutting energy and force ratio

Feed per tooth [microns/tooth]	Spindle Speed [rpm]	Averaged Specific Cutting Energy [N/mm^2]	Averaged Force Ratio	Empirically Tuned Specific Cutting Energy [N/mm^2]	Empirically Tuned Force Ratio
2	80000	2949	0.78	4220	0.79
7	80000	1684	0.65	2481	0.68
12	80000	1251	0.49	1973	0.52
17	80000	1153	0.61	1651	0.67
22	80000	1252	0.62	1740	0.63
27	80000	1088	0.66	1538	0.6
32	80000	1058	0.68	1545	0.62

The cutting forces measured during this series of experimental trials are recorded and used to determine specific cutting energies and force ratios for their respective cutting conditions. The coarse–fine approach of this study enables the observation of a possible strain rate dependence of the material as specific cutting energy and cutting force clearly decrease with increasing strain rate as shown in Figure 3.24.

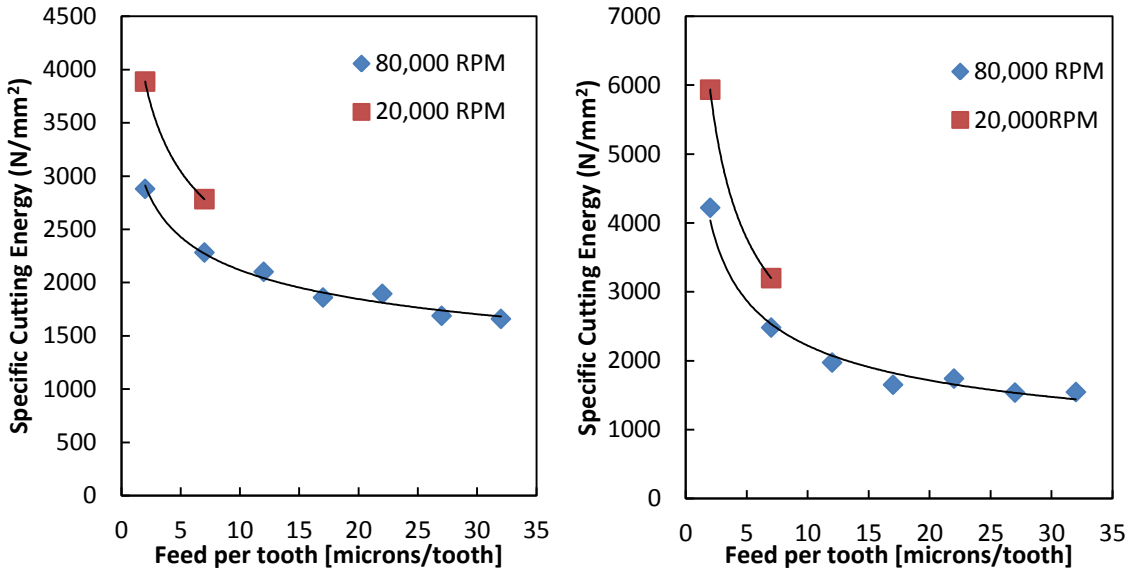

Figure 3.24 Specific cutting energy vs. feed per tooth at multiple cutting speeds. (Left) single laminate. (Right) Two laminate stack.

A potential explanation of this is the change in shear plane length that typically occurs at increasing cutting speed. As the cutting speed increases, the temperature in the chip tool contact area increases and thus the friction decreases. This generally leads to an increase in the shear-plane angle which means that a shorter shear plane length. Thus for a given shear stress of the material a decrease in cutting force must occur. Consequently, increasing the spindle speed results in a decreased resultant cutting force as well as a decreased specific cutting energy which agrees with our recorded data.

However, this process could also be described by the concept of thermal softening. The temperature rise that occurs in the shear plane and along the tool chip interface could result in a decrease in the local yield strength of the material. As the spindle speed increases, the temperature rise will also increase due to the fact that there is less time for the heat to be dissipated at increased cutting speeds. The reduced yield strength will manifest as a decrease in cutting force and a consequent decrease in the specific cutting energy. Thus the specific cutting energy and resultant cutting force decreasing with

increasing spindle speed could also be explained via thermal softening. It is important to note that addition phenomena could be occurring during this cutting process such as changing built up edge or friction angle; however, these were not specifically investigated in this study. Further, detailed study is necessary to draw definitive conclusions as the exact cause of these effects.

The feed rates investigated ranged from 2 microns per tooth correlating to 5.3mm/sec (11.8ipm) to 32 microns per tooth corresponding to 85mm/sec (200ipm).The upper end of this range includes quite aggressive feed rates which makes this process quite favorable from a productivity vantage point. Furthermore, the relatively low cutting forces, seem to suggest that even greater feed rates can be obtained (even though the limits of our machining test center were unable to investigate these higher feed rates to find an absolute maximum feed per tooth. It is predicted that, given the response of the material over the investigated range, machining limits of the machine tool (via tool failure or spindle stalling) are likely to be factors limiting the maximum productivity of this process. The cutting forces for single versus double laminated stacks are shown in Table 3.6 .

Table 3.6 Resultant force ratio for single layer stack vs. double layered stacks

Feed per tooth [microns/tooth]	Spindle Speed [rpm]	Force (single laminate) [N]	Force (2 laminates) [N]	Proportional percentage difference
2	80000	4.52	7.89	7.3%
7	80000	11.59	20.63	6.2%
12	80000	9.9	20.02	0.6%
17	80000	12.46	23.91	2.1%
22	80000	16.96	34.25	0.5%
27	80000	17.59	36.38	1.7%
32	80000	22.42	41.21	4.4%

The percentage difference is calculated by doubling the amount of force required for one laminate and comparing this value to the value recorded for a two laminate stack. There is less than an 8% difference between the expected force value and the measured force value. This amount of difference actually falls within the experimental variation encountered at the testing conditions. For example, the resultant cutting forces measured at a specific condition varied amongst the different replicates by as much as a couple of newtons (whereas all the percentages correspond to differences of less than 2N). This indicates that a slight difference may exist; however, the data cannot prove this with certainty. This indicates that the thin layer of resin actually is capable of constraining the laminated stack and causing it to behave as a homogenous material from a forcing mechanics perspective. This agrees with our initial assumption and also suggests that the thin layer of epoxy does not significantly contribute to the force required to cut the stack while simultaneously providing sufficient interlaminar rigidity to enable multiple laminates to be processed at the same time.

3.10 Summary

This work has presented an initial investigation into though-cut slot milling of laminated stacks of electrical steels. This process is a potential candidate for the rapid prototyping and successive optimization of electrical machines. High material removal rates can be achieved. The specific cutting energy of M-19 in HTPM was determined over a wide range of cutting conditions. Higher cutting speeds and feeds per tooth also correspond with a decrease in specific cutting energy. These specific cutting energies can be incorporated into the force predicting model to accurately predict the cutting forces of

this material at the ideal process conditions (from a process efficiency standpoint) attainable by current available machine tools.

CHAPTER 4

OPTIMIZATION OF CUTTING PARAMETERS FOR MAXIMUM PRODUCTIVITY AND MINIMUM BURR FORMATION

4.1 Introduction

This chapter addresses the investigation of the optimal cutting parameters in the high-throughput profile milling process to achieve maximum productivity while maintaining acceptable part quality. Specifically, an effort to obtain an understanding of the factors influencing burr formation along the edge of the cut is conducted. This investigation, performed concurrently with the analysis of the specific cutting energy and cutting forces produced during the HTPM experiments, will serve as the primary characterization metric of the cut quality. Some investigation and discussion of delamination of the laminated stacks is also conducted. Insight obtained from this study will serve to help determine an optimal condition to process and shape electrical steel laminates via milling.

4.1.1 Material Properties of M-19 Electrical Steel

The material properties of M-19 electric steel, particularly its high toughness, will ultimately have a significant impact on the optimization of the cutting parameters. The chemical composition of the alloying metals used in conjunction with iron to produce M-19 electrical steel is shown in Table 4.1. It is important to note the relatively high percentage of silicon alloyed in the steel.

Table 4.1 Chemical composition of M-19 electrical steel used in this study[72]

Composition %

C	Mn	P	S	Si
0.003	0.15	0.01	0.001	2.7

It is also important to note, that the material properties utilized in this study are limited by the supplier's manufacturing and business practices. The different grades of electrical steel are rated based on thickness, core loss and magnetic permeability. Per the manufacturer's production standards, the grades: M-15, M-19 and M-22 are produced from the same batch of alloyed metal. The differing grades are all processed as if they were to be M-15 receiving the same chemical alloys and undergoing the same processing. The achievable tolerances in the alloying composition and processing techniques result in variations in core loss and permeability. There will always be some variability in the other magnetic properties, such as resistivity, hysteresis etc, within the same grade and across grades. There will also be some variation in mechanical properties. Consequently the manufacturer rates the material properties and provides typical values, guaranteeing core loss only. Depending on the availability of various grades, higher quality grades will be provided to the customer if the requested grade is unavailable (e.g. if M-22 is requested and the current inventory only contains M-15, M-15, the better grade of magnetic material, will be provided). Consequently the material properties used in this research will be based off of the M-15 grade, except for the core loss which is specifically provided for M-19. All mechanical properties available from the manufacturer are shown in Table 4.2.

Table 4.2: M-19 Material Properties.

M-19 material properties	values	units
Laminate thickness:	0.014	in
Electrical Steel Standard Gauge Number (ESSG No.)	29	
Density	7.65	gm/cm^3
Yield strength	358	MPa
Tensile strength	490	MPa
Elongation % in 2in strip	23	%
Rockwell B hardness	72	HRB

The yield strength and hardness of the M-19 steel is comparable to that of typical steels. However, it exhibits a very large elongation percentage. This large strain actually results in the material becoming significantly tougher than typical mild steel. This relatively high toughness results in a low machinability, indicating that it will be quite challenging to machine this material and that proper process parameters must be selected to effectively cut the material to produce acceptable parts. Figure 4.1 shows an approximated true stress-true strain curve comparing lower bound estimates of toughness between M-19 and other common steel types.

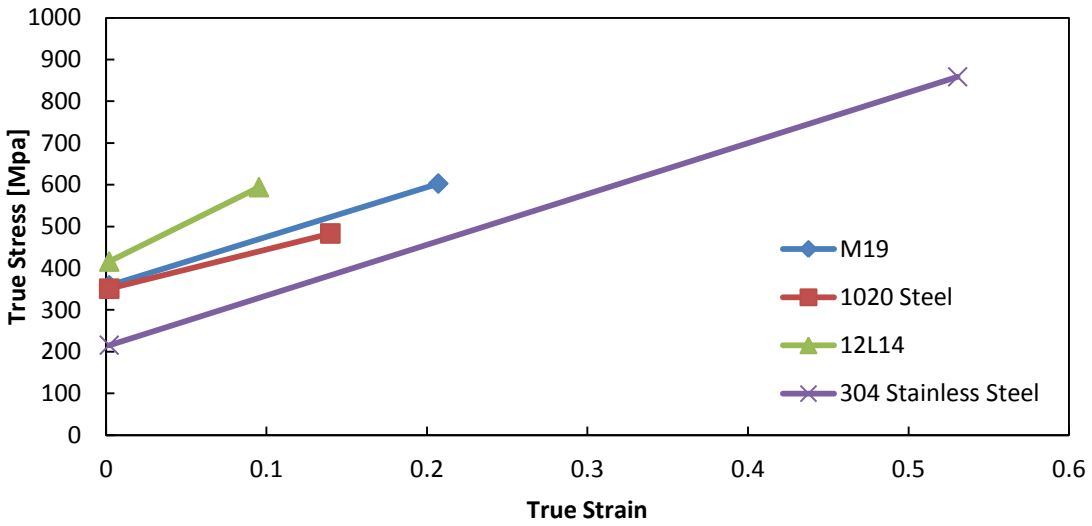

Figure 4.1 Approximated stress strain curves for various types of steels

Due to the limited mechanical material properties available, this plot was constructed incorporating several key assumptions. The materials are assumed to be elastic-strain hardening and the values provided by the manufacturer are converted to true stress and true strain. The point of intersection of each curve at the ordinate is the yield strength of the material (thus the elastic regions are not shown). The yield stress is assumed to be taken at 0.2% elongation as is common practice in material mechanics tests. The ultimate tensile test is used as a conservative estimate of fracture (although fracture actually occurs later) and by correlating it with the maximum elongation percentage of the materials, a linearized approximation of the stress-strain curve is developed. The area under this linearized curve is then calculated to produce a toughness value for each material. As illustrated in Figure 4.2, the toughness of M-19 is approximately twice that of 1020 steel which well known as a difficult material to machine. Thus burr formation is expected to be a significant factor in the process optimization.

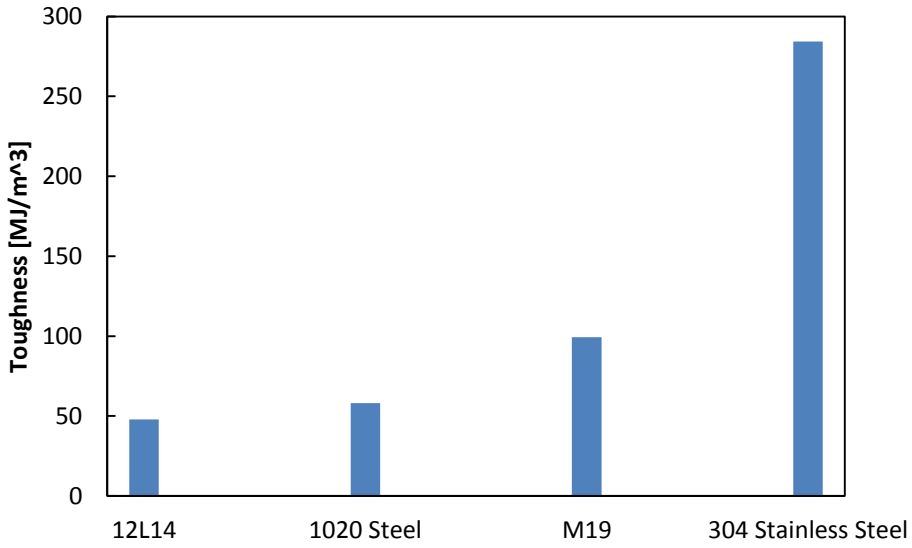

Figure 4.2 Comparison of toughness of various types of steel

4.1.2 Burr formation metric

The electrical steel under investigation, similar to many steels is a very tough and ductile material. Thus significant plastic deformation occurs in the material during the machining process as the feed per tooth decreases (which occurs along the entry and exit of a milled full slotting cut). This manifests as ductile extrusion of the chip instead of the desired clean shearing failure. Consequently, the extruded chips remain adhered to the base material in the form of burrs. Thus due to the ductility and toughness of the electrical steel sizable burr formation can be expected.

This burr formation is specifically selected as a dominant governing metric for part quality due to its significant and multiple effects on the manufacturing and performance of electric machines. Burring along the edge of laminates can result in assembly difficulty due to the fact that several laminates are required to assemble an electric machine. Burrs can get caught between laminates resulting in dimensional and positioning errors. Furthermore, the burring can result in electromagnetic shorting of the electrical steel, providing an alternate path for the magnetic flux to flow causing degradation in the machines performance [40]. Significant burring can also present problems with winding the copper coils around the machines. Burrs present a rough and jagged surface which can erode some of the coating on the outside of the copper coils and potentially resulting in electrical short circuiting. This can cause decreased machine performance and potentially dangerous heating of the coils, which could ultimate result in catastrophic failure of the electric machine. Finally, bur removal which is necessary to avoid this negative consequences is a costly and time consuming secondary process[73]. Consequently, burr formation presents a critical process defect that must be mitigated for

satisfactory production and performance of these electric machines. Furthermore, burr formation is expected from the machining of this electrical steel due to its high toughness and percentage elongation.

4.1.3 Delamination metric

Delamination is considered due to the novel concept of processing multiple laminates simultaneously via milling. Productivity can be drastically increased using this approach as opposed to more conventional serial production of laminate components and subsequent stacking of these layers. Delamination should also be mitigated in order to maintain acceptable part fixturing during the cutting process. Separation of the laminates could cause undesirable vibration, unexpected tool interactions, and ultimately unusable components due to improperly machined surfaces.

4.2 Approach

The same design of experiments utilized to investigate the cutting forces and specific cutting energy was also used to study burr formation and delamination. Similarly, a two step, coarse-fine experimental plan enables a broad investigation of overall trends followed by a more refined analysis conducted over a specific range of interest. The first coarse study consisted of a three factor, two level experimental test matrix investigating the feed per tooth, axial depth of cut (more specifically single layer and two layer laminated stacks), and spindle speed. The peak burr height and the percentage of the cut that is burred were recorded to describe the burring along the edge of the cut. It is in fact quite difficult to accurately measure burr geometry on the micro-scale. The orientation of the burr can have a significant effect on a burr height measurement, as a burr of constant geometry can have a different measured height depending on whether it is "standing-up"

perpendicular to the surface or "laying down" against the surface. In addition to the challenge introduced by the orientation of the burrs, it is possible for a surface to have a single very large burr left over at the end of a cut while most of the cut is burr free. Furthermore, it is also to have a cut edge that is completely burred along its length with very short burrs. If these two cases are describe by their height alone, a large amount of descriptive information is left unreported. Thus it was deemed necessary by the authors to consider more than simply one metric to describe the burring due to the intermittent and extremely variable formation of the burrs.

In the subsequent fine study, burr height was quite small and it became difficult to optically measure the burrs with the digital microscope and maintain confidence in the results. Thus a surface profilometer was utilized instead to characterize the burr heights. Similar to the force and specific cutting energy fine study, this study consisted of a single factor, five level experimental test matrix, further analyzing the influence of feed per tooth on burr formation while cutting at maximum spindle speed. The peak burr height and also the average burr height were reported due to the added capability of the surface profilometer to quickly measure the entire range of the cut.

4.3 Apparatus and Experimental Setup

In the coarse study, subsequent to machining of the laminated stacks, the samples are examined using a Keyence VHX-600 digital microscope. Lingering chips were removed from the surface of the laminates with a soft bristled brush before viewing under the microscope. This brush was selected in order to remove chips that had simply adhered to the surface, and to simultaneously avoid damaging or deforming the burrs. The digital microscope incorporates image processing capabilities that enable it to perform non-

contact profilometric measurements of surfaces. This is accomplished by recording numerous images over a range of incremented, recorded focal distances and then compiling the images together to generate a three-dimensional profile of the surface. This microscope is used to take high quality images of the cuts in addition to determining the surface profile of the burrs left over by the machining process.

Figure 4.3 shows a screen image from the digital microscope. It incorporates the digitally processed image and uses the previously processed data to produce a profile of the surface shown below the image. The profile describes the height measured along the red line shown in the image. The green lines overlaying the profile are utilized to measure the height of the burr relative to the laminate surface. The image is a picture of a milled slot in one of the electrical steel samples. The burred edges are clearly visible near the top and bottom of the image. It is important to note that the blurry section in the middle of the image is simply the table of the microscope beneath the laminate.

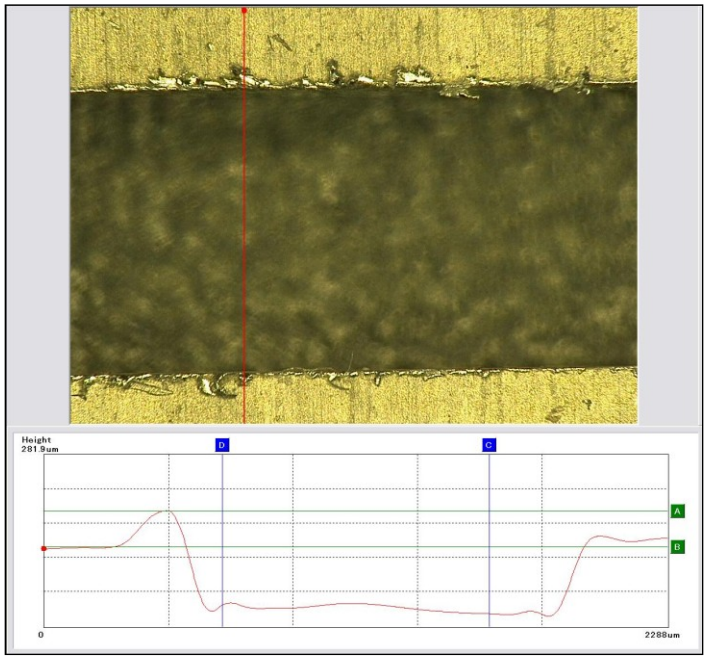

Figure 4.3 Image obtained via digital microscope illustrating a high throughput profile milled machined slot and the surface profile of this slight taken along the red vertical line.

The quality of the cut is evaluated optically by the digital microscope. A magnification of 20X was selected as a standard to compare the overall quality of the cut. The burring percentage was measured at this magnification. A higher magnification of 100X was used to evaluate the actual burr height.

After conducting the coarse study, it was determined that the fine study would measure much smaller burrs due to the effects of the process parameters being studied. Consequently, a different approach is used to evaluate the burr characteristics of the cut. Instead of the digital microscope, a stylus profilometer (Talysurf 112, Taylor Hobson) with a sapphire sphere stylus (0.774mm in diameter) is used to measure the profile along the edge of the cuts. This instrument has the added benefit of recording the entire profile of the burred surface, thus providing a very detailed description of the burred edge (in essence simultaneously measuring burr height and the percentage of the cut that is burred). The large size of the stylus allows it to pick the highest points of the burrs providing a very conservative estimate for burr height. The laminate is carefully fixtured using an adhesive to a stage located on the Talysurf and the stylus is aligned such that it traverses collinearly with the cut edge. A trace is taken measuring the burr height over a length of approximately 15 mm. A portion of the flat, un-machined surface of the laminate is also measured during the same trace to provide a datum surface from which the burr height can be determined.

4.4 Results

4.4.1 Coarse study (Initial Investigation)

The data collected for the coarse study consisted of optical measurements of the laminated stacks. The average peak burr height and average burring percentage for each of the three replicates tested at a condition tested are concisely shown in Figure 4.4 and Figure 4.5 respectively. These figures can be interpreted similarly to the initial coarse investigation that was conducted in the previous chapter. The first four cases incorporate a two laminate stack axial depth of cut while the last four incorporate an axial depth of cut equal to the thickness of a single laminate. The even cases correspond to the high spindle speed of 80,000 rpm while the odd numbered cases correspond to 20,000 rpm. Finally, the square data points indicates low feeds per tooth of 2 microns/tooth and the circle data points indicate high feeds per tooth of 7 microns/tooth. It is important to note that the data of this initial coarse study it utilized to determine trends in burr formation and not necessarily explicitly describe exact burr geometrical data. As evidenced by the large standard deviations, drawing decisive conclusions concerning the exact burr heights under the investigated conditions is quite difficult. However general trends can be determined in this phase of the study, enabling subsequent, more refined investigation of the actual burr heights in the fine study.

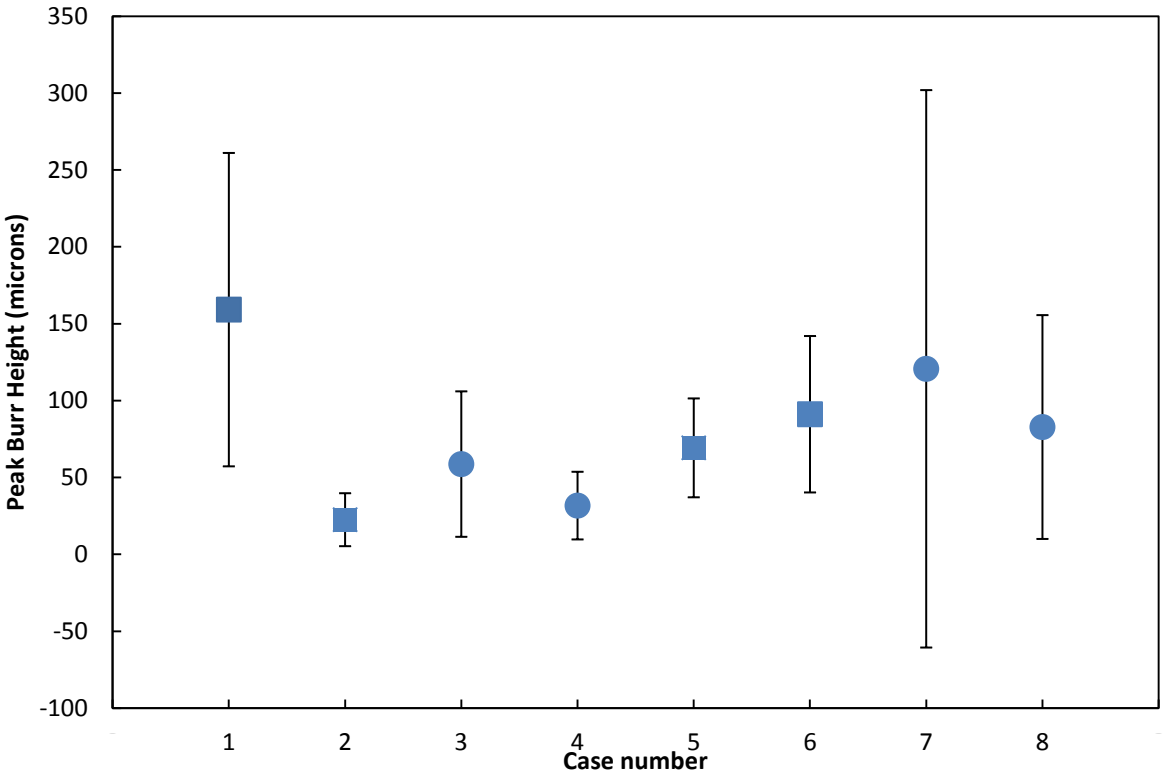

Figure 4.4 Peak burr height for the eight conditions under investigation. Displayed values are the average of 3 replicates with the standard deviation above and below these values.

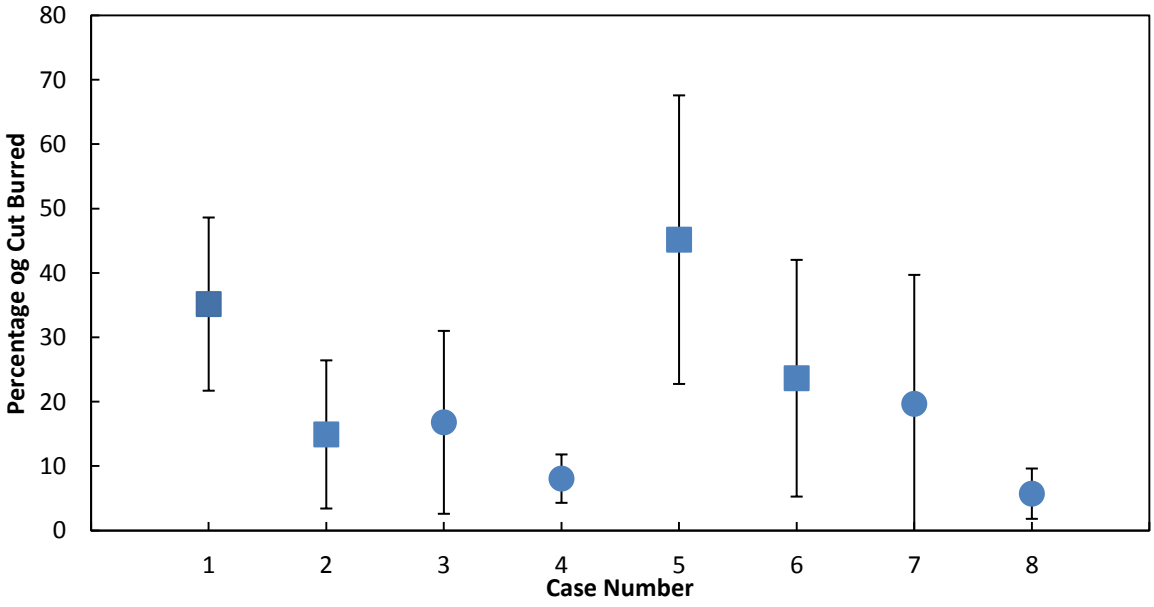

Figure 4.5 Burring percentage for the eight conditions under investigation. Displayed values are the average of 3 replicates with a standard deviation above and below these values.

Some of the conditions in Figure 4.5 also displayed very large standard deviation. This is again likely due to the intermittent nature of burr formation and the difficulty of effectively identifying and measuring the burrs. It is important to note, that the large standard deviation of Case 7 shown in Figure 4.4 was caused by a very large peak burr height outlier, offsetting the average of the other significantly smaller peak burr heights cut at the same condition. Both Figure 4.4 and Figure 4.5 display similar trends with decreased peak burr height at higher spindle speed and feed per tooth. On several of the cuts intermittent burring was observed with various sized burr-free regions located between burrs. However, some cuts, as can be seen in Figure 4.6 exhibited consistent burring throughout the length of the cut. Furthermore, for certain cases, burring occurred much more on one side of the cut than another side. However, this did not seem to occur consistently along the cut or for the replicates at any specific cutting condition.

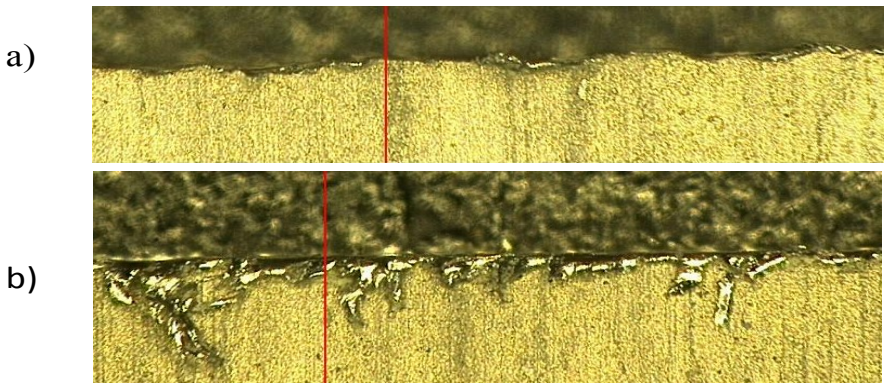

Figure 4.6 (LEFT) Comparison of cut quality. (a) Edge of cut made using Case 4 (80,000rpm, 7 micron feed per tooth, two laminate stack) with very little burring. (b) Edge of cut made using Case 5 (20,000rpm, 2 micron feed per tooth, single laminate stack) with significant burring

Delamination was determined optically and results show that delamination free machining can be achieved during this cutting process. Only one of the replicates (the first replicate of Case 1) of all the tests showed slight delamination near the end of the

cut. Figure 4.7 displays the sidewalls and delamination of this cut and of a cut exhibiting no delamination (Case 3). Very clean sidewalls were observed along the edge of most of the cuts in the study, clearly displaying the very small thickness of the epoxy layer and the lack of delamination during the cut.

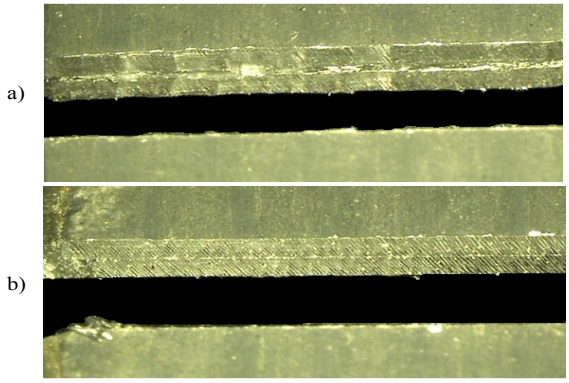

Figure 4.7 Sidewalls of cut laminated stack. (a) Slight delamination is observable (cut from Case 1 at 20,000rpm, 2 micron feed per tooth, and two laminate stack). (b) No delamination is observable (cut from Case 3 at 20,000rpm, 7 micron feed per tooth, two laminate stack). Note: black region is surface of microscope table. It has been digitally modified to enable easier viewing of the image.

4.4.2 Analysis (Coarse Study)

The data obtained from the digital microscope images was further analyzed to yield a quantified description of the burr formation. The peak burr height measurement required tedious and time consuming metrology of the samples. The profilometric measurement of the microscope takes numerous high resolution images and requires some time to acquire and compile all this data. Furthermore, high magnification is required to obtain precise measurements of the burr heights. This decreases the viewable area within the image. Consequently, the images are visually inspected at a lower resolution to determine the largest burrs and then the regions of interest are magnified and profiled. Thus the maximum peak burr height for a given condition is determined. In order to determine the percentage of the cut that is burred, individual burrs geometries were each manually

measured using one of the microscopes image processing tools. The pixel length of the burrs can then be converted to correct physical lengths using the appropriate scaling factor for the microscope's viewing resolution. The lengths of these burrs are then compared with the overall length of the cut and thus a percentage ratio of the burred to unburred portion of the cut can be determined.

4.4.3 Results (Fine Study)

The data collected for the fine study consisted of Talysurf profile measurement of the cut edges of the laminates. The average peak burr heights for the three replicates tested at each condition are displayed in Figure 4.8 Furthermore, the average burr height along a specific cut sample (referred to as the mean burr height to avoid confusion) was determined from the surface profile data for each individual experiment. These mean burr heights were then averaged across the replicates of a given condition shown in Figure 4.9.

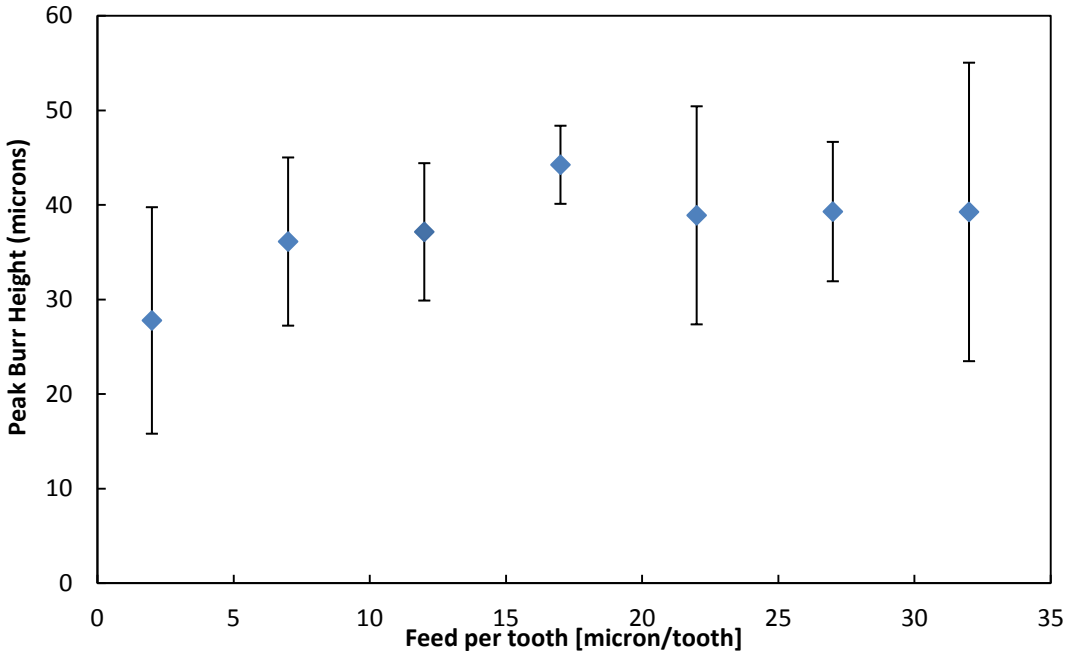

Figure 4.8 Maximum peak burr height as a function of feed per tooth. Error bars indicate standard deviation.

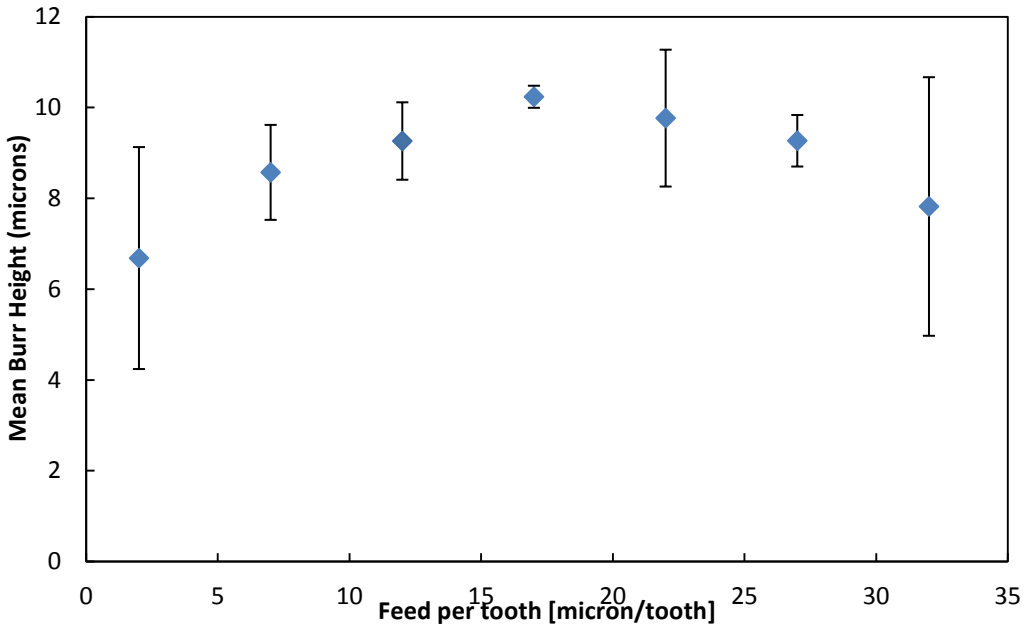

Figure 4.9 Mean burr height as a function of feed per tooth. Error bars indicate standard deviation.

Significant standard deviations can be observed in the figures of maximum peak burr height and mean burr height. This is again due to the highly variable and intermittent nature of mechanically produced burrs. It is noteworthy that the standard deviations in the mean burr heights are only on the order of microns; however, the average values are so low that the error bars depicting the standard deviation appear quite large.

4.5 Analysis

The surface profile obtained using the Talysurf is processed via filtering software that accompanies the instrument. The initial profile is retained in addition to separating it into roughness and waviness components. The roughness profile removes any gradual surface waviness that may be occurring in the sample. The waviness profile removes the high frequency variations that occur due to the surface roughness of the sample. For this study the roughness data was utilized due to its removal of any height variations that may have been due to the lack of flatness present in the thin laminate material. This should yield the

best representation of the actual burr profile. An image of a characteristic surface roughness profile obtained from the Talysurf is shown in Figure 4.10. The figure illustrates some of the additional data analysis that is conducted to be able to draw meaningful information from the data. The relatively flat region occurring after 15mm is the actual surface of the laminate, and the small variations in this region are due to the actual surface roughness of the electrical steel sample. The data values that occur before this 15 mm point reflect data from the actual burred region. Points that occur below the middle dashed line are actually representations of the profilometer stylus dropping below the surface of the laminate and detecting variations along the sidewall edge of the cut laminate. Data points below this line are not meaningful with regards to determining the burr height. Thus data points from the flat profile of the laminate surface are averaged and set as a datum for burr height comparison. The data points occurring below this data are simply neglected and the difference between the datum and the remaining burr peaks of the burred region are calculated to obtain burr peak heights. From these peaks a maximum peak height can be determined (as illustrated in the figure). Furthermore, an average burr height can be computed from the peaks. This average inherently incorporates both percentage of the cut burred in addition to maximum burr height to provide a more complete description of the surface cut quality.

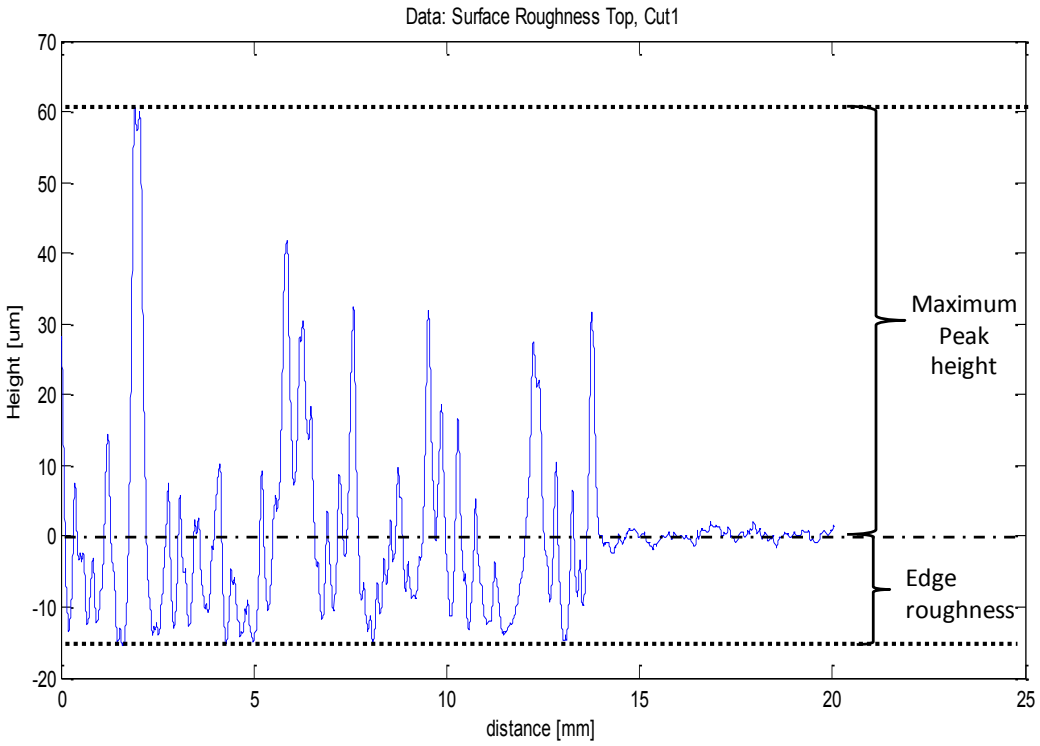

Figure 4.10 Characteristic Surface roughness profile taken from a trace along the edge of a machined slot.

It is important to note the surface roughness of the laminate material is approximately 3 microns as can be seen in Figure 4.10. This is useful when making comparisons of small burr heights and their effects on part quality. Burr heights near or smaller than this value are likely negligible due to the fact that the profile measurement could indeed be due to the inherent surface roughness of the material as opposed to actual burr formation.

4.6 Discussion

4.6.1 Burr Formation

It was noted that at smaller feed per tooth, greater burr formation occurred. Significantly larger maximum burr height and percentage of the cut that is burred was observed on the lower feed rate trials of the initial coarse investigation. A potential

explanation for this can be the existence of a minimum chip thickness at which the machining process transitioned from a cutting dominant regime to one dominated by plowing of the material. This plowing process in conjunction with the high spindle speed can result in heating of the material, and significant burr formation. The material's relatively large maximum elongation percentage is clearly manifested here as it forms very large, consistent burrs along the cut edge of the workpiece. The increasing specific cutting energy required at lower feed rates noted in the previous chapter also agrees with this explanation. More energy is required during these small feed per tooth cuts due to the plowing dominant actions of the tool, which is much more energy intensive than shearing the material. Thus undesirable burr formation can occur at small feeds per tooth. Furthermore, the trends in burr formation seem to follow the same trends as the specific cutting energy required to process the material. Analysis of these experiments suggests that cutting the material in a shearing dominant regime with uncut chip thicknesses larger than the minimum chip thicknesses should result in reduced burr formation.

As illustrated in Figure 4.5, increasing the spindle speed does serves to decrease the burr formation. It has been noted in previous studies that ductility decreases with increasing strain rate. [61, 63, 74] This is generally accepted and corresponds with our data as less burring occurs at higher cutting speeds. These results agree with the findings of previous studies which investigate burr formation in the machining of other materials [55, 73, 75, 76]. Thus the subsequent fine study further investigated burr formation at these conditions. Very small maximum peak burr heights were observed from these tests. The largest average peak burr height was 44 microns corresponding to 12% of the thickness of a single laminate. Furthermore, the largest average mean burr height was 10

microns corresponding to 2.8% of the thickness of a single laminate. This is only slightly above the surface roughness of the uncut laminate. Finally, cutting at extremely aggressive feed rates of 85mm/sec (200 ipm) the mean burr height could be confined to a value of 8 micron. There is still a significant amount of variation in the averages determined from the replicates; however, the mean values are relatively low in comparison to the thickness of an individual laminate. Thus cutting at these high speeds and feed rates should effectively minimize burr formation to an acceptable level for producing laminated stacks.

4.6.2 Delamination

The two possible types of delamination (in plane shearing and out of plane "alligatoring") as shown in Figure 4.11 were investigated during this study. In all of the experimental studies except for one, no delamination was observed. Furthermore, no in plane shear delamination was observed in any of the trials.

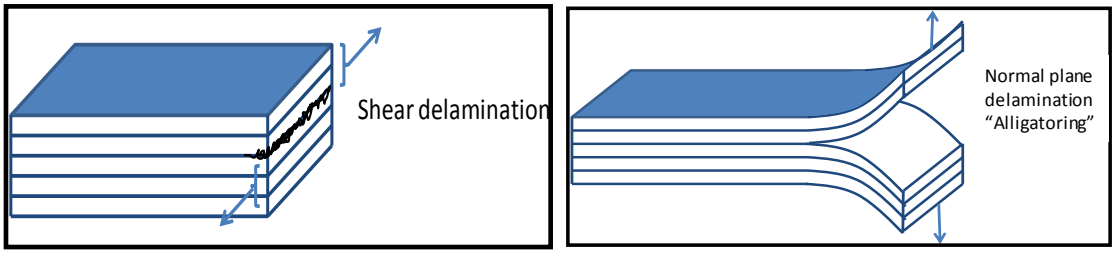

Figure 4.11 Illustrations of modes of delamination in a laminated stack

Figure 4.12 below shows the sidewalls of one of the cuts conducted at the higher feed rates and spindle speeds of the coarse study (7 microns per tooth). The single delamination incident may have been due to poor epoxy bonding near the edge of the sample. The delamination only occurred at the unconstrained end of the sample as can be seen in Figure 4.13. Once a crack is created, it can propagate (due to the brittle nature of

the resin) by the continued forcing and vibration of the machining process, and due to chips being wedged between the laminated layers. However, resins with greater peel strengths should be more resistant to continuing this propagation. Thus the forcing was likely not significant enough to sufficiently propagate the crack to the base of the cut as no delamination is observed there. This suggests that although initial delamination may occur, the bonding of the stacks with an epoxy resin is a relatively robust means of maintaining and producing laminated stacks.

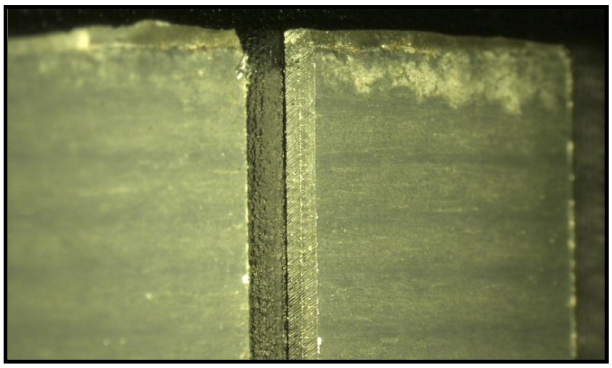

Figure 4.12 Machined slot within a laminated stacks exhibiting no delamination. (A) Left side of slot. (B) Right side of slot

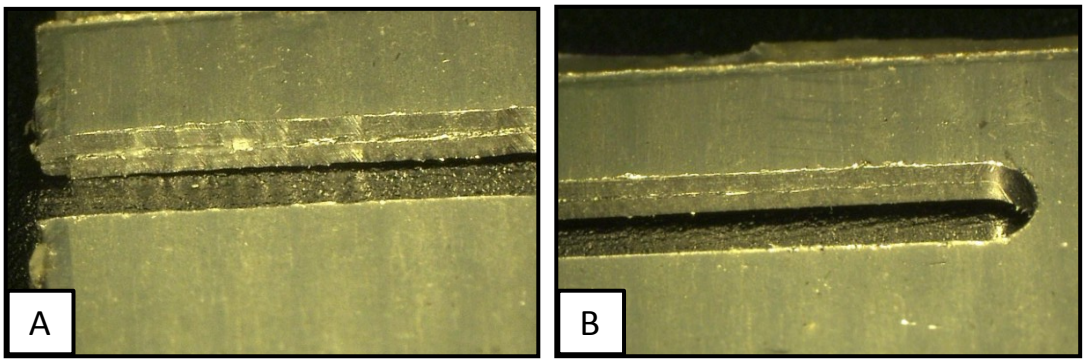

Figure 4.13 Machined slot within a laminated stack exhibiting slight delamination near the outer edge (A) but not delamination near the base of the same slot(B).

Previous initial machining of laminated materials has indicated that the likelihood and amount of delamination increases with axial force applied to the stacks[77, 78]. This is

supported by the delamination of the initial cuts of the laminated stacks from blind cuts (which introduces significant axial forces on the floor of the cut) and from the out of plane alligatoring of the stacks serving as the primary mode of delamination. Due to the low helix angle utilized in this study, very small axial forces were produced in the coarse and fine investigations. Thus, it seems that delamination can be altogether avoided by machining under proper conditions, namely minimizing the axial forces applied to the stack below a certain critical delamination force (the force necessary to generate a crack).

4.7 Supplementary Study on Tool Wear

Subsequent to the previous experimentation and analysis, an additional exploratory study was conducted to investigate the impact of tool wear on the burr formation during the cutting process. It was initially assumed that due to the short cutting length of the tests (a total of 360mm for a given study) that tool wear would be insignificant and consequently not a noteworthy factor in the study. This additional study was conducted to verify this assumption. The study was conducted on a single laminate at a constant spindle speed of 80,000rpm, and two feed rates: 7 microns per tooth and 32 microns per tooth. A new tool was used to machine several slots into a sheet of the electrical steel for a total cutting length of 1500 mm. This is accomplished by cutting 15 slots each 100 mm in length. This cutting length corresponds to a cutting length 4 times greater than experienced by a tool in the previous experimental studies. Three replicates were conducted at each feed rate. The burr formation was then investigated along the length of the cut by measuring the burred edge along a slot using the Talysurf profilometer. A trace is taken along the length of a slot at regular intervals of the total length of cut for a given tool. For example the data point shown in Figure 4.14 at 800mm corresponds to a trace

taken along the 8th slot of a replicate. Figure 4.14 and Figure 4.15 display the mean burr height measured as a function of length of cut. Figure 4.14 presents experiments specifically conducted at a 32 micron per tooth chip load which corresponds to a feed rate of 85.3 mm/sec, the highest feed rate investigated in this study. Figure 4.15 refers to experiments conducted at 7 microns per tooth chip load corresponding to a low feed rate of 18.6 mm/sec. There appears to be a slight increasing trend (on the order of microns) in burr height; however, the change in burr height from the beginning to the end of the cut falls within the variation observed in the previous experimental studies. Thus it can be concluded tool wear was not a significant factor in the measured burr formation of the tests in this study.

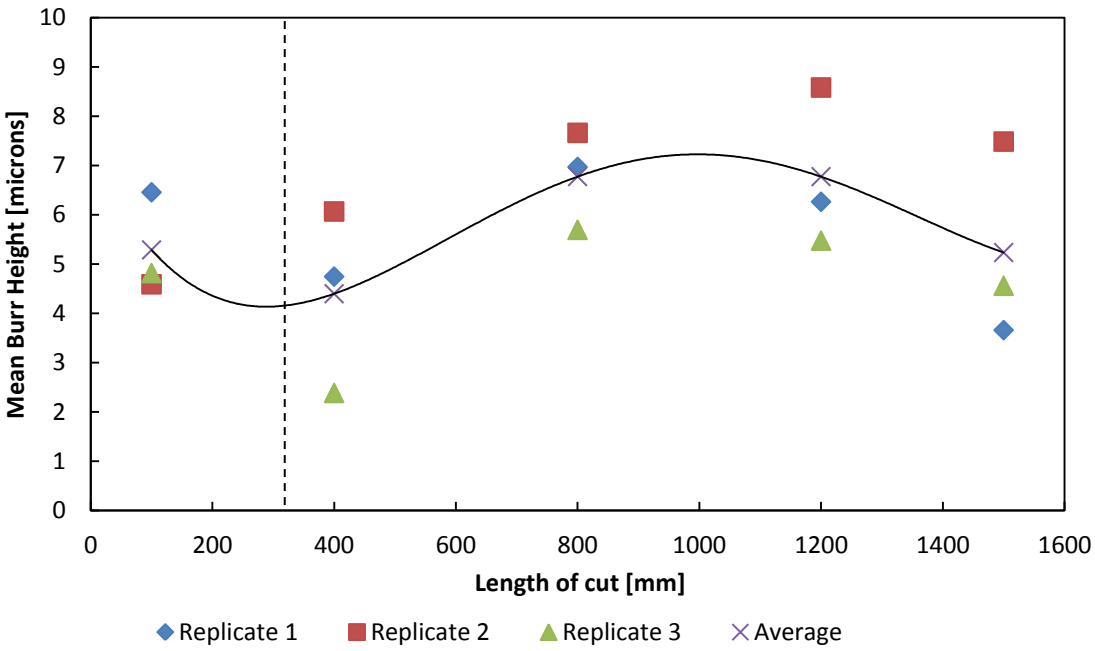

Figure 4.14: Mean burr height as a function of cutting length. Cutting condition: feed per tooth 32 microns per tooth; spindle speed 80,000rpm. The fitted line is a fourth order polynomial fit. The dotted line demarcates a cutting length of 360mm which is equivalent to the maximum cutting length of a given study.

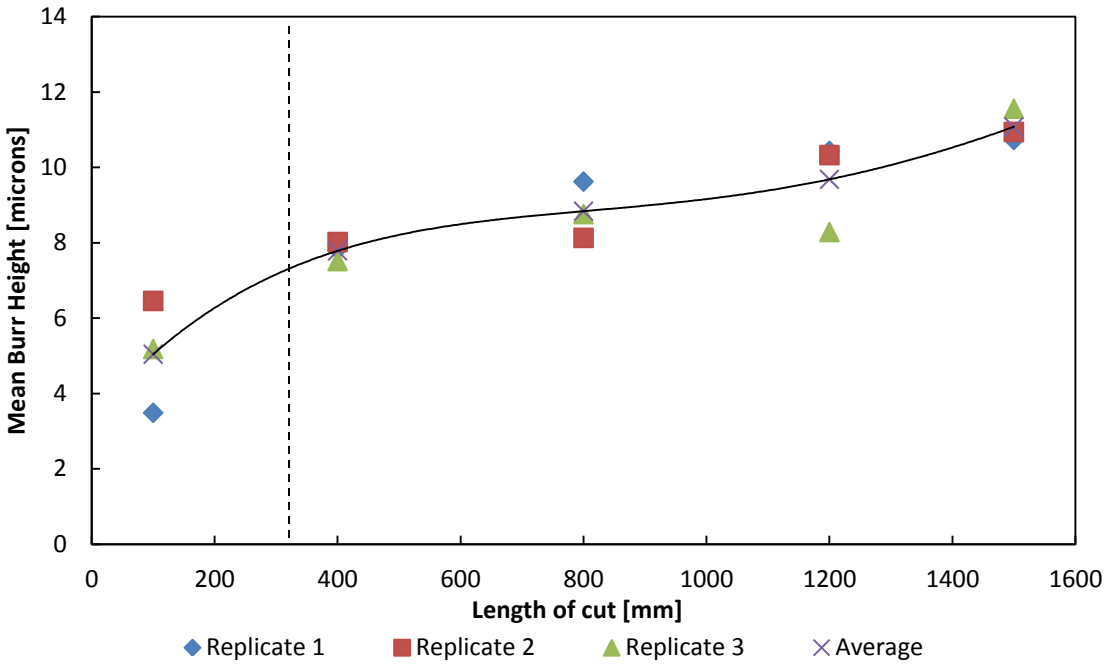

Figure 4.15: Mean burr height as a function of cutting length. Cutting condition: feed per tooth 7 microns per tooth; spindle speed 80,000rpm. The fitted line is a fourth order polynomial fit. The dotted line demarcates a cutting length of 360mm which is equivalent to the maximum cutting length of a given study.

4.8 Summary

Burring is presented as a sizable challenge to the HTPM of electrical steels. A coarse-fine experimental study is conducted to determine the optimal conditions of achieving maximum productivity and minimum burr formation. Interestingly, these conditions coincide, which is not often the case in engineering processes. At feeds of ≥7 microns per tooth and spindle speeds of ≥80,000 rpm peak burr heights and burring percentage can be greatly reduced and in some of the replicates altogether eliminated. Increasing the feed rate situates the cutting process in the shearing dominant regime as opposed to the more energy intensive plowing regime. Furthermore, increasing the spindle speed exhibits a further reduction in burr formation. No measurable delamination was observed during most of the experimental trials with only one of the test replicates exhibiting slight

delamination. This suggests that given sufficient spindle power and tool strength, laminated machining of stacks of electrical steel is achievable.

CHAPTER 5

CONSIDERING THE IMPACT OF PROCESS HISTORY ON MAGNETIC PROPERTIES OF M-19 ELECTRIC STEEL

5.1 Introduction

Abrasive waterjet machining has been proposed by the literature as a method to effectively process electrical steels while minimizing any degradation in performance of the material's magnetic properties[28]. This process utilizes a high pressure stream of water combined with an abrasive powder to cut through materials. The process is essentially a mechanical grinding process as the small abrasive particles remove bits of the workpiece while the water serves to flush the particles and the removed bits away. The machines are commonly used to conduct two dimensional cutting of metal plate material with high positional accuracy (+/- 0.003" at max traverse velocity for the model utilized in this study). This machine is often praised for its ease of use and effectiveness at cutting most materials with acceptable accuracy for conventional macro-scale parts. This study investigates the suitability of this process for the accelerated prototyping of electric machines as compared to the newly proposed HTPM. In particular these two processes will be compared based on their ability to shape the electrical steel laminates into the desired geometries necessary to produce the machines. Qualitative and quantitative analysis of the processes' performance is investigated, specifically the effects on magnetic properties of the post-processed electrical steel (as manifested by the specific core loss and permeability). Abrasive waterjetting is specifically selected as a comparison metric due to its position as the best known "flexible" processing technique at minimizing magnetic performance damage.

5.1.1 Magnetic Properties of M-19 Electrical Steel

As mentioned previously, the magnetic properties of M-19 steel are quite favorable for constructing electric machines. This electric steel is fully processed (i.e. the magnetic properties are fully developed and do not require additional annealing or post processing) and non-grain oriented. There will likely be some slight grain orientation due to the rolling process utilized to produce the sheets however this orientation is different from typical "grain oriented" electrical steel which is specifically developed to have enhanced magnetic properties in one direction. The grain oriented electric steels are commonly used in transformers and similar electrical machines. All magnetic properties available from the manufacturer are shown in Table 5.1.

Table 5.1: M-19 Material Properties.

*Tested at 1.5T and 60Hz according to ATM A677. Tests are conducted on 3 cm wide Epstein strips sheared half parallel and half transverse to the rolling direction.** Core loss specifically for M-19 and not M-15[79].

M-19 material properties*	values	units
Maximum Core loss**	1.55	Watts/lb
electrical resistivity	50	μohms*cm
hysteresis loss (Bmax=10kG)	0.0068	J/lb/cycle
Coercive force (Bmax=10kG)	0.41	Oersteds
Saturation induction	2.01	Tesla
Max permeability	8000	μ/μ_0

5.2 Experimental Approach

In order to effectively compare the two processes, several test specimens were cut from sheets of M-19 electrical steel using both processes. The best known processing condition was selected for the HTPM process as determined by previously discussed research. A high and medium quality setting (AWJ 5 and AWJ 3 respectively) was

selected for the abrasive waterjet machining process since the optimal parameters for this process were not known. Thus in order to make a valid comparison both high and medium qualities were selected. The quality setting essentially dictates the feed rate utilized by the machining center. A low quality setting was not selected due to the fact that this setting typically produces unacceptable parts. A constant thickness of a single sheet of electrical steel was used in the production of the samples via both processes. Thus a three level single factor experimental test matrix was developed as shown in Table 5.2. The commanded linear speed is the commanded maximum velocity. The average feed rate when cutting averages the velocity over the entire move and thus includes accelerations and decelerations as the machine tool head changes directions relative to the workpiece. Fifteen replicates will be conducted at each of these conditions resulting in a total of 45 tests. This is in order to provide a sizable data set around which to make observations concerning the characteristic behavior of the conditions. The tests are conducted in a randomized order to maintain statistical significance. The specimens are approximately 20mm x 60mm composed of a single laminate sheet of M-19 electrical steel. All of the samples are cut such that the longest dimension of the test piece runs parallel to the rolling direction to eliminate any potential influences this may have on the magnetic property comparison.

Table 5.2 Experimental Test Matrix

Test Number	Machining Process	Quality/ Feed Rate	Average Cutting Feed Rate [mm/sec]	Commanded Linear Speed [mm/sec]
1	AWJ	med quality (3)	16.3	18.7
2	AWJ	high quality (5)	10.1	10.4
3	HTPM	high feed rate	68.4	85.3

The performance metrics by which the processes are compared include burr formation (including peak burr height and average burr height), specific core loss, permeability, and qualitative optical evaluation of part quality. The specific core loss and permeability are evaluated at a standard AC frequency of 60Hz and at an induced magnetic field of 1.5 Tesla. A specially designed miniature test fixture is utilized to measure the magnetic properties of the samples. Furthermore, a digital microscope is utilized to perform the qualitative optical evaluation while a surface profilometer is used to characterize the burr formation.

The procedure for measuring the magnetic properties of these specimens involves inserting the test specimen into the test fixture and demagnetizing it to remove any initial magnetization of the sample. This is accomplished by applying an AC voltage large enough to induce a voltage in the test specimen above the saturation frequency of the specimen. Then this voltage is slowly and gradually lowered to zero, whereas the decreasing AC voltage serves to align the magnetic domains in the material in a random state. Subsequent to the demagnetization process, a sufficiently large AC voltage is applied to induce a voltage corresponding with the desired magnetic field strength (1.5 Tesla in this testing procedure). The voltages of the primary and secondary coils are recorded and then the voltage applied to the power circuit is removed. This process is repeated for each of the specimens to be tested.

5.3 Apparatus and Experimental Setup

In order to investigate the post-process magnetic properties of the electrical steels a specially designed testing fixture was constructed. This fixture is based off of the designs of previous research conduct by De Wulf et. al and operates along the same principles

and methodologies as the ASTM standard A804/A804M-04. [80, 81] developed a miniaturized test fixture capable of measuring smaller samples. This device is particular useful when investigating the magnetic properties of material of which you have a limited supply or of which the samples are actually quite small. Measurements made with this apparatus should in-fact correspond more precisely with actual real life performance inside electric machines since the samples are closer to the actual size of the rotor and stator teeth of many common machines.

Figure 5.1 illustrates this test fixture. It essentially behaves similar to a transformer. The test fixture incorporates a laminated stack of electrical steel, the test specimen and two coils of magnet wire. The laminated stack is M6 non-grain oriented electrical steel manufactured by Arnold Magnetics. The laminates of this stack were cut into the appropriate shape using an abrasive waterjet as this process has been previously suggested as the least disruptive to the magnetic properties. However, post processing of these laminates was required to remove the rusting that occurred along the cut edge even though the laminates were promptly removed and dried with an air jet immediately after the cutting process was completed.

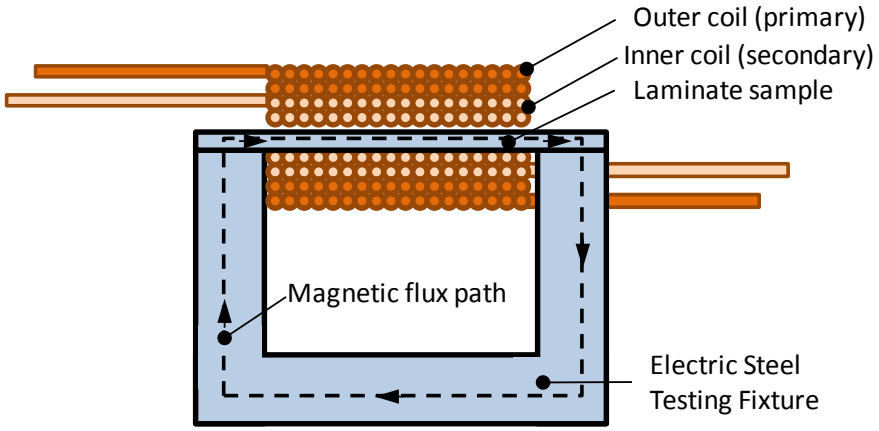

Figure 5.1 Magnetic testing fixture and schematic of fixture design

A nonconductive structure is fabricated and used to rigidly constrain the laminated stack while also serving as a winding bobbin for the copper coils. During testing, the specimen is placed through this bobbin with its ends contacting the top surface of the laminated stack of the test fixture. A 1kg mass atop a non-conducting structure applies even downward force onto these edges ensuring that a constant and uniform force is applied to guarantee that the test specimen maintains contact with the ends of the test fixture.

The two coils of the test fixture are wound concentrically. The outer coil acts as the power coil through which a current is supplied. This induces a magnetic field to flow through the test specimen. The magnetic field then flows through into the laminated stack and forms a complete circuit as illustrated in Figure 5.1. This flow of magnetic flux induces a current to flow in the inner secondary coil. Measurements can be made using this test fixture to determine magnetic properties of the specimen such as core loss and permeability. This fixture does not completely conform to the current ASTM standard in its miniaturized state; however, previous studies and its relatively simple operating principles imply that it is sufficient to make accurate comparisons amongst different specimen all tested on this same apparatus. Thus the results presented aim to provide comparative data between two different processes utilizing a common evaluation apparatus and technique.

Figure 5.2 presents an electrical circuit diagram of the setup used in the testing. The *V* points represent the location of the voltmeters. The left side of the diagram is the circuit connected to the secondary measurement coil while the right side corresponds to the

primary power coil. The resistor is a 10kΩ resistor. The AC power source is provided using a variac variable transformer.

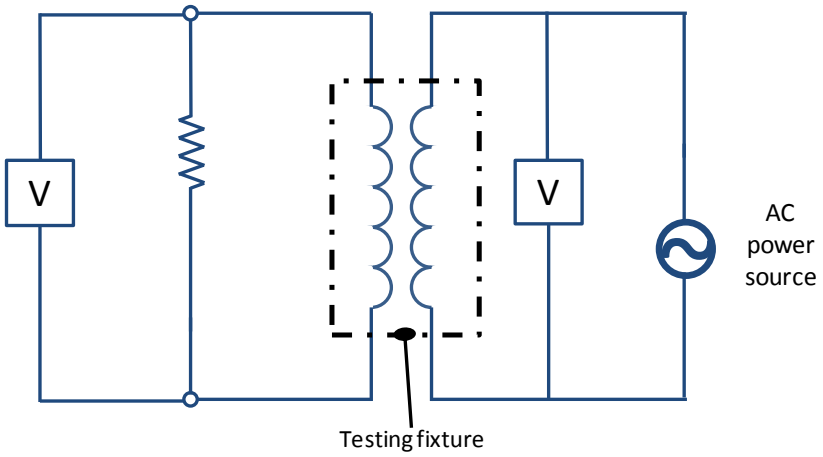

Figure 5.2 Circuit diagram of magnetic testing fixture

5.3.1 Specimen Preparation

The laminates for the fixture in addition to the samples to be tested are manufactured via abrasive waterjet machining using an Omax 2626 JetMachining Center. The machining center uses a preconfigured library of materials to assign the proper feed rate and pressure parameters. A material setting of 304 Stainless Steel (machinability 80.8, RB 53.3) was selected from this library. The laminates are sandwiched between thin pieces of plywood to provide the necessary rigidity to accurately fixture and cut the thin sheet of electrical steel. These outer sandwiches pieces of wood were mechanically fastened together with screws. A commanded thickness of 0.508mm and a tool offset of 0.381mm were selected to ensure that the machine cut through the entire stack of plywood and electrical steel. The laminates were machined under a pressure of 310MPa with an abrasive flow rate of 6.4 grams/second, an abrasive index of 0.95, and an abrasive mesh size of 80 (U.S. standard mesh). The laminates were removed from the

water and dried using compressed air immediately after the completion of the machining in order to minimize material degradation due to rusting. The inevitable rusting that did later occur was removed using an abrasive wire brush.

In order to produce the laminate samples for the HTPM condition a special fixture was also designed and constructed. Most of the author's previous work on HTPM includes tests through-cutting slots into the laminates which are rigidly fixtured on three ends. Thus a scaled extension of this fixturing technique is used and illustrated in Figure 5.3. This fixture incorporates a rigid aluminum frame which provides support and rigidity to the thin sheets of electrical steel. The ribs of the frame are specifically spaced to provide rigidity while also allowing sufficient spacing for the specimens to be cut. The frame is raised up and to allow clearance for the tool during the through-cut slotting. Furthermore, dowel pins are utilized to align the fixture with a linear axis of the desktop micromachining center used to perform the HTPM. A modal analysis is performed on the frame which determined that the natural frequencies of the fixture were far away from the intended excitation frequencies of the spindle. The sheet of electrical steel is attached to the frame via double coated adhesive tape and further constrained on the edges using tie-down blocks. The laminate samples are then milled from this setup. The micromachining center incorporates encoders to provide positional and velocity feedback control. The temporal positional data from this encoder can be recorded while the machine is milling a sample. This positional data can then be used to provide the velocity profile of the tool during the cutting process. This velocity profile is utilized to determine the average feed rate while cutting mentioned in Table 5.2.

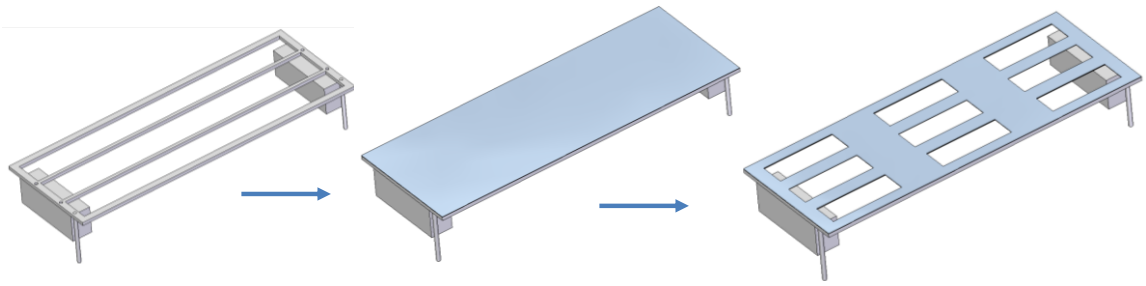

Figure 5.3 Machining fixture for producing HTPM laminate test samples.

5.3.2 Metrology

Each specimen is weighed using a Scientech SL 3000 balance to precisely determine its mass. The length of each specimen was also determined using Mitutoyo calipers. These values were recorded and used to provide accurate physical descriptions of the samples which will be necessary to calculate the core loss and magnetic permeability of the samples. Lingering tabs remaining from the machining processes that might potentially interfere with accurately measuring the lengths were removed prior to these measurements using a pair of shears.

A Talysurf 112, Taylor Hobson stylus profilometer was used to characterize the burr formation of the abrasive waterjet samples. A 15mm trace was taken along an edge of a test specimen (parallel to the longest dimension of the specimen). This trace also incorporated a portion of the flat un-burred surface of the specimen to serve as a datum to determine the actual distance of the burr height from the surface. The trace provides a characteristic surface profile of the burred portion of the test sample from which the peak burr height and average burr height can be determined. Additional optical qualitative evaluations of the cuts were made using a Keyence VHX-600 digital microscope.

The supplied voltage and induced voltage was measured using two digital lab multimeters: a Fluke 45 dual display digital multimeter and a Hantek 1200 handheld

oscilloscope/multimeter. These multimeters were also used to determine the resistance of the coils of the test fixture. The magnetic properties of the test specimens (specific core loss and permeability) are a function of the applied and induced voltages in addition to other geometrical and physical properties. Thus the voltages obtained from these multimeters are used to determine the magnetic performance of the test samples as discussed in the analysis section.

5.4 Analysis

The magnetic properties of the test specimens are calculated according to the ASTM standard A804/A804M-04. The mass (m), length (l) and density (ρ), as reported by the manufacturer) of the specimens are measured and used with Equation (5.1) to determine the active mass (m_1). The active mass of the specimen describes the actual portion of the sample that contributes to the flow of the magnetic flux. Equation (5.1) shows that this active mass is simply the mass scaled by an effective mean path length (l_1). The value of this mean path length is selected to correspond with the values used by De Wulf et. al as described in the literature[81]. The test set-up used in this study is identical to that reported by De Wulf et. al and it can logically be concluded that they should have equivalent mean path lengths. The effective cross sectional area (A) of each specimen is not measured but determined from the mass and measured length of the specimen as shown in Equation (5.2).

$$m_1 = m\frac{l_1}{l} \tag{5.1}$$

$$A = \frac{m}{\rho l} \tag{5.2}$$

5.4.1 Specific Core Loss

The core loss was calculated by measuring the power input into the test setup and comparing it to the power induced inside the secondary measurement coil. The power, as shown in Equation (5.3) is calculated by combining Joule's law and Ohm's law to yield a relation dependent on the input and induced voltage and their corresponding resistances. The voltage and resistance V_1, R_1 correspond to the power input circuit, while the voltage and resistance V_2, R_2 correspond to the secondary measurement circuit. The voltage and resistance are selected so as to eliminate the need to determine the phase angle between the current and power components of the alternating current waveform. The current in the secondary (induced) circuit was on the order of tens of micro-ohms indicating that the resistor serves to effective convert most of the energy in the circuit into the voltage that is used in the analysis of the magnetic properties.

$$P = \frac{V_1^2}{R_1} - \frac{V_2^2}{R_2} \tag{5.3}$$

This power loss is then converted into a specific core loss value for a given unit mass as shown in Equation (5.4). N_1 and N_2 correspond to the number of turns in the primary coil and the secondary coil respectively.

$$P_c = \frac{N_1}{N_2}\left(\frac{V_1^2}{R_1} - \frac{V_2^2}{R_2}\right)\frac{1}{m_1} \tag{5.4}$$

5.4.2 Permeability

The voltage required to obtain an induced magnetic field is determined using Equation (5.5). This relation enables us to correlate the induced voltage (E_f) to a corresponding magnetic field strength (*B,* which was set at 1.5 Tesla for this study) within the electrical steel sample at the specified frequency of (*f)* of 60Hz.

$$E_f = \sqrt{2}\pi BAN_2 f \tag{5.5}$$

The peak to peak voltage is utilized to determine the magnetic permeability of the samples at a specified frequency and induced magnetic field. This voltage is determined from the measured RMS voltage (V_{RMS}) in the primary circuit via Equation (5.6). This peak to peak voltage can finally be used in conjunction with Equation (5.7) to determine the relative permeability (P_μ) for the tested specimen, where Γ is the permeability of free space.

$$V_{p-p} = 2V_{RMS}\sqrt{2} \tag{5.6}$$

$$P_\mu = \frac{Bl_1}{\Gamma N_1\left(V_{p-p}/2R_1\right)} \tag{5.7}$$

5.5 Results

The specimens for the testing were manufactured as described above and then tested using the specially developed test fixture. The complete results of this testing is shown in Table 5.3. The specific core loss and permeability shown are calculated using the Equation described in the analysis section.

Table 5.3 Measured data from magnetic testing

Test number	Replicate	Length [mm]	Width [mm]	Mass [g]	Voltage in secondary circuit [mV]	Induced magnetic field (B) [Tesla]	Magnetic Field Strength (H) [Amps/meter]	Voltage in primary circuit [mV]	Active Mass [g]	Permeability at 1.5T	Specific Core Loss [W/kg]
1	1	60.08	20.08	3.09	268.5	1.499	1780.6	304.7	2.83	1339.8	3.32
1	2	60.09	20.07	3.10	269.3	1.499	1780.6	304.7	2.84	1340.3	3.10
1	3	60.08	20.11	3.11	270.6	1.501	1790.6	306.4	2.85	1334.8	3.18
1	4	60.05	20.11	3.13	272.8	1.503	1850.7	316.7	2.87	1292.9	5.14
1	5	60.00	20.11	3.13	272.8	1.501	1811.6	310.0	2.87	1319.8	3.48
1	6	60.07	20.10	3.11	270.3	1.499	1775.9	303.9	2.85	1344.1	2.65
1	7	60.01	19.88	3.07	267.3	1.500	1760.8	301.3	2.81	1356.7	2.81
1	8	60.15	20.04	3.05	264.9	1.500	1744.4	298.5	2.79	1369.2	2.76
1	9	59.79	20.00	3.08	269.9	1.504	1777.1	304.1	2.83	1347.9	2.81
1	10	60.08	20.03	3.10	269.3	1.499	1778.3	304.3	2.84	1341.9	3.01
1	11	60.00	20.01	3.10	269.6	1.498	1771.9	303.2	2.84	1346.4	2.66
1	12	60.01	20.04	3.12	271.3	1.498	1785.9	305.6	2.86	1335.9	2.79
1	13	60.01	20.02	3.09	269.0	1.500	1783.0	305.1	2.83	1339.6	3.28
1	14	59.89	20.05	3.07	267.9	1.501	1805.2	308.9	2.82	1323.7	4.52
1	15	59.96	20.02	3.11	270.8	1.499	1789.4	306.2	2.85	1334.0	3.07
2	1	60.01	20.00	3.10	269.8	1.500	1785.3	305.5	2.84	1337.5	3.17
2	2	60.04	20.02	3.07	267.5	1.502	1777.7	304.2	2.81	1345.5	3.47
2	3	59.97	20.02	3.11	270.7	1.499	1788.8	306.1	2.85	1334.2	3.07
2	4	59.80	19.89	3.06	267.8	1.503	1744.4	298.5	2.81	1371.7	2.00
2	5	60.01	20.02	3.08	268.6	1.503	1795.8	307.3	2.82	1332.4	3.94
2	6	59.88	19.88	3.08	268.9	1.501	1781.8	304.9	2.83	1341.4	3.26
2	7	59.82	19.86	3.07	268.7	1.503	1773.0	303.4	2.82	1350.1	2.95
2	8	59.86	19.92	3.06	267.0	1.500	1774.8	303.7	2.81	1345.5	3.47
2	9	59.94	19.95	3.06	266.9	1.501	1785.3	305.5	2.81	1338.9	3.94
2	10	59.92	19.94	3.05	265.3	1.496	1746.7	298.9	2.80	1364.2	2.74
2	11	59.89	19.90	3.06	266.6	1.498	1763.7	301.8	2.81	1352.6	3.11
2	12	59.92	19.95	3.06	266.4	1.498	1763.7	301.8	2.81	1352.3	3.16
2	13	59.96	19.95	3.06	266.6	1.500	1759.0	301.0	2.81	1357.8	2.92
2	14	59.85	19.89	3.06	267.2	1.501	1758.4	300.9	2.81	1358.8	2.74
2	15	59.84	19.88	3.05	266.4	1.501	1744.4	298.5	2.80	1369.9	2.36
3	1	59.99	20.05	3.10	270.0	1.500	1803.4	308.6	2.84	1324.6	3.88
3	2	60.02	20.09	3.10	269.8	1.500	1768.9	302.7	2.84	1349.9	2.50
3	3	60.01	20.08	3.10	269.4	1.497	1769.5	302.8	2.84	1347.4	2.61
3	4	60.00	19.96	3.11	270.7	1.499	1791.1	306.5	2.85	1333.1	3.17
3	5	60.01	20.02	3.13	272.7	1.501	1780.6	304.7	2.87	1342.5	2.21
3	6	59.92	19.98	3.08	268.5	1.500	1780.0	304.6	2.83	1341.7	3.29
3	7	59.98	20.01	3.08	268.6	1.502	1761.3	301.4	2.82	1357.8	2.49
3	8	59.95	20.03	3.11	270.0	1.494	1787.1	305.8	2.85	1331.6	3.18

Table 5.3 Continued: Measured data from magnetic testing

Test number	Replicate	Length [mm]	Width [mm]	Mass [g]	Voltage in secondary circuit [mV]	Induced magnetic field (B) [Tesla]	Magnetic Field Strength (H) [Amps/meter]	Voltage in primary circuit [mV]	Active Mass [g]	Permeability at 1.5T	Specific Core Loss [W/kg]
3	9	60.00	20.01	3.09	269.4	1.502	1785.3	305.5	2.83	1339.6	3.28
3	10	59.94	19.97	3.08	268.7	1.502	1782.4	305.0	2.83	1341.5	3.33
3	11	59.93	19.98	3.13	272.3	1.497	1797.6	307.6	2.87	1326.1	3.01
3	12	59.94	19.99	3.13	272.8	1.500	1803.4	308.6	2.87	1324.4	3.13
3	13	59.99	20.02	3.12	271.7	1.500	1815.7	310.7	2.86	1315.5	3.94
3	14	60.00	20.00	3.10	267.7	1.488	1768.4	302.6	2.84	1339.6	2.99
3	15	59.97	20.01	3.10	270.0	1.500	1802.8	308.5	2.84	1324.6	3.85

This data is also plotted in Figure 5.4 and Figure 5.5 to provided additional insight into these specific characteristics. A box-plot format is utilized to show multiple facets of the data statistics. The height of the wide blue bars indicates the mean value for all the replicates at each condition. The slightly thinner grey error bars indicated the standard deviation of the sample distribution above and below this average. Finally the thinnest black error bars indicate the maximum and minimum extreme values measured at each of the conditions. Typically these extremes lie outside the standard deviation; however, in the first condition of Figure 5.5, the lower extreme was much smaller than the upper extreme and thus the standard deviation (determined by the total variance of the sample) extends beyond this lower extreme.

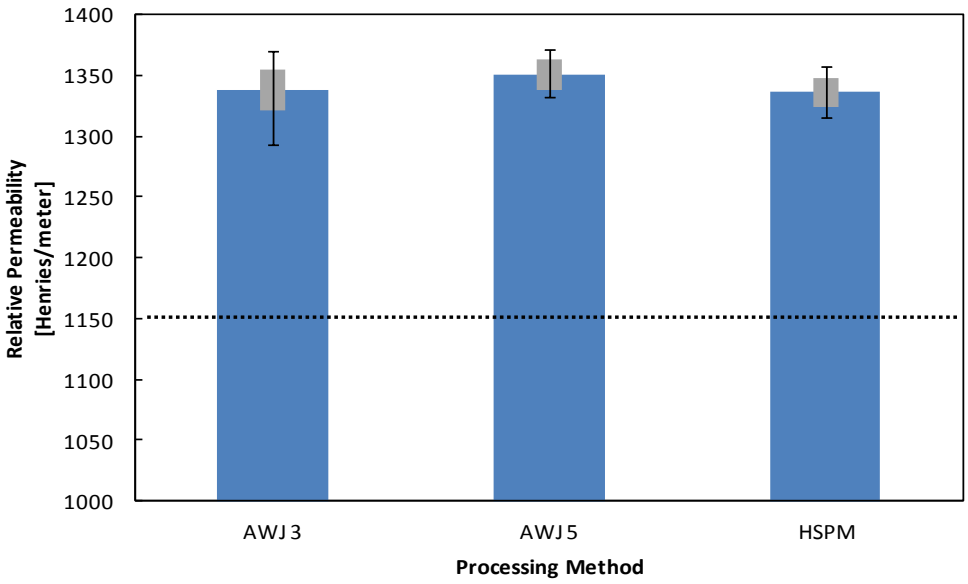

Figure 5.4 Average permeability for different processing methods. Permeability was measured at 60Hz and 1.5T. The dotted line indicates the typical minimum permeability for this material.

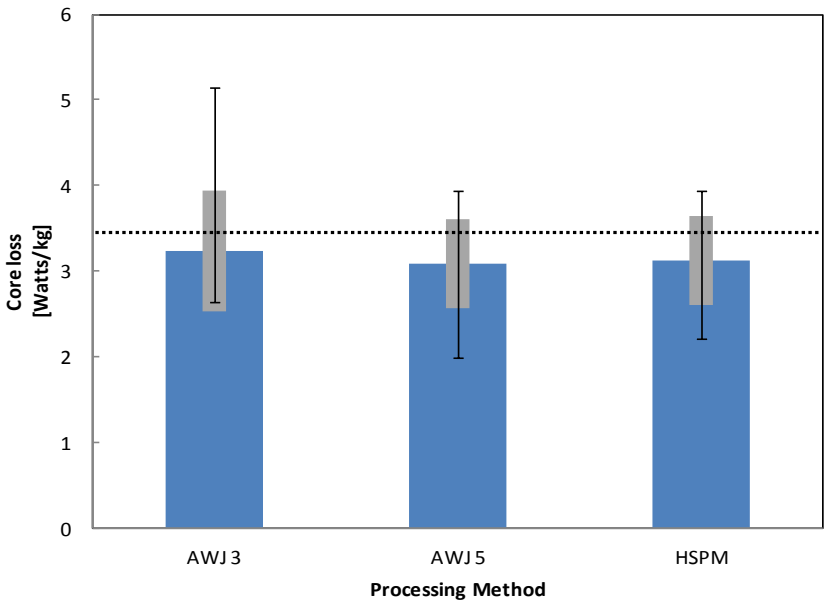

Figure 5.5 Average specific core loss for different processing methods. Specific core loss was measured at 60Hz and 1.5T. The dotted line indicates the required maximum allowable core loss by the ASTM standard.

AWJ 3 and AWJ 5 exhibited average core losses of 3.23W/kg and 3.08 W/kg respectively while the HTPM samples exhibited a core loss of 3.12W/kg. With regard to

the permeability, AWJ 5 exhibits the highest permeability of 1350H/m; while HTPM yielded a value of 1336H/m and AWJ 3 exhibited a permeability of 1337H/m.

5.5.1 Experimental Uncertainty

A further investigation into the experimental uncertainty is warranted to validate the previous observation concerning the magnetic properties. Kline-Mcclintock error analysis is conducted on the testing fixture and results in an experimental uncertainty on the same order as the measured values (average of 2.67[W/kg] for AWJ 3, 2.65[W/kg] AWJ 5, 2.674[W/kg] for HTPM). The uncertainty due to the resistance in the circuit exhibited the largest effect on the overall uncertainty. Equation (5.8) describes the partial used to compute this resistance uncertainty. Note the squared voltage term which explains why the resistance uncertainty has such a large effect.

$$\frac{\partial P_c}{\partial R} = \frac{V_1^2 l}{R^2 m m_1} \tag{5.8}$$

The uncertainties in the instruments utilized in this study are shown in Table 5.4. Potential improvements in uncertainty could be achieved by incorporating additional circuitry to better measure the resistance, which will reduce the resistance uncertainty. However, reducing this uncertainty down to a negligible value (zero) will result in an uncertainty that is much larger than the difference between the processes (~0.9 W/kg).

Table 5.4 Measurement Equipment and Reported Accuracy

	Measurement type	Accuracy	Units
Fluke 45 Dual Display Multimeter	Induced Voltage	0.2%	mV
	Resistance	0.05%+0.02 Ohms	Ω
Scientech SL 3000 balance	Mass	0.001	g
Hantek 1200 Oscilloscope/Multimeter	Voltage Input	1%	mV
Mitutoyo Calipers	Length	0.01	mm

It is common practice in similar pervious works comparing the effect of process parameters on magnetic properties to simply utilize the mean of the experimental data, while simply citing the experimental uncertainty. An important goal of the study has been to make a relative comparison between the processes especially since previous studies have quoted AWJ as the best process from an electromagnetic property perspective. Thus in order to reduce the error in this study several replicates were conducted (15 at each condition). Even though all the replicates were conducted at a constant condition, significant variance was observed indicating that the process does not yield a high level of repeatability to the desired degree of consistency or that the magnetic properties of these samples does not seem to be constant and in fact could vary throughout the material (within a single roll or batch of electrical steel). This latter conjecture is further reinforced by knowledge of the means in which the manufacturer sorts the material. All the material is guaranteed to be below a certain value of core loss of 3.42 W/kg. Thus more stringent process control on the manufacturing process may be necessary to definitively report on the relative capabilities and effects that the different processing methods have on the post produced material.

However, to circumvent the current material and manufacturing process constraints, a pooled estimate statistical hypothesis test is conducted to enable definitive conclusions concerning the relative permeability and core loss between the two processes to be drawn. A Gaussian distribution for the (core loss and permeability) of the specimen populations is assumed. The hypothesis test is performed on both core loss values and permeability values separately. Moreover, since the test is a simple 1 to 1 comparison, the test is conducted comparing HTPM to AWJ 3 and comparing HTPM to AWJ 5. Thus we

are computing the mean of the difference of the two processes as shown in Equation (5.9) and Equation (5.10) (for specific core loss).

$$\bar{\mu}_{0,(AWJ3,HTPM)} = P_{c,AWJ3} - P_{c,HTPM} \tag{5.9}$$

$$\bar{\mu}_{0,(AWJ5,HTPM)} = P_{c,AWJ5} - P_{c,HTPM} \tag{5.10}$$

Assuming, as an initial hypothesis (H_o), no change in the resulting magnetic properties of the two processing methods (e.g. difference between average core loss of AWJ 3 and HTPM (μ_o) is zero), the opposite or alternative hypothesis (H_A) is then evaluated using a statistical hypothesis test decision table shown in Table 5.5. This will confirm or deny the validity of the hypothesis (Ho) and indicate how μo (mean of the difference of our sample sets) compares to the true mean (μ) of the difference of the sample sets of the entire population.

Table 5.5: Decision Table for Hypothesis Test

H_A	**Reject H_0 if:**
$\mu<\mu_0$	$\bar{x} < C_{min}$
$\mu > \mu_0$	$\bar{x} > C_{max}$
$\mu \neq \mu_0$	$\bar{x} <C_{min}$ or $\bar{x} >C_{max}$

The C_{min} and C_{max} values are calculated using Equation (5.12) and (5.13) involving the T-statistic (calculated at a 95% confidence interval), and *n* (number of tests for a given sample set), and the standard deviation of the sample set (the square of which is calculated in Equation (5.11)).

$$s^2 = \frac{(n_1 - 1)s_1^2 + (n_2 - 1)s_2^2}{n_1 + n_2 - 2} \tag{5.11}$$

$$C_{\min} = \mu_0 - t_{(n_1+n_2-2),\alpha/2} s \sqrt{\frac{1}{n_1} + \frac{1}{n_2}} \tag{5.12}$$

$$C_{\max} = \mu_0 + t_{(n_1+n_2-2),\alpha/2} s \sqrt{\frac{1}{n_1} + \frac{1}{n_2}} \tag{5.13}$$

Computing these values and comparing them according to the decision table enables us to draw conclusive comparison between the processes effects on magnetic properties at a 95% confidence level. Table 5.6 and Table 5.7 present the results of this comparison.

Table 5.6: Specific Core Loss Comparison Results of Hypothesis Test.

	s^2	$\bar{x}$	C_{min}	C_{max}	Permeability Comparison (at 95% confidence)
HTPM vs. AWJ5	0.27	0.04	-0.39	0.39	$P_{c,HTPM}=P_{c,AWJ5}$
HTPM vs. AWJ3	0.38	-0.11	-0.46	0.46	$P_{c,HTPM}=P_{c,AWJ3}$

Table 5.7: Permeability Comparsion Results of Hypothesis Test

	s^2	$\bar{x}$	Cmin	Cmax	Permeability Comparison (at 95% confidence)
HTPM vs. AWJ5	144.4	-14.20	-8.99	8.99	Pμ,HTPM<Pμ,AWJ5
HTPM vs. AWJ3	215.3	-1.81	-10.98	10.98	Pμ,HTPM=Pμ,AWJ3

The resulting core loss of the two processes is statistically the same. There is only an 8% chance that AWJ 5 may yield a lower core loss than HTPM. Furthermore there is a 19% chance that HTPM has a lower core loss than AWJ 3. With regard to the

permeability HTPM exhibited a statistically significant lower permeability than AWJ5. However, it has the same permeability as AWJ 3. There is only a 13.5% chance that AWJ has a greater permeability than HTPM.

5.6 Discussion

5.6.1 Burr Formation and Oxidation

To effectively compare the capabilities of the proposed HTPM to that of other existing manufacturing process, several preliminary benchmarking tests were performed. An Omax abrasive waterjet was used to cut sample pieces out of the electrical steel. These pieces were promptly removed, dried, and then viewed under the digital microscope. Despite the relatively short period of time (mere minutes) that the material was in contact with water, rusting, visible to the naked eye, was observed. This rust is non-conductive and takes up more space than the original steel potentially resulting in undesirable part deformation and possible electromagnetic problems. Thus this rusting necessitates a secondary process to remove the corrosion from the laminates. Figure 5.6 below clearly shows some of this rusting on an electrical steel sheet from which several pieces have been cut.

Figure 5.6 Oxidation occurring on electric steel after abrasive waterjetting, despite prompt removal of water via compressed air.

Furthermore, significant burr formation was observed even when waterjetting at the highest quality setting available. The burring measured from the milling process was significantly smaller than that observed from the preliminary samples cut via AWJ machining, with the average peak heights being less than half the height of those produced by the abrasive process. It was initially assumed that waterjetting at lower quality setting will only result in greater burring as theses settings typically produce lower surface finishes. However, the profilometric data obtained after a more thorough investigation measurement of the burred samples indicates otherwise. Three replicate samples of each AWJ machining condition tested were measured using the profilometer. The averages of these replicates are shown in Figure 5.7. These seem to suggest that the burr formation is the same or worse as the quality improves.

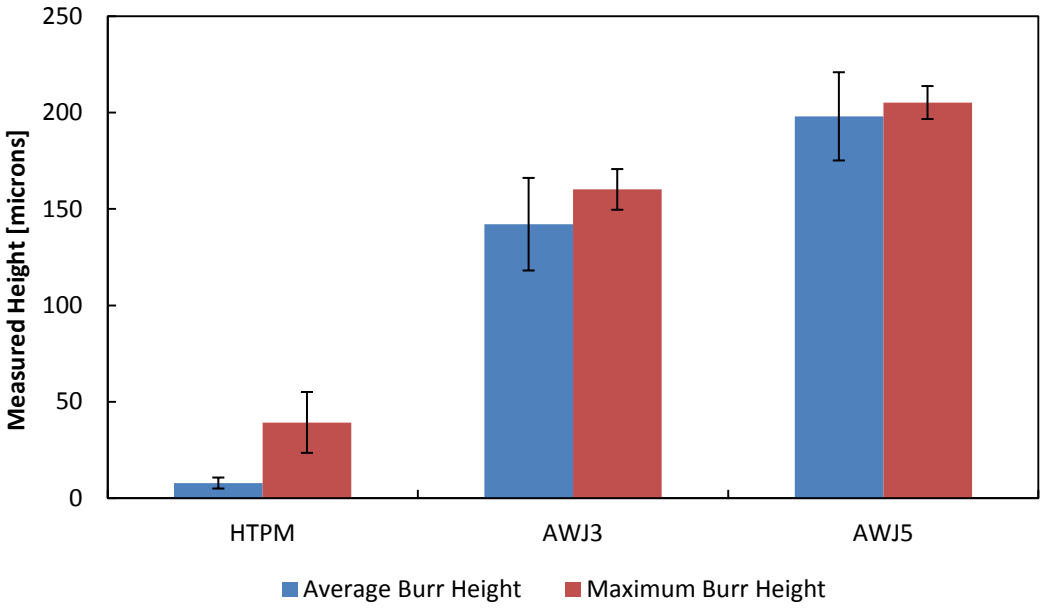

Figure 5.7 Peak burr height and average burr height for abrasive waterjet samples at two conditions compared to HTPM. The error bars indicate the standard deviation amongst the measured samples.

Comparing these burr heights to the burr height values previously obtained utilizing HTPM, it is apparent that a 4x increase in peak burr height and a 16x increase in average burr height along the cut. Moreover, unlike the cuts observed from the HTPM, the burring was very consistent along the length of the cut and virtually 100% of the edge was burred. Figure 5.8 illustrates some of this burring. The resulting burring can lead to assembly issues by increasing the difficulty in forming the laminate stacks. Wire winding problems could also result as the burrs could snag the wires during winding and even abrade some of the insulation away. Finally, potential magnetic field problems could result (since the jagged surface could result in magnetic short circuiting and interlaminar short circuiting). It is noteworthy that the burring did occur primarily on one side of the sample (the bottom facing side) similar to the milling process (which however occurred on the top facing side).

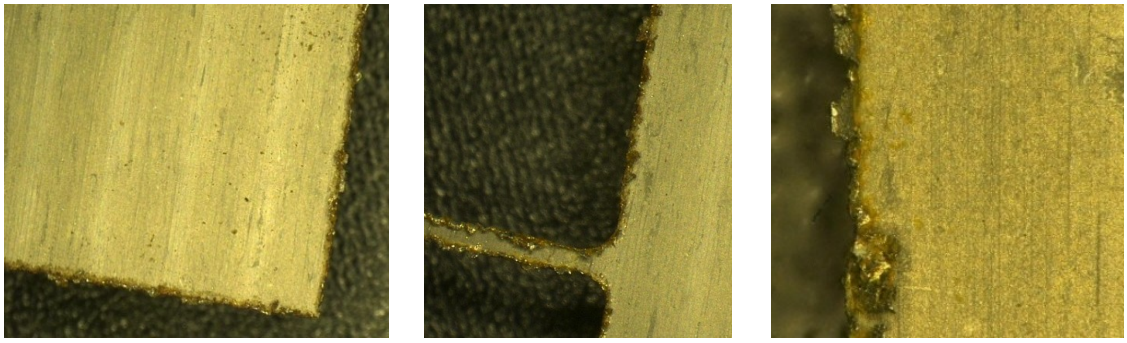

Figure 5.8 Rusting and burr formation at different locations along the edge of abrasive waterjet machined pieces of M-19 electrical steel illustrating consistent burring along the edge. The far right image is a magnification of the far left image revealing the burred edge.

Overall, this indicates that the process in general is not very effective at creating a clean cut for precision manufacturing of small laminates. Furthermore, in comparison HTPM is capable of producing clean cuts without the need for secondary processing to remove burrs and without significant rusting.

5.6.2 Magnetic Properties

The data presented in the results section concerning the core loss shows that the two processes result in a virtually identical core loss values. This is verified by the statistical analysis of the data via hypothesis testing. The hypothesis test did conclude that the permeability of AWJ 5 was statistically greater than HTPM however the difference between the two sample means was only 14 H/m corresponding to a 1% change in permeability. Since the permeability is not guaranteed by the manufacturer it is difficult to say whether this change is in fact a manifestation of the process parameters studied here or the manufacturer's production processes. These results seem to suggest that the magnetic performance of these two processes is comparable and that there is no significant difference between the core loss and permeability at the tested conditions. The manufacturer states that the maximum allowable core loss, 3.42W/kg, correspond with ASTM standard A 677-07 and this is verified by the data observed. The core loss values measured correlate well with the ASTM standard for this type of material. This correspondence serves as a further indicator that the results obtained are accurate despite the experimental uncertainty.

5.6.3 Productivity

The HTPM is accomplished at a rate 4x faster than the quality 3 AWJ machining and 6.7x faster than the high quality abrasive. These feed rates can also theoretically be doubled to 8x and 13.4x by simply using a four fluted endmill instead of a 2 fluted endmill and cutting at the same conditions. Moreover, the capability of cutting laminated stacks of electrical steel enables another increase in production rate. However, productivity must be properly defined as considering production rate and part quality.

HTPM achieves drastically less burr formation and no observable rusting when compared to AWJ machining. This has a significant effect on the laminate component because burrs and rust corrosion must be removed prior to the assembly of an electric machine. For the (statistically) same magnetic performance increases in feed rate and decreases in burr formation are attainable resulting in a noteworthy increase in productivity. Consequently HTPM possesses a significant advantage from a manufacturing perspective.

5.7 Summary

All of the results of this study should be considered holistically when comparing the two manufacturing processes. Table 5.8 summarizes the primary differences investigated in this study. HTPM exhibits a substantial decrease in average and peak burr formation while also not exhibiting any observable delamination or oxidation. A statistical analysis concluded that the two processes yield the same core loss; however, the average core losses obtained are presented in the table for completeness. The analysis also indicated that HTPM yields the same permeability as AWJ 3 but exhibits a 1% decrease in permeability relative to AWJ 5.

Table 5.8 Comparison Metric for Abrasive Waterjet Machining and HTPM

	Maximum Burr Height [microns]	Average Burr Height [microns]	Feed Rate [mm/sec]	Average Core Loss [Watts/Kg]	Average Permeability [Henries/meter]	Oxidation
AWJ 3	160	142.1	18.7	3.23	1337.8	Yes
AWJ 5	205	197.9	10.4	3.08	1350.1	Yes
HTPM	39	7.8	85.3	3.12	1335.9	No
Direction of improvement	Lower is better	Lower is better	High is better	Lower is better	High is better	

This chapter presents a comparison of the effects of two machining processes on the shaping of electric steel sheets in to appropriate geometries for stator and rotor

components of electrical machines. The change in magnetic performance was quite small and changes indicated by the collected data fell within the range of instrumental uncertainty. However, the further analysis of the data did enable definite conclusions to be drawn.

This work presents a previously unexplored comparison between the resulting magnetic properties of electrical steel laminates after AWJ machining and HTPM. Furthermore it discusses the manufacturability advantages between the two processes. AWJ machining exhibits significant rusting, burring, and exhibits difficulty in processing laminated and miniature parts. HTPM is theoretically capable of a 13x improvement in processing speed, without significant burring or rusting issues.

CHAPTER 6

SUMMARY AND CONCLUSIONS

6.1 Summary

This work has investigated the manufacturing processes incorporated into the production of the stator and rotor laminates of electric machines. The production of these machines has been identified as a rapidly emerging field for multiple industries, and as a consequence, is a critical area for research and development. As demands for more energy-dense and energy-efficient electric machines rise, developers will be forced to create better designs for these machines. An effective prototyping process is essential to quicken the design cycle and enable effective optimization of these machines. The current production processes for prototyping the laminated components of electric machines (specifically: abrasive waterjet machining, electric discharge machining, laser beam machining) exhibit various benefits for producing these machines in their own rights but none seems to be effectively optimized for the accelerated prototyping of electric machines. Thus HTPM is proposed as a novel prototyping process.

The processing of the electrical steels that comprise electric machines is quite a complex process. The materials exhibit significant material toughness which results in increased energy requirements to precisely shape the material. Furthermore, this toughness results in significant strains manifested as burrs whenever this material is mechanically deformed. The electric steels are very sensitive to water environments as they rust readily and the material is also very sensitive to deformation of its grain structure via both mechanical and thermal processes. Changes to this grain structure can result in damage to the magnetic properties and an ultimate decrease in the performance

of the final electric machine. Significant research has been completed to better understand these effects with respect to the various processing techniques currently in use. However, the governing phenomena describing these materials and their responses to various shaping processes have not been completely understood. Finally, optimizing the processing techniques to achieve the production rates necessary to realize accelerated prototyping while also minimizing the degradation of the material properties of the electric steel remains a challenge.

In this work, several sets of experiments have been conducted to explore the applicability of HTPM to the production of electric steel laminates. Experiments have been conducted to determine the best cutting parameters for processing the electrical steel in addition to determining the specific cutting energy and force ratio of M-19 electric steel. Additional experiments have also been conducted to determine the process parameters that maximize productivity and minimize burr formation. These two objectives actually coincide at the same processing conditions. Furthermore, machining of laminated stacks of electric steel has also been realized with experiments showing no significant delamination during the cutting process. Finally a comparison is made between the effects on the magnetic properties of electrical steel resulting from processing via abrasive waterjet machining and HTPM. The processing capabilities and resulting magnetic properties of the post-machined components are evaluated. Specifically, permeability and specific core loss are compared. HTPM exhibits similar magnetic performance characteristics to the abrasive waterjet machining process.

6.2 Conclusions

Pursuant the work summarized above and presented in the preceding chapters the following conclusions were made:

- Specific cutting of M-19 electrical steel was determined as a function of feed per tooth to be: $K_s = 3342.2 f_t^{-0.198}$
- The force ratio of M-19 electrical steel was determined as a piecewise function of feed per tooth to be: $K_{r1} = 1.0649 f_t^{-0.121}$ *and* $K_{r2} = 0.1305 f_t^{0.4298}$
- Specific cutting energy decreases with increasing spindle speed when processing M-19 electrical steel via HTPM.
- A rigorous non-linear multivariable fitting algorithm capable of determining specific cutting energies and force ratios from empirical data was developed.
- Burr formation was minimized by cutting at high feeds per tooth and high spindle speeds.
- Optimal cutting conditions were determined to be:

  spindle speeds ≥ 80,000rpm and feeds per tooth ≥ 32 microns per tooth.
- Minimum mean burr heights of 6.7 microns were achieved.
- Minimum peak burr heights of 27 microns were achieved.
- HTPM and AWJM exhibit statistically identical core loss.
- AWJM at its highest quality setting exhibits a 1% increase in permeability vs. HTPM.
- HTPM exhibits multiple times increase in linear feed rate vs. AWJM, capable of machining at 85.3 mm/second.
- HTPM exhibits order of magnitude decrease in burr formation vs. AWJM.

6.3 Publications

Pursuant to the work summarized above and presented in the preceding chapters the following contributions were made:

Liles, H.J. and Mayor, J.R. "Initial Study on the High-Speed, High-Precision Micromilling of Laminated Electric Steels," *Proc. of the 7th International Conference on MicroManufacturing*, 2012, pp. 110-117

Liles, H.J. and Mayor, J.R. "Initial Investigation into Helical Milling of Laminated Stacks of Electrical Steel," *Proceedings of the ASME 2012 International Manufacturing Science and Engineering Conference*, 2012

Liles, H.J. and Mayor, J.R. "Application of High Throughput Profile Milling to the Production of Laminates for Electric Machines," *Proceedings of the International Electric Machines and Drives Conference, 2013 IEEE International, 2013**

Liles, H.J. and Mayor, J.R. "Investigation of High-Speed Profile Milling of Laminated Electric Steels," *Transactions of the ASME: Journal of Manufacturing Science**

Liles, H.J. and Mayor, J.R. "Optimization of Cutting Parameters of Electrical Steel for Maximum Productivity and Minimum Burr Formation," *Transactions of the ASME: Journal of Manufacturing Science**

* - Pending publications

6.4 Recommendations for Future Work

- Determination of optimum feed cutting parameters

This work investigates the material response of M-19 up to the limits of the testing machine tool. The results indicated that feeding faster produced less burr formation. Tests

should be conducted to determine if an upper feed limit exists with regard to burr formation and delamination.

- Determination of ideal fixturing technique for HTPM of electrical steel laminates

  This work incorporated through-cut slot milling as a means of processing the electrical steel laminates in order to minimize tool breakage and investigate only the properties of the electrical steel. However, this setup produces significant vibration and undesirable dynamic effects. Additional study should be conducted to find an ideal solution to fixturing the laminates and laminates stacks during prototyping.

- Investigation of limits of processing laminated stacks of electrical steel via HTPM

  The capabilities of HTPM processing of electrical steels are ultimately limited by tool geometry and tool strength. However, these precise limits have yet to be determined. A study investigating the maximum achievable laminated stack height and corresponding feed rate should be conducted. Furthermore, an optimal combination of stack height and material removal rate should also be determined.

- Analysis of other electrical steel grades

  Electrical steel grades other than M-19 should be investigated to increase the flexibility of the HTPM process to produce components for machines incorporating different magnetic material requirements. Specific cutting energies for other common grades such as M-6, M-4 and even Hiperco should be determined and compared to those corresponding to M-19 presented in this work.

- Revised magnetic testing samples

  Future work concerning the difference between the resulting magnetic properties of these two processes should endeavor to better observe the processing effects by

decreasing the ratio of the region of unaffected electrical steel to the region of steel affected by the processing. A sample of electrical steel can be cut with multiple lines of "material deformation" to yield a specimen that should exhibit greater sensitivity to the material processing. Figure 6.1 illustrates a possible configuration of a future test specimen. This new specimen design should yield a better understanding of the effects that the processing condition used to shape the steel have on its magnetic properties.

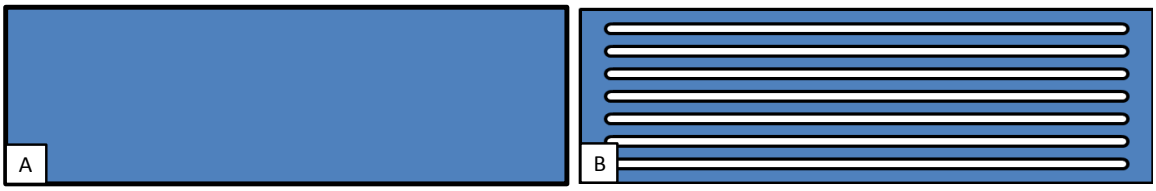

Figure 6.1: (A) Specimen used for this study. (B) Future specimen design with increased process affected area. Note that the dark border around the edge of image A and around the internal cuts of image B indicates process affected area.

REFERENCES

[1] carreviewsratings.net. (2011). Available: http://carreviewsratings.net/wp-content/uploads/2011/03/2011-Chevrolet-Volt.jpg

[2] MyPerfectAutomobile.com. (2010). Available: http://www.myperfectautomobile.com/wp-content/uploads/2010/11/nissan-leaf-specs.jpeg

[3] Okuma, "Okuma announces new machine to be unveiled at IMTS 2012," 2012.

[4] Nakanishi. (2013). *Product Literature*. Available: http://www.nsk-nakanishi.co.jp/industrial-eng/hpms/

[5] HAAS. (2013). *Product Literature*. Available: http://www.haascnc.com/vmc_intro.asp

[6] C. Zwyssig*, et al.*, "An Ultra-High-Speed, 500000 rpm, 1 kW Electrical Drive System," 2007, pp. 1577-1583.

[7] J. Kunz*, et al.*, "Design of a 750,000 rpm switched reluctance motor for micro machining," 2010, pp. 3986-3992.

[8] Boeing. *Boeing 787 from the ground up*. Available: http://www.boeing.com/commercial/aeromagazine/articles/qtr_4_06/article_04_3.html

[9] O. o. P. Affairs, "Secretary Chu Awards $9.6 Million for Transformational Energy Research Projects," T. D. O. ENERGY, Ed., ed, 2010.

[10] B. Obama, "Remarks by the president in state of union address," O. o. t. P. Secretary, Ed., ed. Washington D.C., 2011.

[11] B. Obama, "Remarks by the president in state of union address," O. o. t. P. Secretary, Ed., ed. Washington D.C., 2012.

[12] M. S. Sarma, *Electric machines: Steady-state theory and dynamic performance*: WC Brown, 1985.

[13] W. F. Smith, "Structure and properties of engineering alloys," 1993.

[14] ASM, "Asm Handbook: Properties and Selection : Nonferrous Alloys and Special-Purpose Materials (Asm Handbook) " vol. VOL. 2, ed: ASM International, 1991.

[15] K. Ho and S. Newman, "State of the art electrical discharge machining (EDM)," *International Journal of Machine Tools and Manufacture,* vol. 43, pp. 1287-1300, 2003.

[16] K. H. Ho*, et al.*, "State of the art in wire electrical discharge machining (WEDM)," *International Journal of Machine Tools and Manufacture,* vol. 44, pp. 1247-1259, 2004.

[17] S. Kumar, *et al.*, "Surface modification by electrical discharge machining: A review," *Journal of Materials Processing Technology,* vol. 209, pp. 3675-3687, 2009.
[18] F. Ghanem, *et al.*, "Influence of steel type on electrical discharge machined surface integrity," *Journal of Materials Processing Technology,* vol. 142, pp. 163-173, 2003.
[19] A. K. Dubey and V. Yadava, "Laser beam machining—A review," *International Journal of Machine Tools and Manufacture,* vol. 48, pp. 609-628, 2008.
[20] P. Baudouin, *et al.*, "Effects of laser and mechanical cutting modes on the magnetic properties of low and medium Si content nonoriented electrical steels," *Magnetics, IEEE Transactions on,* vol. 38, pp. 3213-3215, 2002.
[21] P. Baudouin, *et al.*, "Effect of the rapid heating on the magnetic properties of non-oriented electrical steels," *Journal of magnetism and magnetic materials,* vol. 328, pp. 221-5, 2002.
[22] A. Belhadj, *et al.*, "Simulation of the HAZ and magnetic properties of laser cut non-oriented electrical steels," *Journal of magnetism and magnetic materials,* vol. 248, pp. 34-44, 2002.
[23] A. Belhadj, *et al.*, "Effect of laser cutting on microstructure and on magnetic properties of grain non-oriented electrical steels," *Journal of magnetism and magnetic materials,* vol. 256, pp. 20-31, 2003.
[24] D. Gaworska-Koniarek, *et al.*, "The influence of assist gas on magnetic properties of electrotechnical steel sheets cut with laser," 2011, p. 012091.
[25] R. De Graaf and J. Meijer, "Laser cutting of metal laminates: analysis and experimental validation," *Journal of Materials Processing Technology,* vol. 103, pp. 23-28, 2000.
[26] J. H. O. J. Zeng. (10/27/2011). *Technical description of abrasive waterjets*.
[27] A. Boehm and I. Hahn, "Influence of turning on the magnetic properties of electrical steel in the production of electrical machines," in *Electric Machines & Drives Conference (IEMDC), 2011 IEEE International*, 2011, pp. 83-88.
[28] A. Schoppa, *et al.*, "Influence of abrasive waterjet cutting on the magnetic properties of non-oriented electrical steels," in *SMM15, September 5, 2001 - September 7, 2001*, Bilbao, Spain, 2003, pp. 370-372.

[29] D. Shanmugam, *et al.*, "A study of delamination on graphite/epoxy composites in abrasive waterjet machining," *Composites Part A: Applied Science and Manufacturing,* vol. 39, pp. 923-929, 2008.
[30] D. Shanmugam, *et al.*, "Minimisation of kerf tapers in abrasive waterjet machining of alumina ceramics using a compensation technique," *International Journal of Machine Tools and Manufacture,* vol. 48, pp. 1527-1534, 2008.
[31] M. A. Azmir and A. K. Ahsan, "A study of abrasive water jet machining process on glass/epoxy composite laminate," *Journal of Materials Processing Technology,* vol. 209, pp. 6168-6173, 2009.
[32] S. Paul, *et al.*, "Abrasive water jet machining of glass fibre metal laminates," *Proceedings of the Institution of Mechanical Engineers, Part B: Journal of Engineering Manufacture,* vol. 216, pp. 1459-1469, 2002.
[33] A. Schoppa, *et al.*, "Influence of the cutting process on the magnetic properties of non-oriented electrical steels," *Journal of magnetism and magnetic materials,* vol. 215, pp. 100-102, 2000.
[34] A. Schoppa, *et al.*, "Influence of the manufacturing process on the magnetic properties of non-oriented electrical steels," *Journal of magnetism and magnetic materials,* vol. 215, pp. 74-78, 2000.
[35] A. Moses, *et al.*, "Aspects of the cut-edge effect stress on the power loss and flux density distribution in electrical steel sheets," *Journal of magnetism and magnetic materials,* vol. 215, pp. 690-692, 2000.
[36] F. Ossart, *et al.*, "Effect of punching on electrical steels: Experimental and numerical coupled analysis," *Magnetics, IEEE Transactions on,* vol. 36, pp. 3137-3140, 2000.
[37] E. Hug, *et al.*, "Effect of internal stresses on the magnetic properties of non-oriented Fe–3wt.% Si and (Fe,Co)–2wt.% V alloys," *Materials Science and Engineering: A,* vol. 332, pp. 193-202, 2002.
[38] O. Hubert and E. Hug, "Influence of plastic strain on magnetic behaviour of non-oriented Fe&# 8211; 3Si and application to manufacturing test by punching," *Materials science and technology,* vol. 11, pp. 482-487, 1995.
[39] M. Emura, *et al.*, "The influence of cutting technique on the magnetic properties of electrical steels," *Journal of magnetism and magnetic materials,* vol. 254–255, pp. 358-360, 2003.
[40] Y. Kurosaki, *et al.*, "Importance of punching and workability in non-oriented electrical steel sheets," *Journal of magnetism and magnetic materials,* vol. 320, pp. 2474-2480, 2008.

[41] S. Murthy, *et al.*, "Minimization of torque pulsations in a trapezoidal back-EMF permanent magnet brushless DC motor," 1999, pp. 1237-1242 vol. 2.
[42] G. Loisos and A. J. Moses, "Effect of mechanical and Nd:YAG laser cutting on magnetic flux distribution near the cut edge of non-oriented steels," *Journal of Materials Processing Technology,* vol. 161, pp. 151-155, 2005.
[43] M. Malekian, *et al.*, "Modeling of dynamic micro-milling cutting forces," *International Journal of Machine Tools and Manufacture,* vol. 49, pp. 586-598, 2009.
[44] P. Basuray, *et al.*, "Transition from ploughing to cutting during machining with blunt tools," *Wear,* vol. 43, pp. 341-349, 1977.
[45] C. J. Kim, J. R. Mayor, and J. Ni "A static model of chip formation in microscale milling," *Journal of manufacturing science and engineering,* vol. 126, p. 710, 2004.
[46] M. P. Vogler, *et al.*, "Microstructure-level force prediction model for micro-milling of multi-phase materials," *Journal of manufacturing science and engineering,* vol. 125, pp. 202-209, 2003.
[47] C. J. Kim, *et al.*, "Experimental analysis of chip formation in micro-milling," *TECHNICAL PAPERS-SOCIETY OF MANUFACTURING ENGINEERS-ALL SERIES-,* 2002.
[48] S. S. Joshi and S. N. Melkote, "An explanation for the size-effect in machining using strain gradient plasticity," *Journal of manufacturing science and engineering,* vol. 126, p. 679, 2004.
[49] D. Dornfeld, *et al.*, "Recent Advances in Mechanical Micromachining," *CIRP Annals - Manufacturing Technology,* vol. 55, pp. 745-768, 2006.
[50] X. Liu, *et al.*, "The mechanics of machining at the microscale: assessment of the current state of the science," *Journal of manufacturing science and engineering,* vol. 126, p. 666, 2004.
[51] M. Zaman, *et al.*, "A three-dimensional analytical cutting force model for micro end milling operation," *International Journal of Machine Tools and Manufacture,* vol. 46, pp. 353-366, 2006.
[52] W. Bao and I. Tansel, "Modeling micro-end-milling operations. Part I: analytical cutting force model," *International Journal of Machine Tools and Manufacture,* vol. 40, pp. 2155-2173, 2000.
[53] C. Li, *et al.*, "Modeling of three-dimensional cutting forces in micro-end-milling," *Journal of Micromechanics and Microengineering,* vol. 17, p. 671, 2007.

[54] J. Tlusty and P. MacNeil, "Dynamics of cutting forces in end milling," *Annals of the CIRP,* vol. 24, pp. 21-25, 1975.
[55] J. Park*, et al.*, "Evaluation of machinability in the micro end milling of printed circuit boards," *Proceedings of the Institution of Mechanical Engineers, Part B: Journal of Engineering Manufacture,* vol. 223, pp. 1465-1474, 2009.
[56] J. P. Davim and P. Reis, "Damage and dimensional precision on milling carbon fiber-reinforced plastics using design experiments," *Journal of Materials Processing Technology,* vol. 160, pp. 160-167, 2005.
[57] I. El-Sonbaty*, et al.*, "Factors affecting the machinability of GFR/epoxy composites," *Composite structures,* vol. 63, pp. 329-338, 2004.
[58] J. P. Davim*, et al.*, "A study on milling of glass fiber reinforced plastics manufactured by hand-lay up using statistical analysis (ANOVA)," *Composite structures,* vol. 64, pp. 493-500, 2004.
[59] R. Teti, "Machining of composite materials," *CIRP Annals-Manufacturing Technology,* vol. 51, pp. 611-634, 2002.
[60] A. Boehm and I. Hahn, "A new approach in the production of electrical motors using only machining processes," in *1st International Electric Drives Production Conference, EDPC-2011, September 27, 2011 - September 30, 2011*, Nuremberg, Germany, 2011, pp. 78-83.
[61] J. Tlusty, *Manufacturing Processes and Equipment*: Prentice Hall Upper Saddle River, 2000.
[62] J. M. Amiss*, et al.*, *Machinery's handbook guide 27*: Industrial Press Inc., 2004.
[63] S. Kalpakjian and S. R. Schmid, *Manufacturing Engineering and Technology Machining* vol. 45h: Prentice Hall, Pearson Education, Inc. , 2003.
[64] E. Armarego and N. Deshpande, "Computerized predictive cutting models for forces in end-milling including eccentricity effects," *CIRP Annals-Manufacturing Technology,* vol. 38, pp. 45-49, 1989.
[65] E. Armarego and N. Deshpande, "Computerized end-milling force predictions with cutting models allowing for eccentricity and cutter deflections," *CIRP Annals-Manufacturing Technology,* vol. 40, pp. 25-29, 1991.
[66] F. Gu*, et al.*, "An approach to on-line cutter runout estimation in face milling," *Transactions of NAMRI/SME,* vol. 19, pp. 240-247, 1991.

[67] W. A. Kline and R. DeVor, "The effect of runout on cutting geometry and forces in end milling," *International Journal of Machine Tool Design and Research,* vol. 23, pp. 123-140, 1983.
[68] W. Y. Bao and I. N. Tansel, "Modeling micro-end-milling operations. Part II: tool run-out," *International Journal of Machine Tools and Manufacture,* vol. 40, pp. 2175-2192, 2000.
[69] S. Y. Liang and J. J. J. Wang, "Milling force convolution modeling for identification of cutter axis offset," *International Journal of Machine Tools and Manufacture,* vol. 34, pp. 1177-1190, 1994.
[70] J. R. Mayor and A. A. Sodemann, "Curvature-based tool-path segmentation for feedrate optimization in micromilling," in *Transactions of the North American Manufacturing Research Institution of SME, May 20, 2008 - May 23, 2008*, Monterrey, Mexico, 2008, pp. 285-292.
[71] M. Arif*, et al.*, "Analytical model to determine the critical feed per edge for ductile–brittle transition in milling process of brittle materials," *International Journal of Machine Tools and Manufacture,* vol. 51, pp. 170-181, 2011.
[72] A. S. Corporation, "Selection of Electrical Steels for Magnetic Cores," in *Product dat bulletin*, A. S. Corporation, Ed., ed. Middletown,OH: AK Steel Corporation, 2003.
[73] P. C. Tseng and I. C. Chiou, "The burrs formation prediction and minimization based on the optimal cutting parameters design method," *JSME International Journal Series C,* vol. 46, pp. 779-787, 2003.
[74] N. E. Dowling, *Mechanical behavior of materials: engineering methods for deformation, fracture and fatigue*, 2nd Edition ed.: Prentice Hall, 1999.
[75] K. Nakayama and M. Arai, "Burr formation in metal cutting," *CIRP Annals-Manufacturing Technology,* vol. 36, pp. 33-36, 1987.
[76] L. K. Gillespie and P. Blotter, "Formation and properties of machining burrs," *J. Eng. Ind.(Trans. ASME, B),* vol. 98, pp. 66-74, 1976.
[77] C. C. Tsao and H. Hocheng, "Effects of exit back-up on delamination in drilling composite materials using a saw drill and a core drill," *International Journal of Machine Tools and Manufacture,* vol. 45, pp. 1261-1270, 2005.
[78] B. Denkena*, et al.*, "Helical milling of CFRP-titanium layer compounds," *CIRP Journal of Manufacturing Science and Technology,* vol. 1, pp. 64-69, 2008.

[79] A. S. Corporation, "Non-Oriented Electrical Steels," in *Product dat bulletin*, A. S. Corporation, Ed., ed. Middletown,OH: AK Steel Corporation, 2003.

[80] ASTM, "ASTM A804/A804M-04," in *Standard Test Methods for Alternating-Current Magnetic Properties of Materials at Power Frequencies Using Sheet-Type Test Specimens*, ed. 100 Barr Harbor Drive, P.O. Box C700, West Conshohocken, PA 19428, USA: ASTM International, 2009.

[81] M. De Wulf*, et al.*, "Design and calibration aspects of small size single sheet testers," *Journal of magnetism and magnetic materials,* vol. 254, pp. 70-72, 2003.